The Dissertation Committee for Hyoungdo Nam certifies that this is the approved version of the following dissertation:

Scanning Tunneling Microscope Studies of 2D Superconductor and 3D Intrinsic Topological Insulator

Committee:

Chih-Kang Shih, Supervisor

Alex de Lozanne

John T. Markert

Gregory A Fiete

Li Shi

Scanning Tunneling Microscope studies of 2D Superconductor and 3D Intrinsic Topological Insulator

by

Hyoungdo Nam, B.S.; M.S.

Dissertation

Presented to the Faculty of the Graduate School of

The University of Texas at Austin

in Partial Fulfillment

of the Requirements

for the Degree of

Doctor of Philosophy

The University of Texas at Austin

May 2015

To my family

Acknowledgements

First of all, I would like to express my appreciation to all of my committee members, Dr. de Lozanne, Dr. Markert, Dr. Fiete, Dr. Shi, and Dr. Shih for their valuable time spent evaluating my dissertation; I would especially like to thank my supervisor Dr. Shih for giving me a lot of opportunities and thoughtful comments during my doctoral courses. During that period, I had many valuable experiences building systems, such as STM, MBE, *in-situ* double-coil mutual inductance set-up, UHV-LT sample transfer vessel, Knudsen-cells, e-beam evaporators , etc., as well as carrying out valuable experiments using them. I would also like to express my gratitude to my former research advisors that supervised me during my master degree: Dr. Haesuk Yang, Dr. Jung Il Lee, Dr. Won Jun Choi, and Dr. Jin Dong Song.

In Dr. Shih's lab, I would like to say thanks to all my former and current lab mates for all their help: Dr. Jungdae Kim, Dr. Jisun Kim, Dr. Ho-Ki Lyeo, Dr. Daejin Eom, Dr. Charlotte Sanders, Dr. Chris Mann, Dr. Sen Yang, Dr. Sebastien Founta, Dr. Chendong Zhang, Dr. Miri Choi, Dr. Huan Li, John Roberson, Amber Jonson, Yuxuan Chen, Ping-Hsiang Su. I am especially grateful to Dr. Jungdae Kim's help learning about LT-STM. In addition, I would like to acknowledge my debt to all the members in machine shop, cryogenic shop, and electronic shop for their willingness to give me a hand with my projects.

From my seven years of living in Austin, I will treasure the memories I have of my time spent with PAMA softball team at Intramural Fields. I am especially thankful to Dr. Yongsup Ihn who helped me properly settle in immediately upon my arrival in Austin and to Dr. Jusang Yang who gave me lots of help at every step of the way. I will never forget

our “Third Floor Coffee Break” after lunch. Daniel Cho, I am grateful to you for editing my dissertation.

Moreover, I am thankful to all of my collaborators: Dr. Jie Yong, and Dr. Thomas R Lemberger at Ohio State University, Philip A Kratz, Dr. John R Kirtley, and Kathryn A Moler at Stanford University, Tijiang Liu and Dr. Philip Adams at Louisiana State University, Dr. Yong P Chen at Purdue University.

Last but not least, I would like to acknowledge my great debt to my family, especially my elder sister, Jinchool Nam. Thanks for your support for the longtime doctoral degree.

I dedicate my dissertation to my family.

Hyoungdo Nam

The University of Texas at Austin

May 2015

Scanning Tunneling Microscope Studies of 2D Superconductor and 3D Intrinsic Topological Insulator

Hyoungdo Nam, Ph.D.

The University of Texas at Austin, 2015

Supervisor: Chih-Kang Shih

Electrons show unusual and interesting behaviors both in low dimensions and on material surfaces, distinct from what they display in bulk materials. These intriguing properties have been studied in order to understand their origins. One area where this can be seen is in the case of superconductivity, where superconducting phase fluctuation in a thin superconductor is supposed to substantially suppress the superconductivity of the material as the film thickness decreases. To test this, we prepared epitaxially grown and globally flat lead (Pb) films; here, the thinnest film was 1.4 nm thick. Four different length scale measurements, ranging from the nm to the mm scale, gave consistent superconducting transition temperatures. Our results proved that the film of 1.4 nm still has strong superconducting phase stiffness; namely, the superfluid phase is rigid even in 1.4 nm thin superconductor film. Moreover, the parallel critical magnetic field is remarkably strong so that superconductivity is still observed in Zeeman fields, exceeding the Pauli limit.

In addition, the surface of 3D topological insulator has a novel quantum state induced by strong spin-orbit interaction. A number of material studies were conducted to find a surface dominated conduction topological insulator that has a large energy gap and a single Dirac cone. Moreover, it is necessary for the material to be stable against aging

unlike most 3D topological insulators, such as Bi_2Se_3. Here, Bi_2Te_2Se and $BiSbTeSe_2$ were studied in terms of their structures, electronic properties, and aging effects on them. Scanning tunneling microscopy analysis attested that Bi_2Te_2Se is an order alloy, which has a slight randomness of 15 %, whereas $BiSbTeSe_2$ is a random alloy. Scanning tunneling spectroscopy on $BiSbTeSe_2$ confirmed that the Dirac point tends to stay around the Fermi level under the strong band structure change, induced by random structure. The most surprising observation was that $BiSbTeSe_2$ showed remarkable stability despite the rich composition of selenium (Se). Even after aging for seven days, the Fermi level and the Dirac point remained at almost the same level in bulk band gap. Both observations are very important for applications to utilize the exotic topological surface state.

Table of Contents

List of Tables

List of Figures

Chapter 1: Background to Scanning Tunneling Microscope

The scanning tunneling microscope (STM) was invented early in the 1980s by G. Binning and H. Rohrer at IBM Zurich, who earned the Nobel Prize "for their design of the scanning tunneling microscope" in Physics in 1986. They reported STM development with the first demonstration of three dimensional real-space imaging of the famous silicon (Si) (111) – 7 × 7 reconstruction surface on an atomic scale in autumn 1982 [1-2]. Figure 1.1 (a) and (b) are photographs of the first STM and the Si(111) – 7 × 7 surface image created by using the STM, respectively. Indeed, the STM mapped every corner hole and twelve adatoms in 7 × 7 unit cell, which is interpreted as dimer-adatom-stacking-fault (DAS) model of Si(111) – 7 × 7 [3].

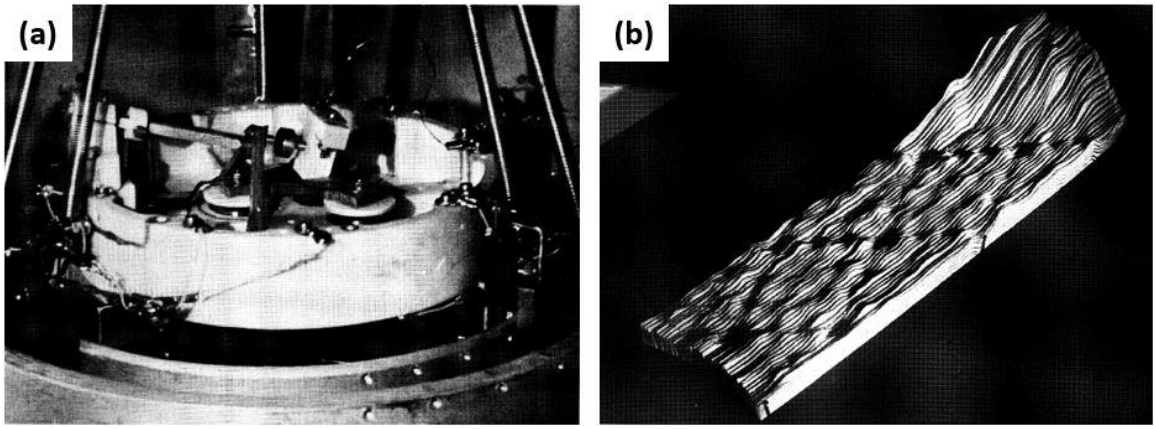

Figure 1.1: (a) Photograph of the first STM (adopted from ref. [1]). (b) The topographic image of Si(111) - 7 × 7 reconstruction surface taken by the STM (adopted from ref. [1]).

Since then, many people are now taking advantage of STM as one of the major tools for studying diverse materials in various fields, such as surface science, superconductivity, and magnetism; in addition, it can be used to manipulate individual

atoms to investigate the fundamental properties of atoms and molecules or to create an artificial structure [4, 5].

1.1 Crucial components of STM set up

All the crucial elements of the first STM are still adopted to current STM designs, although specific components have been improved to maximize STM performance. The important elements of an STM includes the tip, piezo scanner, coarse drive, vibration isolation, and electronics (Figure 1.2). First of all, an atomically sharp and conductive tip is needed to achieve atomic scale lateral resolution. Also, the piezo scanner, using the piezo electric effect, allows fine tip movement of ten pico-meters or less.

The working principle of a STM is based on the tunneling current through the vacuum gap of 3 - 7 Å between the tip and a sample surface. Coarse drive enables the tip to safely approach the sample surface as close as the vacuum gap of around 5 Å; here, the displacement of coarse drive per one step should be shorter than the full range of the z-piezo drive in order to avoid the collision between the tip and the sample. After locating the tip in the tunneling range, the coarse drive must rigidly hold the piezo drive at that location while a tip scans sample surface.

As mentioned above, STM operation requires tunneling current which are typically 10 pA - 10 nA. To measure such a low level current, a scanning controller is equipped with a preamplifier of 10^9 V/A gain. In addition, the controller, assisted by a computer, handles tip-movement in the xy-plane and z-feedback loop in terms of tunneling current, as well as data acquisition.

Lastly, the STM works on a few angstrom tip-to-sample distance and its desired vertical resolution is in the order of pico-meter. Since the typical level of floor vibration of

0.1 - 1 μm is too strong to allow for this resolution, the STM must be equipped with an effective vibration isolation system to significantly reduce noise from that environment.

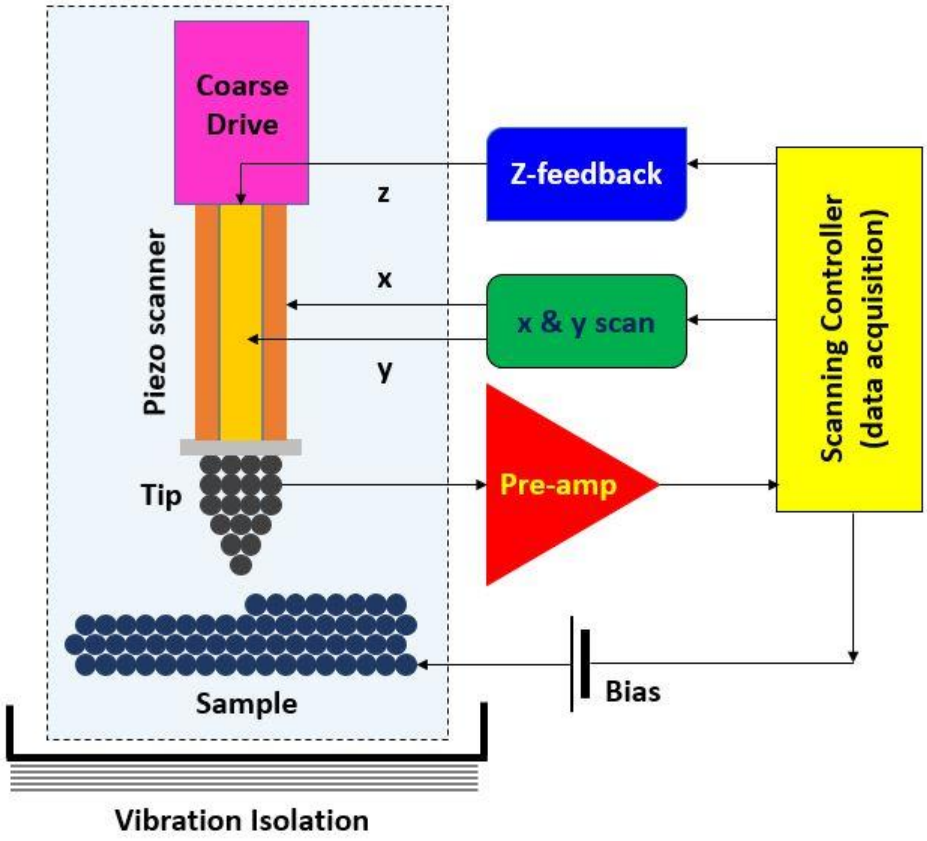

Figure 1.2: Schematic diagram of the scanning tunneling microscope.

1.2 Tunneling current

Before the creation of the STM, tunneling spectroscopy was demonstrated by I. Giaever in 1960 [6]. Using electron tunneling via metal-insulator-metal planar junction, his measurement had directly shown the superconducting energy gap, the critical evidence

for Bardeen-Cooper-Schrieffer (BCS) superconductivity theory [7]. The tunneling phenomenon in STM is a salient operation principle needed to understand scanning tunneling spectroscopy as well.

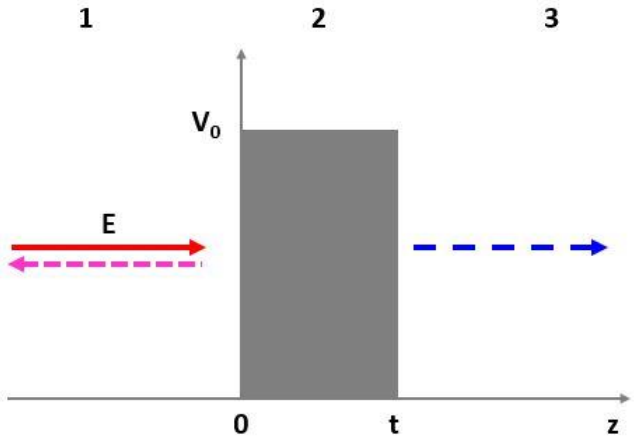

Figure 1.3: Electron tunneling of $E = \hbar^2 k^2 / 2m$ through one dimensional square potential barrier of V_0 in height and t in width. Electron incidents from left side.

1.2.1 Electron tunneling through a square potential barrier

When one considers an electron of energy (E) and mass (m) in a simple case of a one dimensional square potential barrier, like Figure 1.3, the Schrödinger equation,

$$-\frac{\hbar^2}{2m}\frac{d^2}{dz^2}\Psi_i(z) + U(z)\Psi_i(z) = E\Psi_i(z) \qquad (1.1)$$

gives the wave functions of the electron at each region, i = 1, 2, 3. Then, the continuity of the wave functions and their first derivatives, $d\Psi_i/dz$ at the potential boundaries of both z = *0* and $z = t$ leads to tunneling current density,

$$J_t = -\frac{i\hbar}{2m}\left[\Psi_3^*(z)\frac{d\Psi_3(z)}{dz} - \frac{d\Psi_3^*(z)}{dz}\Psi_3(z)\right]$$

$$= \frac{\hbar k}{m} T. \tag{1.2}$$

Here, the exact form of the transmission coefficient, T is

$$T(E) = \frac{1}{1 + \frac{(k^2 + \varkappa^2)^2}{4k^2\varkappa^2} sinh^2(\varkappa t)} \tag{1.3}$$

with a wave vector of $k = \sqrt{2mE/\hbar^2}$ and a decay constant of $\varkappa = \sqrt{2m(V_0 - E)/\hbar^2}$.

Practically, in the case of a strongly attenuating barrier, $\varkappa t \gg 1$,

$$T(E) \approx \frac{16k^2\varkappa^2}{(k^2 + \varkappa^2)^2} \mathrm{e}^{-2\varkappa t}. \tag{1.4}$$

Here, the transmission coefficient is dominantly governed by $\mathrm{e}^{-2\varkappa t}$. The decay constant is $\varkappa = 0.51\sqrt{V_0 - E}$ (Å^{-1}). Applying the typical value of a metal's work function, ~ 4 eV to $V_0 - E$, the decay constant is $\varkappa \approx 1\ \text{Å}^{-1}$. This corresponds to the change of transmission coefficient as much as $e^{-2} \approx 7.4$ times per 1 Å change in barrier width.

1.2.2 Tunneling current for metal-vacuum-metal tunneling junction

In the case of STMs, previous V_0 - E is approximately replaced by a work function ϕ for the small bias voltage. The tunneling current should be proportional to the number of states at E as well as tunneling coefficient. The sample states in the energy span between $E_F - eV$ and E_F are mainly responsible for tunneling current. Since the local density of states (LDOS) can be defined as

$$\rho_{sample}(E) \equiv \frac{1}{\epsilon} \sum_{E_n = E - \epsilon}^{E} |\Psi_n|^2, \tag{1.5}$$

tunneling current becomes

$$I \propto \sum_{E_n = E_F - eV}^{E_F} |\Psi_n|^2 \, T(E_n)$$
$$\approx V \rho_{sample}(E_F) e^{-1.02\sqrt{\phi} t}. \tag{1.6}$$

As mentioned in the previous section, 1 Å change along the z-direction can give rise to an abrupt jump of the tunneling current by one order of magnitude. Equation (1.6) shows how sensitive the tunneling current is with respect to the variation of distance between electrodes. Moreover, it shows that the tunneling current includes the information of Fermi level LDOS of a sample with a bias voltage.

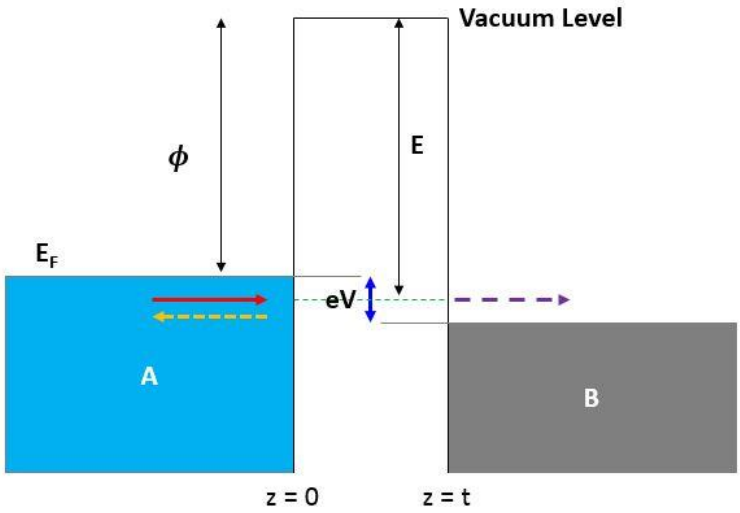

Figure 1.4: Simplified metal-vacuum-metal tunneling junction.

1.2.3 Time-dependent perturbation approach

Time-dependent perturbation approach, also known as the Bardeen approach, was developed by J. Bardeen in 1960 to interpret metal-insulator-metal tunneling junction [8]. Unlike the previous method of solving the Schrodinger equation for a potential system, Bardeen set a separation surface at a location z_0 in the middle of potential barrier to divide the full system to two independent subsystems, described by the wavefunctions of ψ and

χ. Using time-dependent perturbation theory, the tunneling matrix element *M*, describing the transferring amplitude from one electrode ψ to another χ, is given by

$$M_{\psi\to\chi} = \frac{\hbar}{2m}\int_{z_0}\left(\chi^*\frac{\partial\psi}{\partial z} - \frac{\partial\chi}{\partial z}\psi^*\right)dS. \tag{1.7}$$

From Fermi's golden rule [9], the electron transferring rate from ψ to χ is

$$\gamma = \frac{2\pi}{\hbar}\left|M_{\psi\to\chi}\right|^2\delta(E_\psi - E_\chi), \tag{1.8}$$

where δ is the delta function to restrict electron tunneling to an elastic process. For the same reason used in the previous section, the sum of all of the contributions of the relevant states gives the total tunneling current. At a finite temperature, the tunneling current is

$$I = \frac{4\pi e}{\hbar}\int_{-\infty}^{\infty}[f(E_F - eV + \epsilon) - f(E_F + \epsilon)] \times \rho_\psi(E_F - eV + \epsilon)\rho_\chi(E_F + \epsilon)\left|M_{\psi\to\chi}\right|^2 \mathrm{d}\epsilon, \tag{1.9}$$

where $f(E) = 1/\{1 + \exp[(E - E_F)/k_BT]\}$ is the Fermi distribution function, $\rho_i(E)$ is LDOS.

At sufficiently low temperatures, Fermi distribution function can be considered as a step function; subsequently, equation (1.9) becomes simplified as

$$I = \frac{4\pi e}{\hbar}\int_0^{eV}\rho_\psi(E_F - eV + \epsilon)\rho_\chi(E_F + \epsilon)\left|M_{\psi\to\chi}\right|^2 \mathrm{d}\epsilon. \tag{1.10}$$

With the assumption that the energy is independent of $\left|M_{\psi\to\chi}\right|^2$around the Fermi level where we are considering, $\left|M_{\psi\to\chi}\right|^2$ can move outside of integral [8]. Now, tunneling current is just proportional to the convolution of LDOSs of both electrodes. It implies that the electronic structures of both of the electrodes equally contribute to tunneling current. If, in the STM application, one uses an almost constant DOS tip, the tunneling current only reflects pure information of the sample's electronic structure. Allowing the first derivative of tunneling current with respect to bias voltage to be

$$\frac{dI}{dV} \propto \rho_{sample}(E_F - eV). \tag{1.11}$$

Thus, scanning tunneling spectroscopy can prove the spatial variation of LDOS of a sample with an ideal tip.

1.2.4 Inelastic electron tunneling

In addition to the elastic tunneling current, inelastic processes enable another possible channel for electron to transfer from one electrode to another [Figure 1.5 (a)]. Here, excitations in the electrodes assist the inelastic process in electron tunneling; such as with phonons in solids and the vibrational modes for molecules. Since those excitations have a characteristic energy of $\hbar\omega$, they are not activated until electron kinetic energy reach the characteristic energy. When electron kinetic energy of eV exceeds $\hbar\omega$, inelastic tunneling current starts contributing to total current like what is shown in the upper panel of Figure 1.5 (b). Then the contribution of inelastic process to total tunneling current appears in the *I-V*, *dI/dV*, and d^2I/dV^2 spectra [Figure 1.5 (b)]. The inelastic feature in the *I-V* and *dI/dV* spectra is usually very weak and it is easy to smear out inelastic feature due to broadening effects. The broadening happens due to the natural distribution of excitation modes, thermal broadening of the order of k_BT, and broadening due to the experimental measurement technique. In contrast, inelastic feature of the d^2I/dV^2 spectra can appear as a peak at each characteristic energy. Indeed, the second derivative is really helpful for the study of possible excitations in a sample at a finite temperature.

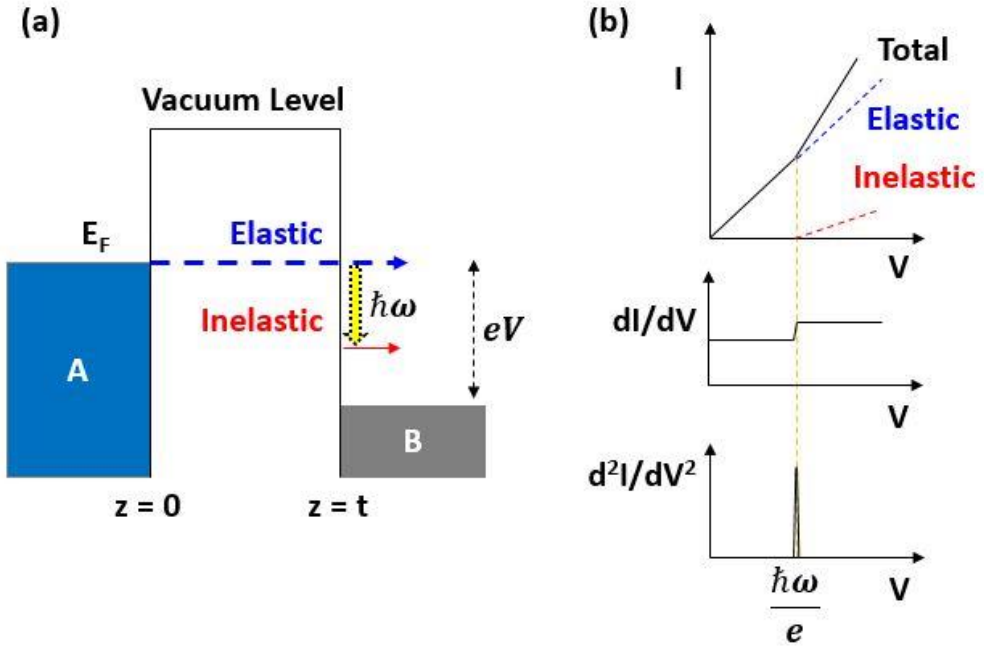

Figure 1.5: (a) Schematics of the inelastic tunneling process in contrast to elastic tunneling process. (b) Simplified appearance of inelastic process in tunneling spectra.

1.3 STM operation modes

1.3.1 Two different topographic mapping modes

Constant current mode (CCM) is the most common STM operation mode. In CCM, z-feedback loop keeps the tunneling current of a set-point by adjusting tip-to-sample distance, while a tip scans on the xy-plane above sample surface. At the same time, a computer recodes not only (x, y) coordinate information but also the variation of tip height *z*. In CCM, the scanning speed is limited by the response time of feedback loop although the tip can scan a sample surface faster than feedback loop.

A fast imaging can be achieved in variable current mode, so called constant height mode (CHM). In this mode, feedback loop is turned off during scanning xy-plane, which

means that the tip moves without change the tip height. But STM can still sense local variations of tip-to-sample distance, which is available from the sample surface profile itself, and can recode $I(x, y)$, instead of $z(x, y)$. The STM can map the sample surface at real time video rate; therefore, it is feasible to observe the dynamic processes of atoms on a sample surface, such as surface diffusion in real time.

1.3.2 Tunneling spectroscopy (TS)

STM is able to do electronic spectroscopy at a certain location of atomic scale accuracy in addition to its scanning ability. As shown before, tunneling spectroscopy (TS) can show LDOS information of a sample as a function of the energy by taking an *I-V* measurement at a constant tip-sample spacing.

Moreover, STM can change the tip-sample spacing under control in contrast to the earlier tunneling study using a planar metal-insulator-metal junction [6]. From the exponential dependence of the tunneling current as a function of tip-sample spacing, $I \propto e^{-1.02\sqrt{\phi}z}$, the sample's work function ϕ can be obtained by an *I-z* measurement.

$$\phi = \left(-\frac{1}{1.02} \frac{d\ln(I)}{dz} \right)^2 \tag{1.12}$$

In fact, the first STM test was showing the exponential relationship between *I* and *z*. Inventors had succeeded in observing this feature by using their STM, tungsten tip, and a platinum sample on the night of March 16th, 1981 [10].

1.3.3 Scanning tunneling spectroscopy (STS) at constant current

From the concept of equation (1.11), the first derivative of tunneling current in terms of applied bias, dI/dV, reflects LDOS at a certain energy level. The observed energy

level can be tuned by an applied bias voltage. Using a lock-in technique, one can apply a DC-bias that is modulated with a high frequency, small AC-voltage to a sample, and then take the in-phase component from tunneling current, proportional to dI/dV to measure the LDOS at a specific energy level. Therefore, scanning tunneling spectroscopy (STS) at constant current means spatial variation of LDOS on a sample surface. In practice, one has to keep in mind that dI/dV depends on not only LDOS but also the spatial dependence of the transmission coefficient.

1.3.4 Current imaging tunneling spectroscopy (CITS)

Current imaging tunneling spectroscopy (CITS) is a combined mode of CCM and TS. During CITS, a tip moves from one pix cell to another while feedback loop holds the system at a constant current of set point. The feedback loop is then cut off and then STM immediately takes a tunneling spectrum at that location. After the tunneling spectrum for the area is taken, the feedback loop is turned on once again and the tip is moved to a new location. This pattern is repeated until the desired sample area is scanned. Therefore, CITS allows us to study the spatial variation of LDOS at an atomic scale. Figure 1.6 shows an example of CITS, which was carried out for the study of the superconductivity proximity effect in a superconductor-normal metal- superconductor junction. Figure 1.6 (a) is the topographic image acquired during CITS. Figure 1.6 (b) is the zero bias conductance extracted from the tunneling spectra of CITS, which reflects the local superconductivity variation. Line spectra of Figure 1.6 (c) and (d) from CITS also exhibit superconductive transition along the white solid and dash lines, respectively.

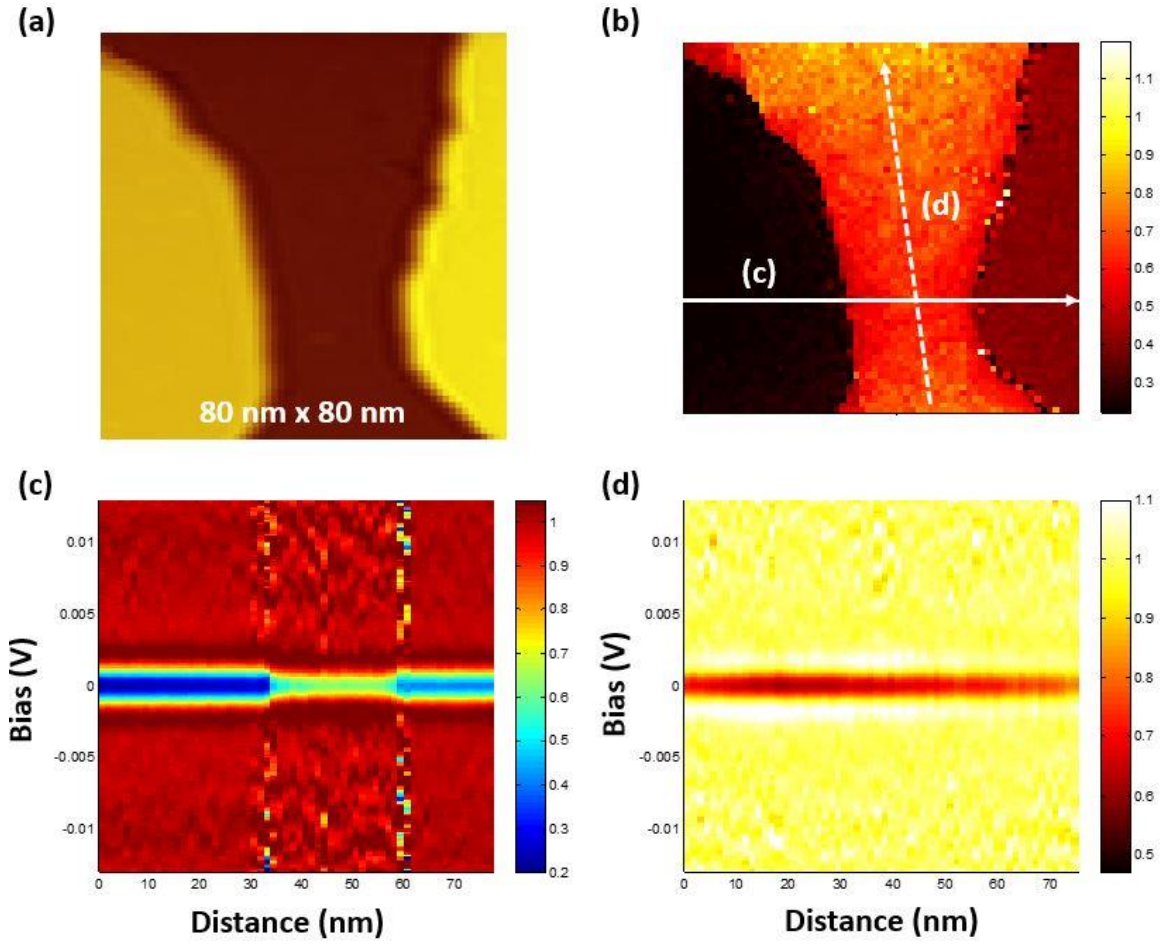

Figure 1.6: (a) CITS topographic image of 80 nm × 80 nm area, showing a superconductor-normal metal-superconductor system (b) Zero bias conductance from CITS, which clearly exhibits the proximity effect of the neighbor superconductors on the normal metal. (c) and (d) are line spectra along the white solid and dash lines in (b), respectively. They show the distance dependence of proximity effect of the superconductor.

Chapter 2: High spatial/energy resolution ultrahigh-vacuum low-temperature STM

STM is one of the major experimental instruments used in material science. Many intriguing scientific observations are achieved in low temperature environment. In order to explore materials in a low temperature regime, our laboratory has also dedicated decades of work in to building up STMs that can work at low temperate (LT) under ultrahigh vacuum (UHV), with *in-situ* growth capability. In this chapter, we shall look over our UHV-LT STM, briefly, and then see how to improve the performance of our original STM in both energy resolution and sample preparation capability.

2.1 UHV-LT STM

2.1.1 Pan-type piezoelectric step motor

The Pan-type STM is named after S. H. Pan who developed the piezoelectric step motor design [11-13]. We also adopted Dr. Pan's design and integrated it into our home-built UHV-LT STM, built by our former graduate students [14, 15]. In our case, the piezoelectric step motor consists of six piezo actuators, a sapphire prism center shaft, and a Macor-ceramic frame. The piezo actuators are attached on the inner wall of Macor-ceramic frame and hold the center shaft by utilizing the friction force between the piezo stacks and the center shaft surface. It makes one step by following this process: Frist, the one of the piezo actuators slide toward one direction individually and successively while the remaining five actuators hold the center shaft in place. When all actuators finish their sliding, they then restore their shear motions all at the same time, moving the center shaft with them and completing the one step displacement in the piezo shear sliding direction.

This Pan-type piezoelectric step motor is used as a reliable positioner to approach our tip to sample's surface in the operation rage of z-scanner.

Figure 2.1 shows one of Pan-type STM head in Dr. Shih's laboratory, which I made, that works in STM mode. Recently, I have changed its usage to UHV double-coil set-up for superconductivity study by measuring superfluid density in macroscopic length scale.

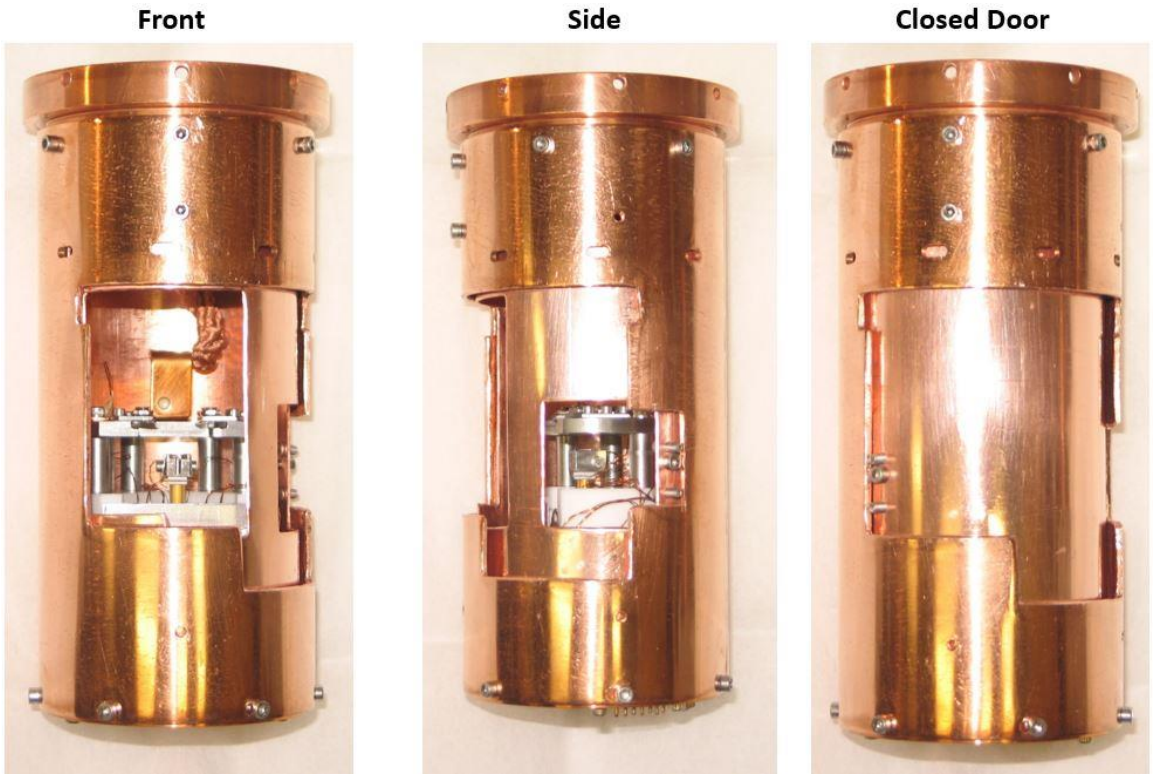

Figure 2.1: Pan-type STM head housed in the most inner cooper radiation shield. The scanning tube is mounted on a sapphire prism.

2.1.2 UHV-LT chamber

Figure 2.2 shows the main vacuum chamber comprising of two parts, the sample/tip preparation section and the LT-STM operation section. In order to achieve UHV of the

order of 10^{-11} torr, two ion pumps and a titanium sublimation pump (TSP) are attached at the bottom of the main chamber. The *in-situ* sample/tip preparation section is equipped with an e-beam tip cleaning stage and a cold finger with sample growth stage and heater at the end of it. Here, the heater is needed to flash a semiconductor substrate by Joule heating. In addition, there are two ports for source material evaporators; currently, they are occupied with a Knudsen-cell for Pb and a home-built thermal evaporator for silver (Ag) and gold (Au). Thus, samples and tips can be prepared under UHV clean environment.

STM is located at the center of the right section of main chamber [Figure 2.2 (a)]. In the middle of the two sections, there is a carousel that is used not only to keep extra samples and tips in UHV, but also to work as an intermediate port between the STM and the sample/tip preparation stage. The maximum capacity of the carousel is four samples and four tips.

Figure 2.2 (b) is the cryostat consisting of LN_2-jacket outside and LHe-bath in the middle. The LHe-bath is hung by a SS tube of 1 inch outer diameter (OD). The bottom of LHe-bath is made of copper to improve thermal conductivity between the STM and the LHe bath. Three layers of copper radiation shields enclose the STM to achieve a temperature that is as close to LHe boiling point of 4.2 K as possible; the outermost shield is connected to LN_2-jacket and the other two are attached to the LHe bath. Finally, the STM can reach 4.3 K as a basic temperature and the basic helium consumption rate is less than 3 ℓ/day. It is worth noting that there is a damping bellows between LN_2-jacket and LHe-bath, which surprisingly reduces transferring vibration noise toward the STM from the outside, especially the noise that is due to LN_2 boiling [14, 15].

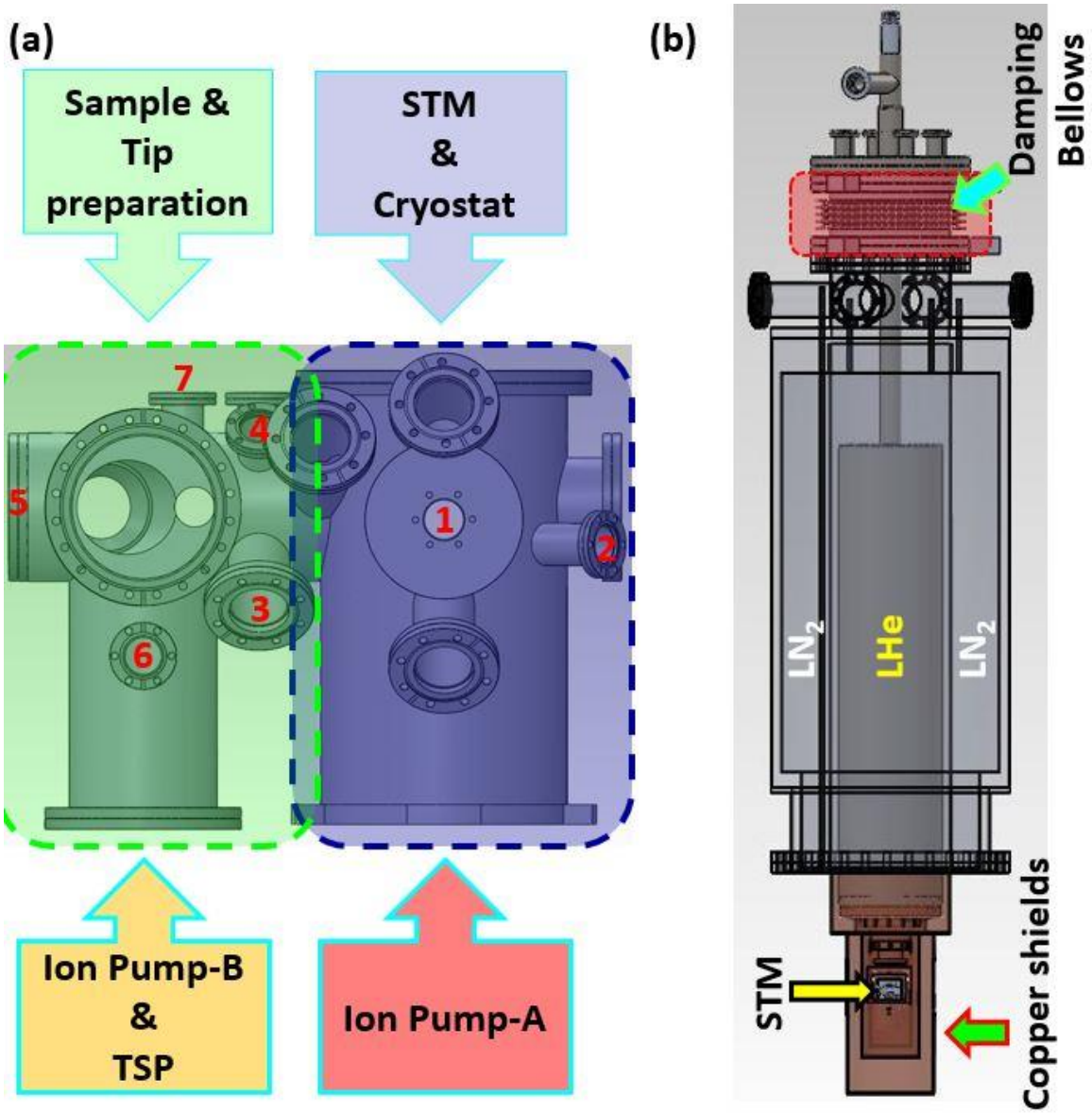

Figure 2.2: (a) STM main chamber consists of two parts, one for sample/tip preparation and the other for LT-STM operation. Two ion pumps are connected to the marked chamber bottom ports. Cryostat with STM (b) is loaded on the top of the right section: #1 port is for wobble stick, #2 for load-lock, #3 for material sources port, #4 for cold finger with a sample growth stage, #5 for 3D motion long travel sample/tip manipulator, #6 for hot-filament ionization gauge, and #7 for e-beam tip cleaning stage. (b) STM is attached to the bottom of cryostat. Three layers of copper radiation shields enclose the STM to achieve the lowest base temperature. In order to reduce transferring vibration noise to STM, there is damping bellows between LN_2-jacket and LHe-bath.

Even after filling the LHe-bath with LN_2 instead of LHe, the STM is still stable so that it can clearly resolve the surface in the atomic scale as seen in Figure 2.3 (a). The fabulous atomic image reveals Pb atoms on the surface of 5 ML Pb film on Si(111) substrate. In Figure 2.3 (b), the line profile along the white dash line shows that the z-resolution is much better than 5 pm even at $T = 77$ K.

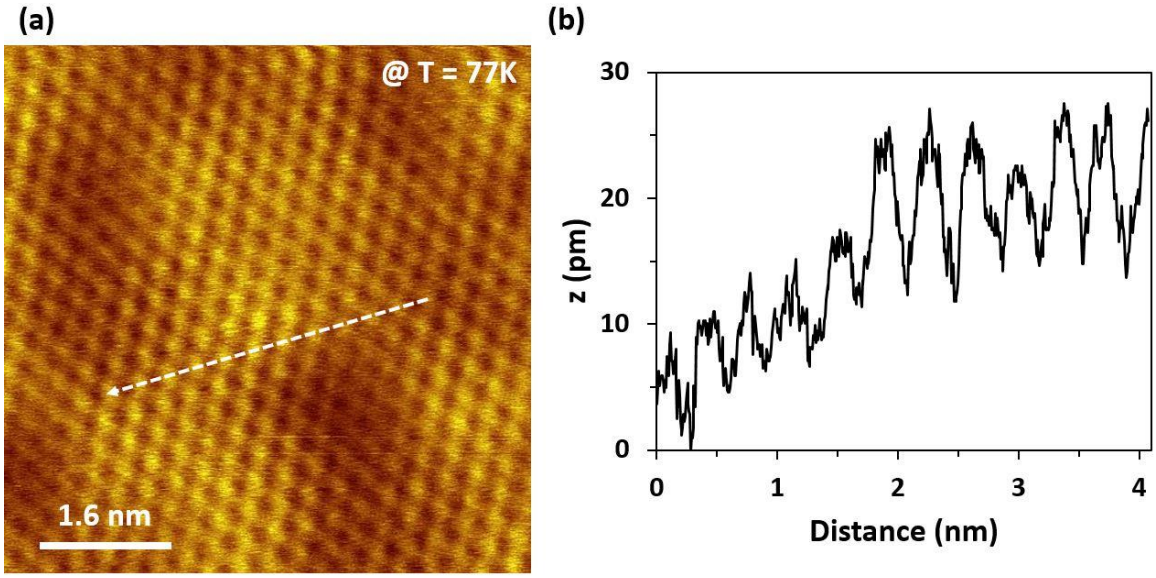

Figure 2.3: (a) An atomic image taken on the surface of 5 ML Pb film on Si(111) substrate at $T = 77$ K. (b) The line prolife along the white dash line reveals that the z-resolution is better than 5 pm.

2.2 Improvement of STM performance

In terms of scanning tunneling spectroscopy, energy resolution is the key factor of STM performance as well as spatial resolution. For example, the superconducting gaps of low dimensional or conventional superconductors are normally in the order of a few meV or less. This means that the desired energy resolution has to be lower than an meV in order

to study low dimensional superconductors. This is especially true for the study of second order features, such as phonon contribution to superconductivity, which requires much lower energy resolution than observation of superconducting gap, for which the energy resolution must be lower than 100 μeV.

To achieve such energy resolution, people have carried out great efforts to enhance STM performance by reducing external noise sources from both mechanical and electrical background noises. Some people built a special room for STM which has a floating floor not in contact with the ground to isolate the room from external vibration noise through the building. Moreover, RF signals in the atmosphere can be absorbed on a number of electrical signal wires required for STM operation due to residual wire capacity, and then the signals are run through the wires. They are specially designed to shield RF signals in atmosphere, which are attributed to one of the strong sources of electrical background noise. Unfortunately, the expense of constructing that kind of room is generally too much to adopt this way of noise reduction.

2.2.1 Radio frequency filtering

Instead of the RF-shielded floating room, there is another way to achieve the same level of STM performance. This alternative method is not only simple but also cheap compared with the previously mentioned method. First of all, RF-filter boxes were made using a series of resin sealed bolt-in filters of 2000 pF, Part No. 1202-005 from Spectrum Control Inc., like Figure 2.4 (a). Each filter is just about $8. As you can see in Figure 2.4 (b), each STM operation cable has its own independent RF-filter. All filter components are enclosed in electromagnetic interference (EMI)/ radio frequency inference (RFI) shielding diecast aluminum box to prevent extra interference after filtering.

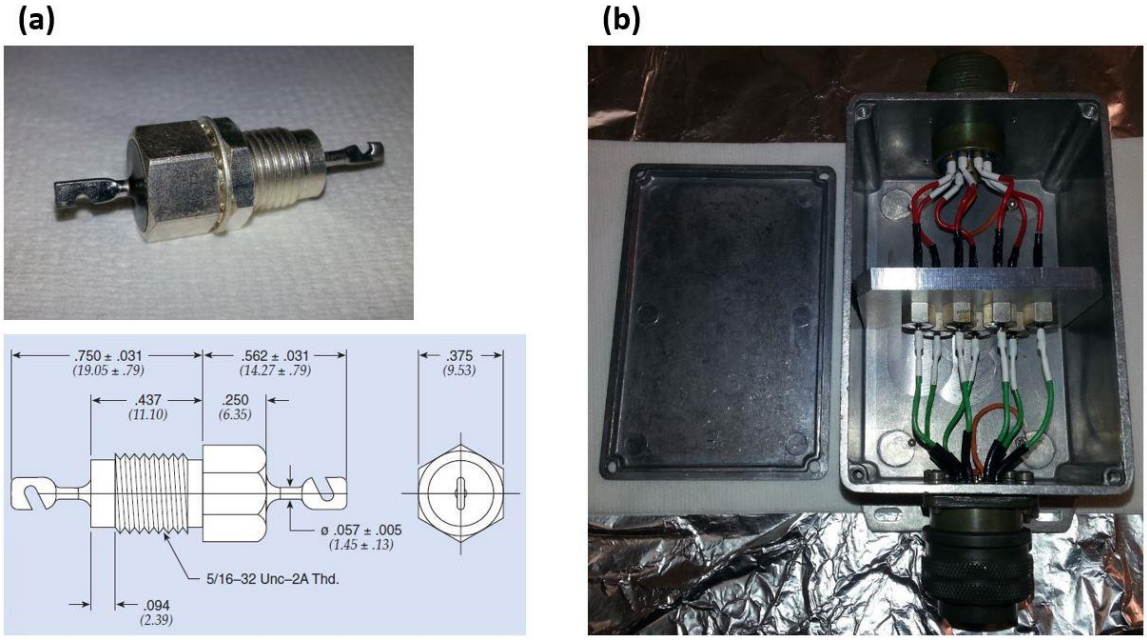

Figure 2.4: (a) RF filter: Part No. 1202-005 from Spectrum Control Inc. The bottom figure shows its dimension in inches (mm) (adopted from ref. [16]) (b) Inside of RF-filter box showing that each signal wire has its own RF-filter and all components are enclosed by EMI/RFI shielding diecast aluminum box.

In fact, we designed two different types of RF filter boxes: indirect filter boxes that were connected to air-side pins of electrical feedthroughs of the STM with an additional bunch of short jump cables and direct filter boxes that were connected by themselves to the air-side pins without jump cables. Note that although the jump cables after RF-filter are less than 30 cm, the jump cables are still able to pick up RF noise of wave lengths on the order of 10 cm or less. Since the improvement of using indirect RF-filter boxes had been shown by J.D. Kim [15], this test have been carried out among only different types of RF-filter boxes. Here, in order to see the pure effect only coming from the four different filter box combinations, seen in Table 2.1, the test had been performed by taking tunneling

spectra at the identical location on 120 ML-Pb/ 20 ML-Ag on Si(111) sample using one W-tip at the same temperature of $T = 4.3$ K.

	Scanner	Walker
I-I	Indirect	Indirect
D-W	Direct	Without
D-I	Direct	Indirect
D-D	Direct	Direct

Table 2.1: Test of four different combinations to connect RF-filter boxes to air-sides of electrical feedthroughs of STM signal wires.

Figure 2.5 (a) shows that tunneling spectra measured with direct RF-filter boxes reveal a deeper zero bias conductance with sharper coherence peaks than an I-I set (black); in addition, D-I (blue) and D-D (red) sets show almost identical spectra. For clarity, I-I and D-D sets have been replotted in Figure 2.5 (b). It shows how much the spectrum is sharpened by using direct RF-filter boxes. Here, the terminology 'coherence peak' is used to represent the singular peak in BCS quasiparticle density of states. Note that it is used in a different context from the same word used to describe the peak near superconductivity transition temperature (T_C) in the temperature dependence of the microwave conductivity or NMR relaxation rate.

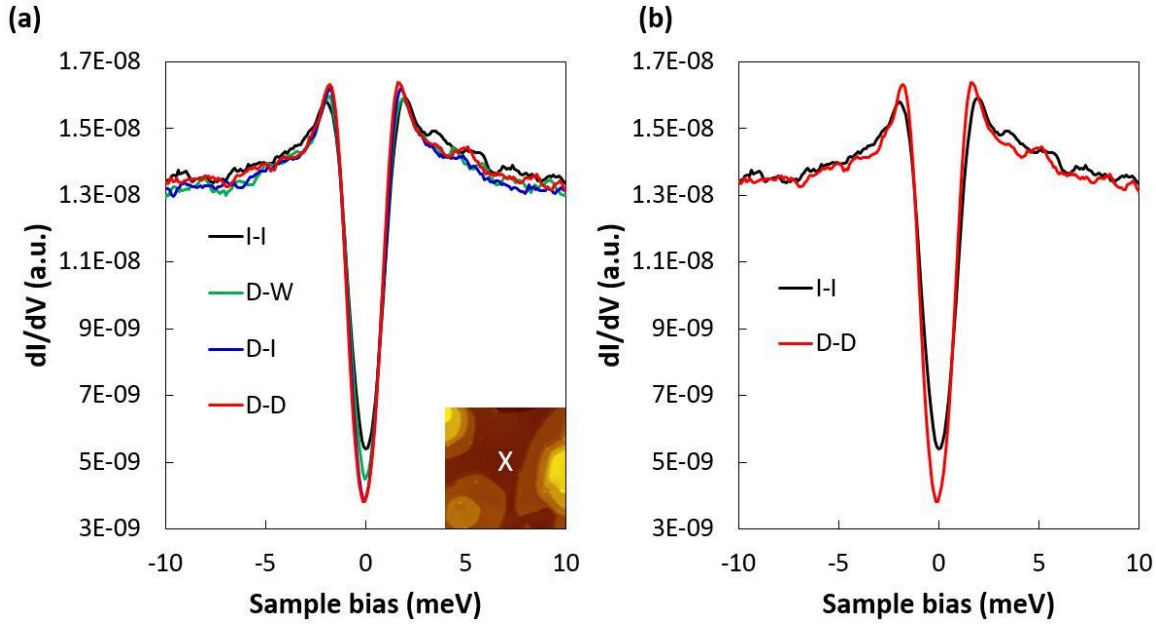

Figure 2.5: (a) Tunneling spectra measured with four different filter box configurations at a white X-mark on the inset STM image at T = 4.3K. The inset image is taken on 120 ML-Pb on 20 ML-Ag/Si(111)-(7 × 7) of 150 nm x 150 nm. (b) Tunneling spectra of I-I and D-D sets for clarity.

In order to estimate the system resolution, BCS curve fitting had been performed on the spectra in Figure 2.5 (b). In Figure 2.6 (a) and (b), the blue curves are the best fit of numerically calculated BCS curves with the same superconducting gap values of $\Delta(T = 4.3\ \mathrm{K}) = 1.035$ meV but with different system broadening factors of δ=0.55 meV and 0.23 meV, respectively. System broadening effect has been described by a convolution between the finite temperature quasiparticle density of states and a Gaussian distribution with the broadening factor. It reveals that D-D set gives more than a 50 % improvement of system resolution.

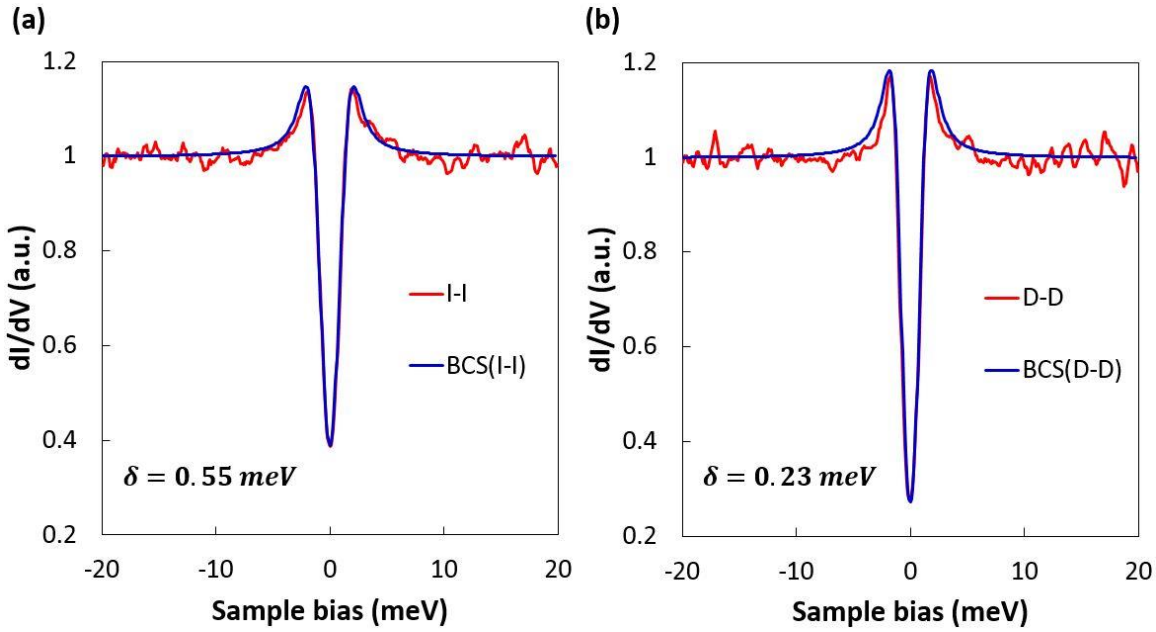

Figure 2.6: (a) and (b) shows a BCS fitting to the tunneling spectra of I-I and D-D, respectively. The BCS curves (blue) on (a) and (b) are calculated with the same $\Delta(T = 4.3\ \mathrm{K}) = 1.035\ \mathrm{meV}$ but with different system broadening factors of δ=0.55 meV and 0.23 meV, respectively.

2.2.2 Elimination of 60 Hz noise at bias signal

Another major electric noise source is the 60 Hz ground loop, which can also degrade the energy resolution of spectroscopy. In fact, STM control requires complicated electronics for handling the scanning tip, the feedback loop of tunneling current, and spectroscopy. Once electronics are combined together, the series of 60 Hz noise can appear, even when the individual electronics' outputs are clean with no background noise features.

In our case, 60 Hz noise appeared when the RHK STM controller of the SPM 100 and the lock-in amplifier of the SR830 DSP had been hooked up together, in order to apply conventional the lock-in technique to scanning tunneling spectroscopy instead of the numerical derivative of the tunneling spectrum. Bias signal from the STM controller

includes not only intentional signals of DC bias and AC lock-in modulation bias components, but also a number of unintentional AC components. The combined output signal was analyzed using an HP 35660A Dynamic Signal Analyzer. During the tests, the lock-in modulation frequency and bias were 550 Hz and 30 μV. As shown in Figure 2.7 (a) and (c), there absolutely exists a series of 60 Hz noise including unknown 170 Hz signal, although individual magnitudes are slightly weaker than lock in modulation bias; especially, lower frequency components are considerably strong compared with modulation bias.

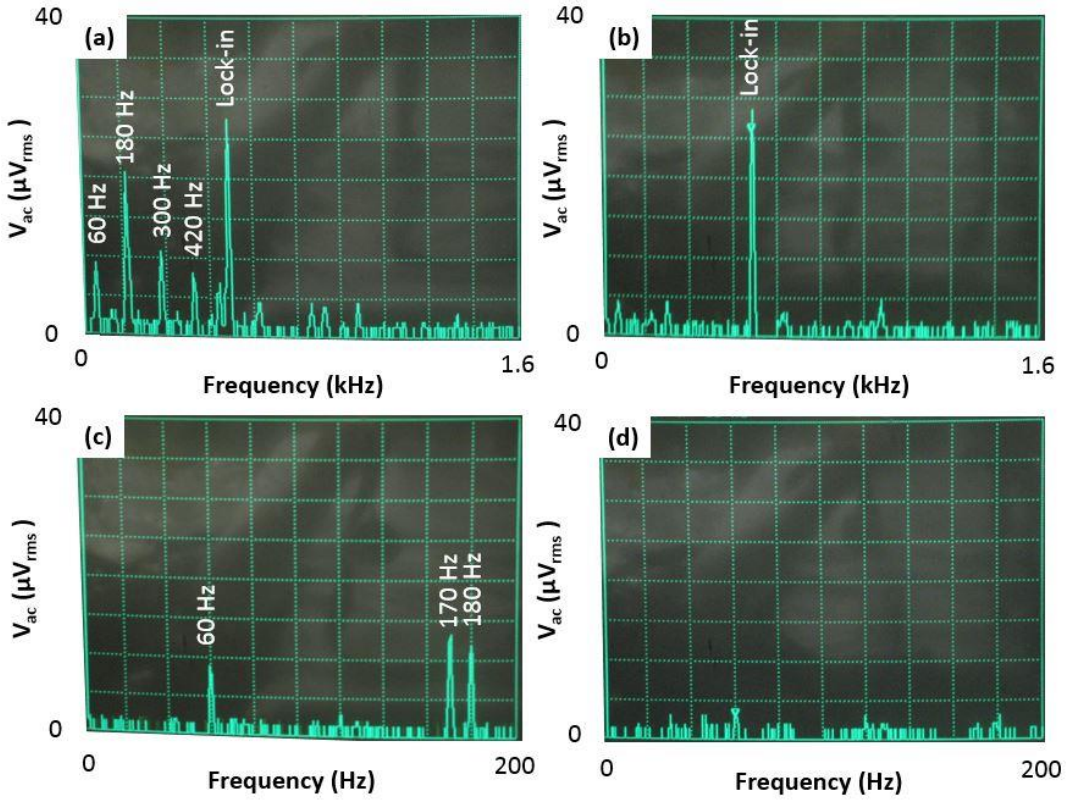

Figure 2.7: (a) and (c) are FFT spectra of bias signal taken before resolving the 60 Hz ground loop problem, whereas (b) and (d) are after resolving ground loop problem between the STM controller and the lock-in amplifier. The spectra of (a) and (b) were taken in the wide frequency range from 0 to 1.6 kHz; on the other hand, (c) and (d) were taken in the narrow range from 0 to 200 Hz.

After resolving the ground loop problem, all peaks related to the ground loop noise vanished from the FFT spectra. Comparison of (a) and (c) with (b) and (d) in Figure 2.7 obviously shows that the 60 Hz noise in the bias signal output had been fully suppressed to at least as low as the signal resolution limit of the HP 35660A Dynamic Signal Analyzer.

2.2.3 Lowering available system temperature

One approach to improve spectrum energy resolution is to reduce thermal broadening by lowing the system temperature. Originally, the LT-STM could reach the lowest temperature of T_{low} = 3.4 K by means of a direct-pumping liquid helium bath. This low temperature limit puts constraints on the abilities of our superconductivity studies; for example, T_c of materials should be higher than T_{low}. Even if the bulk T_c of a material is even higher than T_{low}, there is still a limit in observable lowest dimension of the material because superconductivity is normally suppressed when system dimension is reduced.

In order to lower T_{low}, the pumping line is first changed as the schematics shown in Figure 2.8, where the entire pumping lines are replaced with rigid SS tubes. If one uses a tube made of elastic materials, the elasticity of tube wall leads to a resonance with the fluctuation of the pump's vacuum-force. The resonance occurs because mechanical pumps typically have a certain periodic pumping rather than an ideal continuous pumping. The rigid pumping tube helps to prevent the resonance. In addition, the tube diameter was enlarged from 1/4 inch inside diameter (ID) to 1 inch ID to decrease the pumping load.

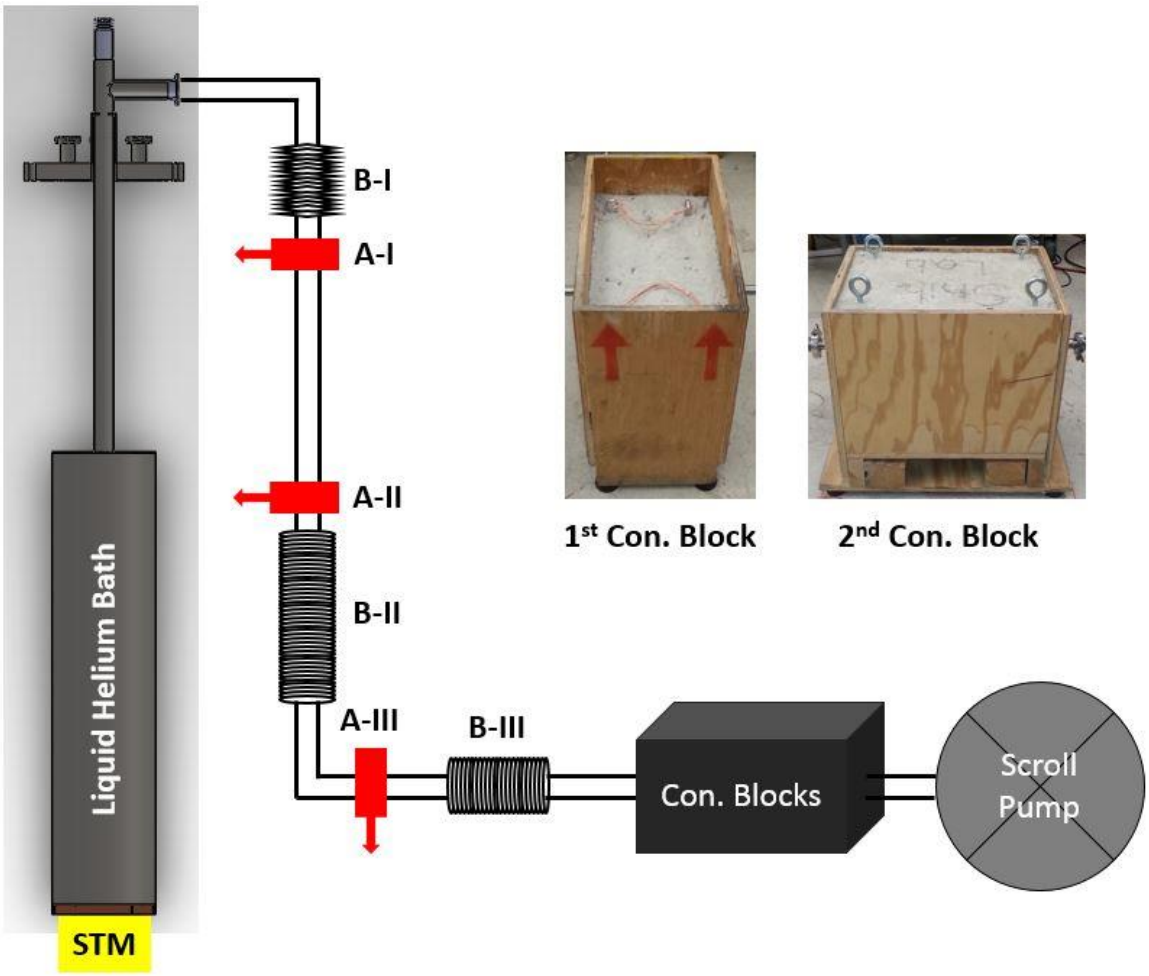

Figure 2.8: Schematics of the direct pumping liquid helium bath. The STM is attached to the copper bottom of the liquid helium bath. The pumping line is made of 1 inch ID SS tubes. The pumping line runs through two concrete blocks that are used as two-stage vibration blockers, located in front of the scroll pump whose pumping speed is 500 ℓ/min. Here, A and B stand for Anchor and Bellows, respectively.

Note that for STM application, vibration noise from cryostat must be considered as much as efforts of lowering the system's temperature. In this case, vibration noise mainly comes from the pump through the wall of the pumping lines. To reduce transferring the vibration noise, three bellows are put in between the SS tubes at the locations marked by bellows symbols (B-I, B-II, and B-III in Figure 2.8). Moreover, tubes are securely anchored

on the outside wall of STM vacuum chamber (A-I and A-II in Figure 2.8) and a leg of vibration isolation table (A-III in Figure 2.8). It prevents vacuum force from pulling the whole system in horizontal and vertical directions. In addition, there are two stages of heavy concrete blocks right in front of mechanical pump, shown in Figure 2.8. The heavy concrete blocks effectively shut out most of the mechanical vibration from the pump and prevents transfer of the mechanical vibration via the wall of pumping line toward STM chamber.

Finally, the available system temperature is now lowered to $T_{low,\ new}$ = 2.1 K from $T_{low,\ old}$ = 3.4 K. The first test was performed to determine superconducting transition temperature of two different types of 2 ML Pb film, which have different atomic structures of 1x1(type-I) and $\sqrt{3} \times \sqrt{3}$ (type-II) [15]. With our original set-up, the STM had difficulty studying this material, especially the type-II of 2 ML-Pb film, since its T_C was too low to acquire a series of temperature dependence superconducting gap data. As shown in Figure 2.9, we can get their reliable T_C with enough data points to fit that data to BCS curves: for type-I of 1x1, T_C = 4.85 K and for type-II of $\sqrt{3} \times \sqrt{3}$, T_C = 4 K.

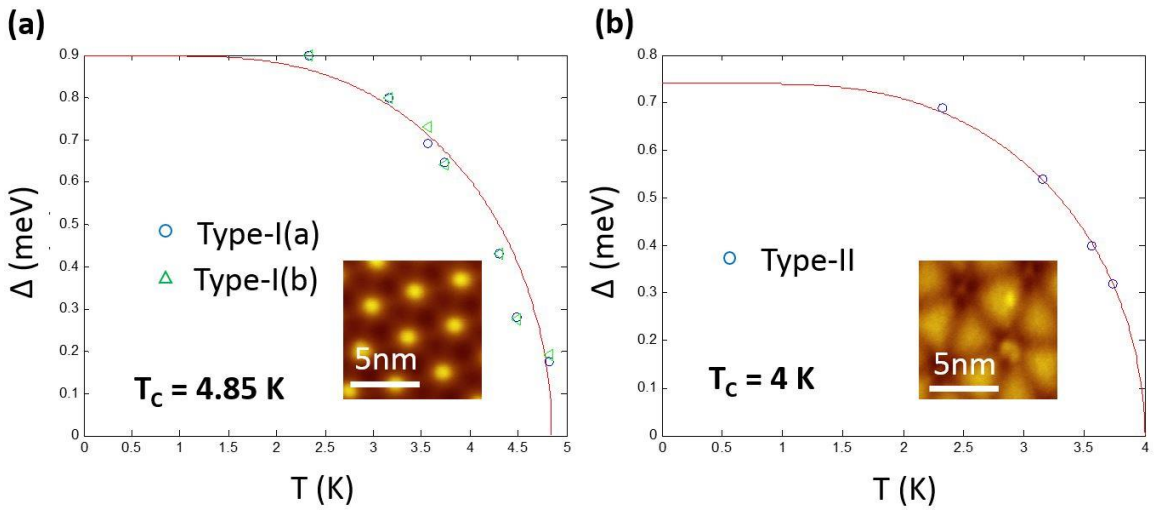

Figure 2.9: (a) and (b) BCS fit to superconducting gap data of type-I and -II of 2 ML Pb film. Insets are Moiré patterns acquired on type-I and –II of 2 ML Pb film.

The next test was carried out by taking a quasiparticle density of state spectrum on a 5ML Pb island on silicon (111) at $T = 2.1$ K. In Figure 2.10, the tunneling spectrum was taken using a conventional lock-in technique where the modulation voltage and frequency are 80 μV and $f = 550$ Hz, respectively. The spectrum shows obvious superconducting tunneling features with sharp coherence peaks and a deep zero-bias conductance; in addition, fine features show up on the shoulder part of the tunneling spectrum. They correspond to a phonon assisted quasiparticle tunneling feature. Each location is marked by a blue arrow in Figure 2.10.

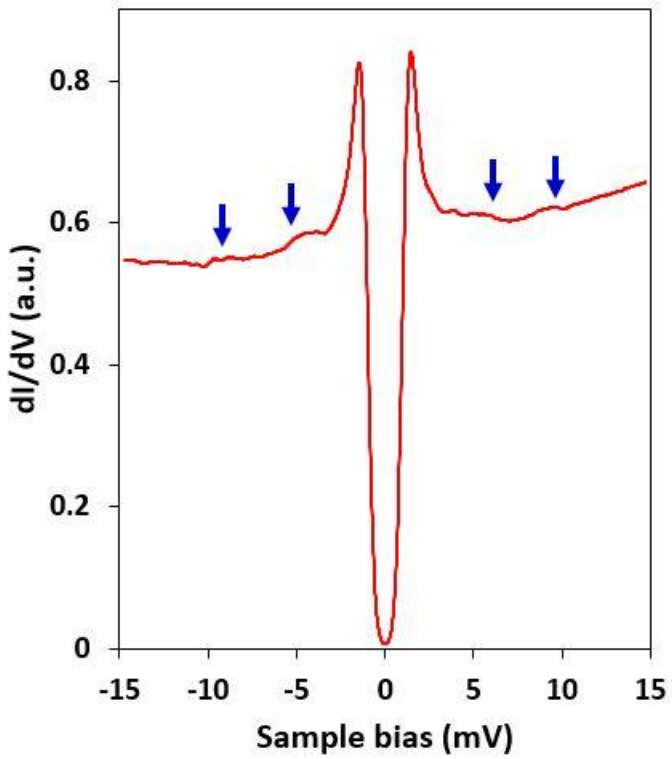

Figure 2.10: Tunneling spectrum taken on 5 ML Pb island at T = 2.1 K. The lock-in modulation voltage and frequency are 80 μV and f = 550 Hz, respectively. The spectrum show well developed coherence peaks and deep zero bias conductance. The blue arrows mark the locations corresponding to phonon assisted quasiparticle tunneling.

2.3 STM tip preparation

The tip plays a key role in achieving atomic scale spatial resolution and feedback loop stability in the STM, and the reproducible and best system energy resolution in STS. All STM tips are prepared by electrochemically etching a polycrystalline tungsten wire of 10 milli-inch diameter. In AC mode, around 2 V_{ac} was applied between W-wire and 5 % NaOH solution, like the schematics in Figure 2.11 (a). One end of the wire was caught by the drop box to protect the tip apex and the residual NaOH was removed with deionized

(DI) water and/or pure alcohol. Although the tip was etched, it was still exposed in air so that the surface formed a WO_3 layer. This layer can be removed by annealing the tip at a temperature over 725 ˚C under the condition of low oxygen content [17]. Our UHV-LT STM has a home-built e-beam stage [Figure 2.11 (b)] for *in-situ* tip annealing in order to remove the WO_3 layer from W-tip.

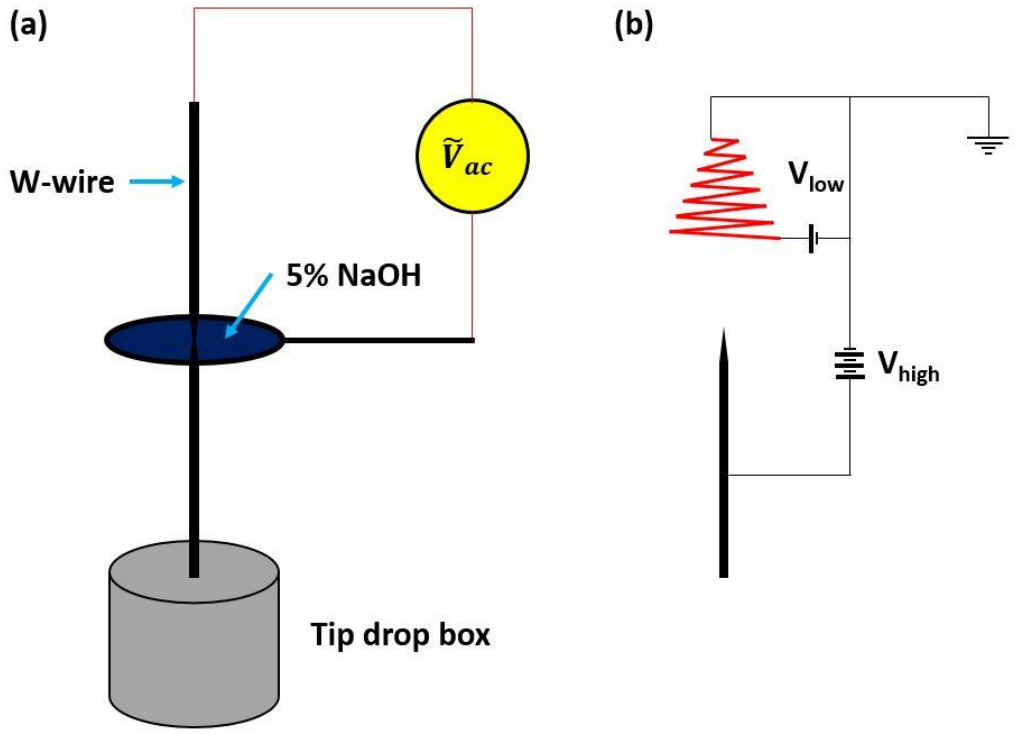

Figure 2.11: (a) Schematics of electrochemical etching. Etched lower part of the tungsten wire falls in the tip drop box. (b) E-beam tip cleaning. Electrons generated from a glowing tungsten filament are accelerated by a high voltage difference, and their kinetic energy is transferred to W-tip apex.

2.3.1 Field emission tip treatment

Empirically, W-tips, even after e-beam cleaning, often show non-reproducible spectra due to the highly structured density of states of the tips. As mentioned before, STM tips, especially for the purpose of spectroscopy, are desired to have a flat density of states, like a free electron metal. Such tip can give reliable and reproducible spectra purely revealing the sample properties. A special and reproducible tip treatment procedure had been developed by R. M. Feenstra *et al.* in 1987 [18], known as the field emission tip treatment. In this procedure, field emission current in the order of 1 – 2 μA is applied to the W-tip which is located at 100 nm away from a count metal electrode. Because of the high current density at the tip apex, local melting and then recrystallization happen at that point. At the same time, the emission current immediately drops to zero by the tip shortening. Since materials tend to have high surface density of atoms in nature, the surface density argument (Table 2.2) interprets that W(110) and W(111) facets are the preferred recrystallization form rather than W(100) and W(112). Fortunately, density of states of (110) and (111) are nearly free electron like around the Fermi level; whereas, for (100) and (112), highly structured owing to localized d_{z^2} surface states [19-22].

Tungsten (bcc)	(110)	(111)	(100)
n (cm^{-2})	1.41×10^{15}	1.15×10^{15}	9.98×10^{14}

Table 2.2: Surface density n of W-atoms to each directional facet.

2.4 Improvement of growth capability

As mentioned in Section 2.1, our original STM has only two available growth ports. In addition, its operation is fully dependent on STM operation. For example, when either growth or STM parts need maintenance, the whole system has to shut down at the same time and then perform entire recovery processes for both growth and LT-STM parts for two weeks. In order to make our system more flexible and to extend ability, two systems were built; for on-site growth, the extra growth chamber was built with independent maintenance ability. In addition, UHV-LT sample transfer vessel was made in order to facilitate the use of more diverse off-site instruments.

2.4.1 Extra growth camber for low temperature MBE growth

First, in order to improve on-site growth capability of the current STM, an extra growth chamber as shown in Figure 2.12 was built, which is equipped with three extra growth ports with built-in water cooling jackets, a quartz crystal thickness monitor, a cold finger, and a magnetic transfer arm. The base pressure of growth chamber is lower than 6 x 10^{-11} torr, achieved with an independent ion pump and TSP; in addition, sample growth stage is attached at the end of the magnetic transfer arm with a piece of copper block, which is able to be cooled down by mechanical contact with the cold finger. The cold copper block can keep samples at low temperatures during transferring the samples. Using the magnetic transfer arm, one can immediately transfer grown samples to STM for *in-situ* STM/S study under UHV and LT condition. Thus, it allows to avoid not only the introduction of unintentional impurity atoms into the samples due to long- and complicated- sample transferring method, but also the degradation of low dimensional structures due to heating up during moving samples.

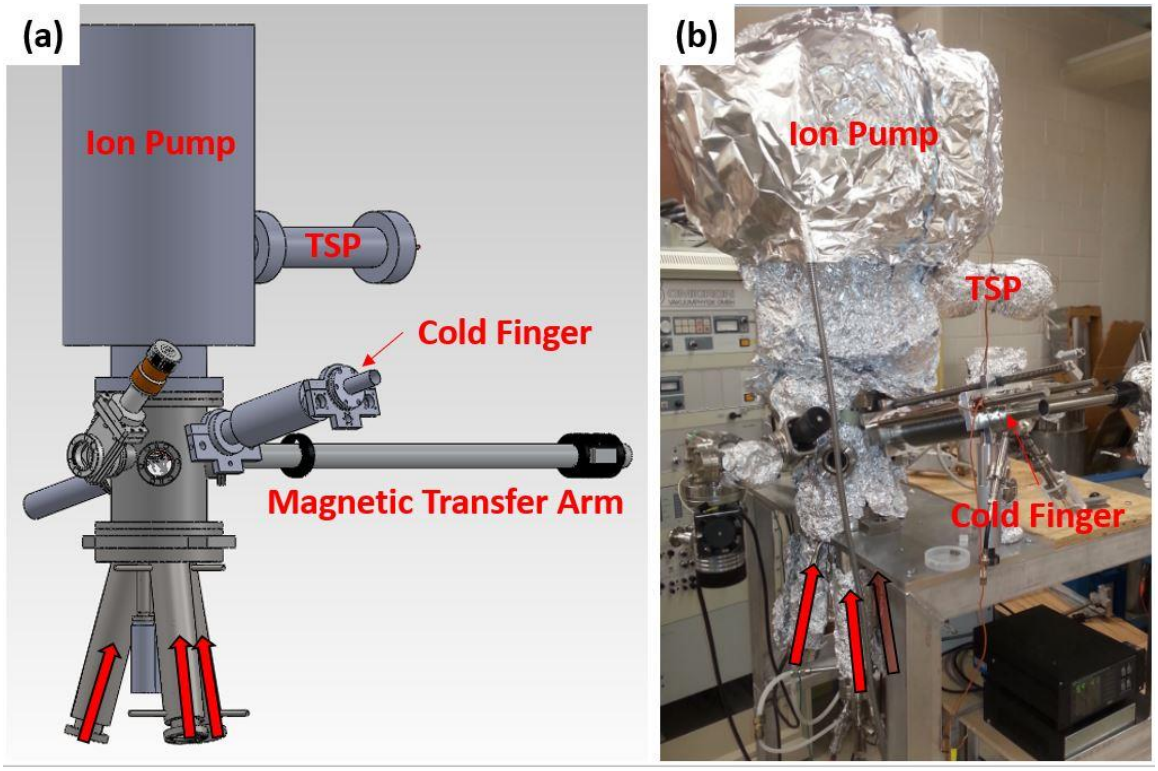

Figure 2.12: (a) and (b) are the drawing and photograph of extra growth chamber equipped with built-in water cooling jackets, respectively. The base pressure is lower than 6×10^{-11} torr using ion pump and TSP.

Since the growth chamber has its own load-lock system, one can conveniently connect it to a port of STM side when it is required to grow new samples. In order to reduce the transferring vibration noise, a bellow was placed between STM and the growth chamber. Even when this growth chamber is connected to STM, STM can take surface image and spectrum without any serious noise problem. In other words, one can easily disconnect it from STM with no disturbance, especially, when one needs to perform a fine STS study on a sample under the best environment.

Moreover, while maintaining the growth chamber, such as source preparations, one can keep STM running to study other samples regardless of the state of the growth chamber. If you consider that it takes around two weeks only to recover UHV and LT of our original

STM, it can save a tremendous time for both sample growth and its characterization using STM.

Current available source materials are indium (In) and germanium (Ge) using individual Knudsen cell, and ion (Fe), cobalt (Co), magnesium oxide (MgO) and copper (Cu) using four pocket Mantis e-beam evaporator to study the systems, such as one-dimensional or two-dimensional structures of magnetic atoms on conventional superconductors.

2.4.2 Mobile UHV-LT sample transfer vessel

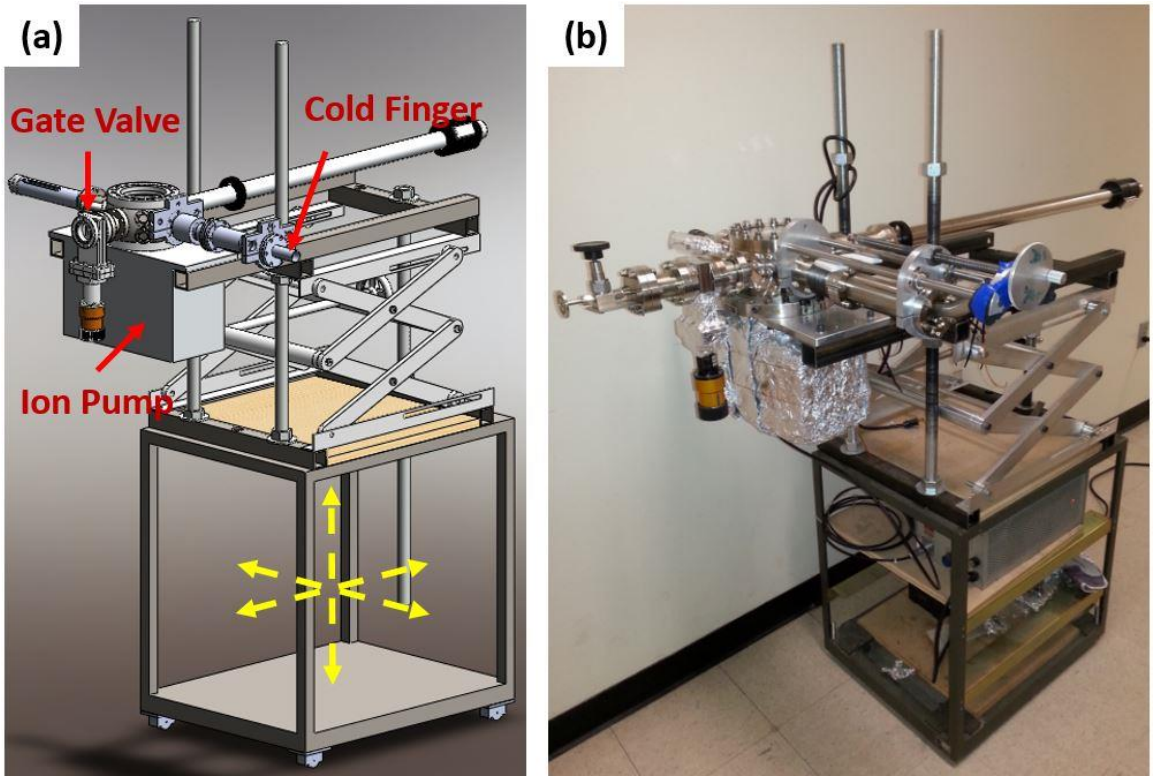

Figure 2.13: (a) and (b) are the drawing and photograph of sample transfer vessel.

Our experiments was necessary to build a system which can extend the accessible range to off-site instruments, such as MBE. For example, metal thin films on the semiconductor substrate often became de-wetting over a threshold temperature, usually lower than room temperature. In addition, the films, exposed in air, were degraded by formation of metal oxide layer on their surface, as well as contamination. Therefore, both LT and UHV conditions were required to resolve the sample degradation issues, happened while transferring samples from STM to instruments to do growth or measurement and vice versa.

In the study of quasi-2D superconductor phase rigidity, the global flat Pb film of 5 ML began to de-wet at the temperature in the range of 150 K ~ 200 K and to form thicker islands. However, in order to perform *ex-situ* macroscopic length scale measurements, such as S-SQUID, superfluid, and magneto-resistance, it was necessary to make the superconducting thin film sustain at least at room temperature in air.

Figure 2.13 shows the complete design and its real photograph of the mobile LT-UHV sample transfer vessel. It is designed to keep samples at a temperature in the range of 120 K ~ 150 K under UHV condition while moving samples from STM to MBE. In this way, germanium (Ge) layer can be grown to protect global flat ultra-thin superconducting films. Since the vessel has its own wheels, it is easy to move the vessel with a sample between the systems. The scissor-like lift jack makes it easy to adjust the level of the connection port and then possible to connect the vessel to load-lock of any UHV system. The gate valve and ion pump of 60 ℓ/m pumping speed allow to keep the pressure inside of transfer vessel to be UHV, 1×10^{-10} torr. The cold finger is needed to lower the temperature at sample acceptor by flowing liquid nitrogen through it.

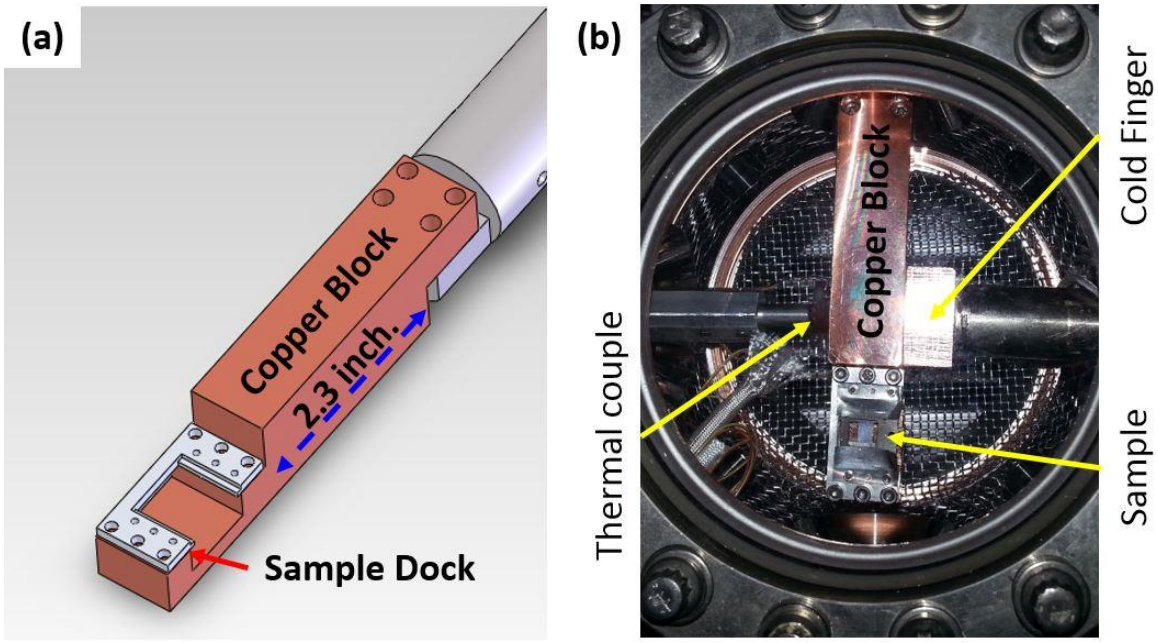

Figure 2.14: (a) and (b) are the drawing and photograph of non-rotatable sample acceptor design.

As shown in Figure 2.14, the non-rotatable sample acceptor is attached to the copper block of 2.3 inch × 1 inch as a thermal sink. Cooling test was performed with a demo sample at the sample acceptor. A thermocouple was attached to the demo sample during the tests for both designs of rotatable and non-rotatable sample acceptors. After cooling down for three hours, the demo sample temperature decreased to below 140 K for both designs. Then the cold finger was detached from the copper block to calibrate temperature change at the demo sample without cooling power. Figure 2.15 shows the temperature change at a demo sample as a function of time for both sample acceptors. Even after 50 minutes, temperature at a demo sample was still below 150 K which was low enough to prevent de-wetting of thin films and long enough to move the transfer vessel between STM and MBE.

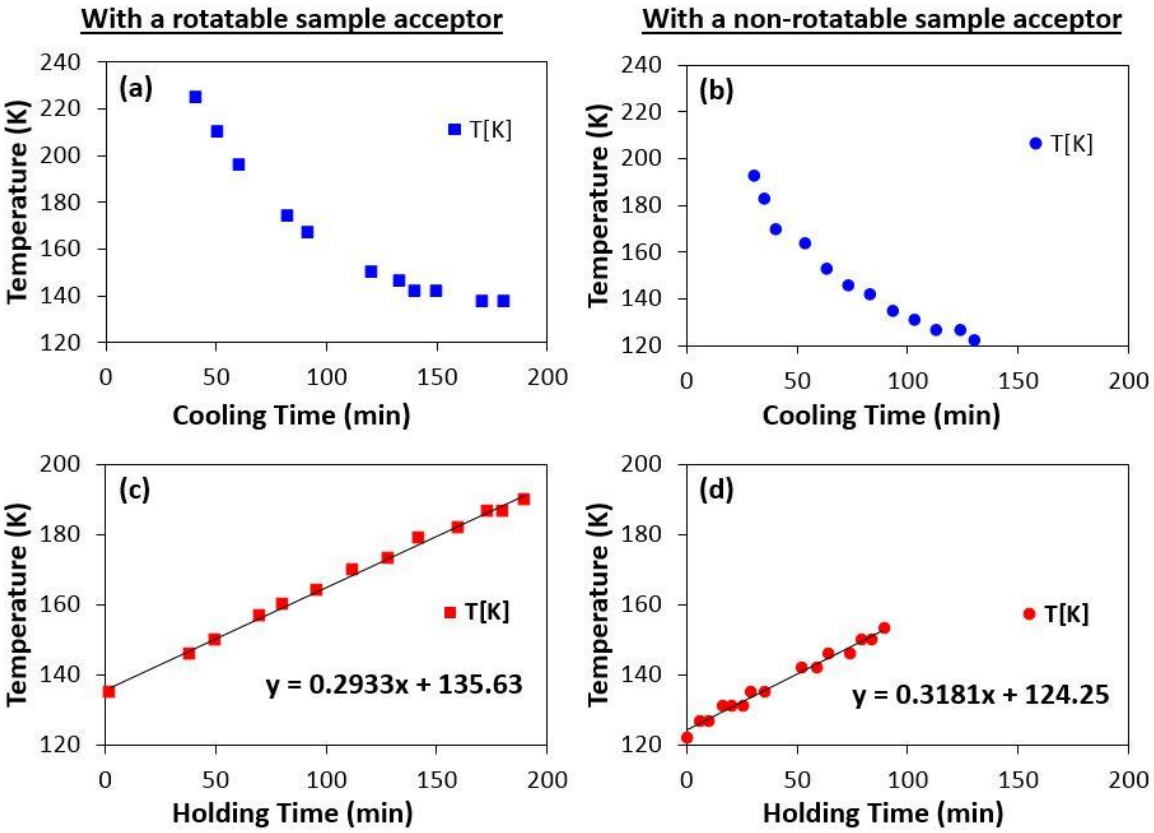

Figure 2.15: (a) and (c) are cooling and holding test results for rotatable sample accepter, respectively; (b) and (d) for non-rotatable sample acceptor. The holding temperature changes tend to linearly increase like the prediction lines in a few hours.

The practical test was carried out by growing 3nm Ge capped global flat 2 ML Pb film. 2 ML Pb film is the most fragile and thinnest global flat Pb film which can be grown in our lab. De-wetting of 2 ML Pb film happens at $T \sim 180$ K. The prepared Pb film, like Figure 2.16 (a), was transferred to MBE equipped with Ge Knudsen cell at LT using the transfer vessel. The comparison between Figure 2.16 (a) and (b) reveals that not only the transfer vessel is working well as what we expect during sample transfer, but also Ge capping layer is just following the surface of underlying layer. Here, Ge capping layer works only as protecting layer without deforming the underlying 2 ML Pb film.

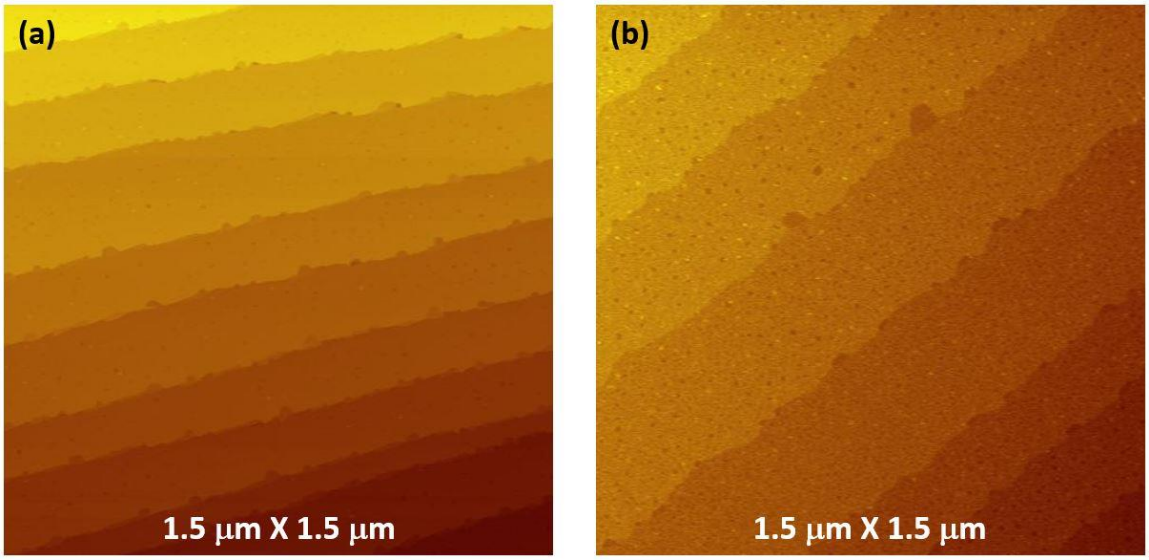

Figure 2.16: (a) is the STM image taken on global flat 2ML Pb film of 1.5 μm × 1.5 μm; whereas (b) is taken after Ge capping.

Chapter 3: Superconductivity

In 1911, superconductivity was discovered by H. K. Onnes following his success of the first liquefaction of Helium gas on July 10th, 1908; like Figure 3.1 (a), Onnes observed the resistance drop of mercury from ~ 0.1 Ω to unmeasurably small resistance of less than 10^{-5} Ω, as temperature decreased and passed the critical temperature of T = 4.20 K ± 0.01 K [23-25].

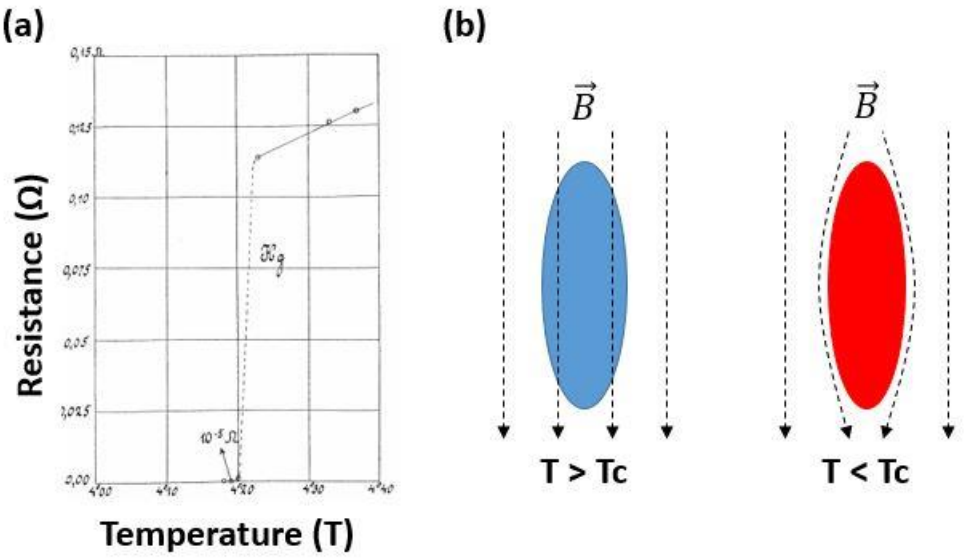

Figure 3.1: (a) Resistance of mercury as a function of temperature measured by H. K. Onnes. Superconducting transition happens at T = 4.2 K (adopted from ref. [25]). (b) Schematics of magnetic flux change before (left) - and after (right) - superconducting transition of material.

In addition to perfect conductivity, perfect diamagnetism was discovered by W. Meissner and R. Ochsenfeld in 1933 [26]. As shown in Figure 3.1 (b), when a material in magnetic field undergoes superconductor transition, the material expels inside magnetic field by inducing a surface current, which cannot be explained with perfect conductivity. But, if the magnetic field equals to condensation energy of a superconducting state in zero

field, there is no more Meissner effect and superconducting phase is destroyed. Here, the critical magnetic field is

$$f_{super}(T) - f_{normal}(T) = -\frac{H_c^2(T)}{8\pi}, \tag{3.1}$$

where f_{normal} and f_{super} are Helmholtz free energies per unit volume at each phase.

3.1 London penetration depth and Pippard coherence length

Both superconductivity hallmarks were theoretically described in 1935 by F. London and H. London with the following equations [27],

$$\vec{\mathbf{E}} = \frac{\partial}{\partial t}(\Lambda \overrightarrow{\boldsymbol{J_s}})$$
$$-\frac{\mathbf{1}}{\boldsymbol{c}}\vec{\mathbf{H}} = \vec{\nabla} \times (\Lambda \overrightarrow{\boldsymbol{J_s}})$$
$$\Lambda = \frac{m}{n_s e^2}\left(= \frac{4\pi\lambda^2}{c^2}\right), \tag{3.2}$$

where n_s, c, and λ are the number density of superconducting electrons, speed of light, and penetration depth, respectively. The first London equation is like Newton's second law for superconducting electrons. It implies that, if electric field $\vec{\mathbf{E}}$ is zero, supercurrent become steady flow without loss. Besides, the second London equation is induced to

$$\nabla^2 \overrightarrow{\boldsymbol{H}} = \frac{\overrightarrow{\boldsymbol{H}}}{\lambda^2}$$
$$\lambda = \left(\frac{mc^2}{4\pi n_s e^2}\right)^{1/2}, \tag{3.3}$$

which reflects the exponential decay of magnetic field as Meissner effect in superconductor.

From Pippard's nonlocal generalization of London equation, $\overrightarrow{\boldsymbol{J_s}} = -\overrightarrow{\boldsymbol{A}}/\Lambda c$, he introduced another characteristic length of superconductor, so called coherence length. The coherence length represents the smallest size of wave packet able to be formed by

superconducting charge carriers. Uncertainty principle of $\Delta x \Delta p \gtrsim \hbar$ within the momentum range of $\Delta p \approx kT_c/v_F$ at Fermi level leads to the coherence length,

$$\xi_0 = a\frac{\hbar v_F}{kT_c}, \tag{3.4}$$

with a = 0.18 within BCS theory [28]. In the presence of scattering, the practical coherence length ξ is

$$\frac{1}{\xi} = \frac{1}{\xi_0} + \frac{1}{\ell}, \tag{3.5}$$

where ℓ is the mean free path. It had been found to fit experimental data on superconducting aluminum with a = 0.15 in Equation (3.4) [29].

3.2 Ginzburg-Landau theory

In 1950, Ginzburg-Landau (GL) theory had been introduced with a pseudo-wavefunction as a complex order parameter $\psi(\vec{\mathbf{r}}) = |\psi(\vec{\mathbf{r}})|\exp(i\theta(\vec{\boldsymbol{r}}))$ to represent superconducting electrons [30]. The magnitude of the complex order parameter is related with the local density of superconducting electrons, $n_s(\vec{\boldsymbol{r}}) = |\psi(\vec{\boldsymbol{r}})|^2$. The celebrated GL differential equations are

$$\alpha(T)\psi(\vec{\mathbf{r}}) + \beta(T)|\psi(\vec{\mathbf{r}})|^2\psi(\vec{\mathbf{r}}) + \frac{1}{2m^*}\left(\frac{\hbar}{i}\vec{\nabla} - \frac{e^*}{c}\vec{\boldsymbol{A}}(\vec{\mathbf{r}})\right)^2 \psi(\vec{\mathbf{r}}) = 0 \tag{3.6}$$

and

$$\overrightarrow{\boldsymbol{J_s}} = \frac{e^*\hbar}{2m^*i}\left(\psi^*(\vec{\mathbf{r}})\vec{\nabla}\psi(\vec{\mathbf{r}}) - \psi(\vec{\mathbf{r}})\vec{\nabla}\psi^*(\vec{\mathbf{r}})\right) - \frac{e^{*2}}{m^*c}|\psi(\vec{\boldsymbol{r}})|^2\vec{\boldsymbol{A}}(\vec{\mathbf{r}}) \tag{3.7}$$

or

$$\begin{aligned}\overrightarrow{\boldsymbol{J_s}} &= \frac{e^*}{m^*}|\psi(\vec{\boldsymbol{r}})|^2\left(\hbar\vec{\nabla}\theta(\vec{\mathbf{r}}) - \frac{e^*}{c}\vec{\boldsymbol{A}}(\vec{\mathbf{r}})\right)\\ &= e^*|\psi(\vec{\boldsymbol{r}})|^2\overrightarrow{\boldsymbol{v_s}}\end{aligned} \tag{3.7′}$$

L. P. Gor'kov showed that GL theory is a rigorous limiting case of BCS theory in 1959 [31]; especially, limited to temperature sufficiently near *T*c and to slow varying ψ and $\vec{\boldsymbol{A}}(\vec{\mathbf{r}})$. In fact, GL theory makes it possible to handle both the nonlinear effects of strong fields and the spatial variation of $n_s(\vec{\boldsymbol{r}})$, in contrast to London theory for nonlocal superconductivity.

3.3 BCS theory

Microscopic theory of superconductivity, also known as the BCS theory, was established by J. Bardeen, L. N. Cooper, and J. R. Schrieffer based on their epoch-making pairing theory in 1957 [32]. In the pairing theory, interaction between electrons mediated by phonons can be attractive in contrast to repulsive Coulomb interaction between electrons. No matter how small the strength of net attractive interaction is, it causes the formation of bound electron pairs in a degenerate Fermi gas in which electrons have equal magnitude and opposite direction of momentum and spin; so called Cooper pairs [33]. The important role of electron-phonon interaction in the pairing theory had experimentally been confirmed by the discovery of the isotope effect for mercury as $T_c \propto 1/\sqrt{M}$, as shown in Figure 3.2 [34-36]. In addition, as mentioned in Pippard coherence length for a pure superconductor, using uncertainty principle estimates that the size of a Cooper pairs is in the order of $\xi_{0,BCS} = \hbar v_F/\pi\Delta_0$ (≈100 nm order). Since the size is much longer than interatomic distance of order of 0.1 nm ~ 0.4 nm, Cooper pairs have to be highly overlapping each other.

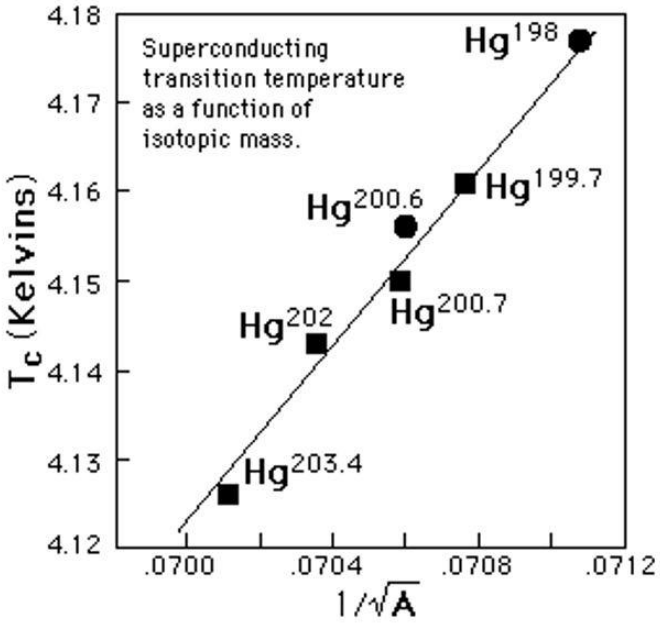

Figure 3.2: Isotopic effect of mercury on superconducting transition temperature (adopted from ref. [34-36]). Indeed, T_C is proportional to the inverse square root of atom mass, $T_c \propto 1/\sqrt{A}$.

3.3.1 Temperature dependence of superconducting gap

The bound electron states in the degenerated Fermi gas had been described by the BCS ground state wave function,

$$|\psi_\theta\rangle = \prod_{\vec{k}} \left(|u_{\vec{k}}| + |v_{\vec{k}}| e^{i\theta} c^*_{\vec{k}\uparrow} c^*_{-\vec{k}\downarrow}\right) |\phi_0\rangle, \tag{3.8}$$

where $|u_{\vec{k}}|^2 + |v_{\vec{k}}|^2 = 1$. $|\phi_0\rangle$ is the singlet wave function in Fermi sea and $c^*_{\vec{k}\uparrow}$ is creation operator which means creating an electron of momentum $\vec{k}$ and spin up state. $|v_{\vec{k}}|^2$ represents the possibility for electrons to occupy the pairing state ($\vec{k}\uparrow, -\vec{k}\downarrow$), whereas $|u_{\vec{k}}|^2$ represents the possibility of not occupying the pairing state. The specific values of $|u_{\vec{k}}|^2$, $|v_{\vec{k}}|^2$, and θ are determined by solving the pairing Hamiltonian,

$$H = \sum_{\vec{k},\sigma} \epsilon_{\vec{k}} n_{\vec{k},\sigma} + \sum_{\vec{k},\vec{l}} V_{\vec{k},\vec{l}} c^*_{\vec{k}\uparrow} c^*_{-\vec{k}\downarrow} c_{-\vec{l}\downarrow} c_{\vec{l}\uparrow}, \tag{3.9}$$

where $\epsilon_{\vec{k}} (= \xi_{\vec{k}} + \mu)$ is the single-particle energy and $V_{\vec{k},\vec{l}}$ is the interaction potential. Applying a self-consistent field method leads to the excitation energy of a fermion quasiparticle of $\vec{p} = \hbar\vec{k}$ and the minimum excitation energy of $\vec{k}$, so called energy gap,

$$\begin{aligned} E_{\vec{k}} &= \sqrt{\xi^2_{\vec{k}} + \left|\Delta_{\vec{k}}\right|^2} \\ \Delta_{\vec{k}} &= -\sum_{\vec{l}} V_{\vec{k},\vec{l}} \langle c_{-\vec{l}\downarrow} c_{\vec{l}\uparrow} \rangle. \end{aligned} \tag{3.10}$$

At the finite temperature, the fermion quasiparticle excitation also follows Fermi statistics. The energy gap is induced to

$$\begin{aligned} \Delta_{\vec{k}} &= -\sum_{\vec{l}} V_{\vec{k},\vec{l}} u^*_{\vec{l}} v_{\vec{l}} \left[1 - 2f\left(E_{\vec{l}}\right)\right] \\ &= -\sum_{\vec{l}} V_{\vec{k},\vec{l}} \frac{\Delta_{\vec{l}}}{2E_{\vec{l}}} tanh \frac{\beta E_{\vec{l}}}{2}, \end{aligned} \tag{3.11}$$

where $f\left(E_{\vec{l}}\right) = 1/\left(1 + \exp(\beta E_{\vec{l}})\right)$ is Fermi distribution function and $\beta = 1/k_B T$. Using the BCS approximation of $V_{\vec{k},\vec{l}} = -V$, the energy gap becomes to be independent of wave vector, $\Delta_{\vec{k}} = \Delta_{\vec{l}} = \Delta$. Finally, the self-consistency condition becomes

$$\frac{1}{V} = \frac{1}{2} \sum_{\vec{k}} \frac{tanh\left(\beta E_{\vec{k}}/2\right)}{E_{\vec{k}}}, \tag{3.12}$$

where

$$E_{\vec{k}} = \sqrt{\xi^2_{\vec{k}} + \Delta^2}. \tag{3.13}$$

Here, the energy gap $\Delta(T)$ includes the temperature dependence and it is numerically evaluated by equation (3.12). The integral form is

$$\frac{1}{N(0)V} = \int_0^{\hbar\omega_c} \frac{tanh \frac{1}{2}\beta\sqrt{\xi^2 + \Delta^2}}{\sqrt{\xi^2 + \Delta^2}} d\xi. \tag{3.14}$$

Figure 3.3 (a) shows the temperature dependence of reduced energy gap as a function of reduced temperature from equation (3.14). Since $\Delta(T_c) = 0$ at T_c, the integral on the right side is evaluated to $\ln(1.13\,\hbar\omega_c/k_B T_c)$, resulting

$$k_B T_c = 1.13\hbar\omega_c e^{-1/N(0)V}. \tag{3.15}$$

Zero temperature BCS superconducting gap is $\Delta_0 \approx 2\hbar\omega_c \exp(-1/N(0)V)$ in weak-coupling limit; therefore, the ratio of $2\Delta(0)$ to $k_B T_c$ is given by a constant value,

$$\frac{2\Delta_0}{k_B T_c} = 3.528. \tag{3.16}$$

It is reasonable value because experimental values for different materials fall in the range from 3.0 to 4.5; especially, most of the values are gathered around the BCS value of 3.5 [Figure 3.3 (b)] [36].

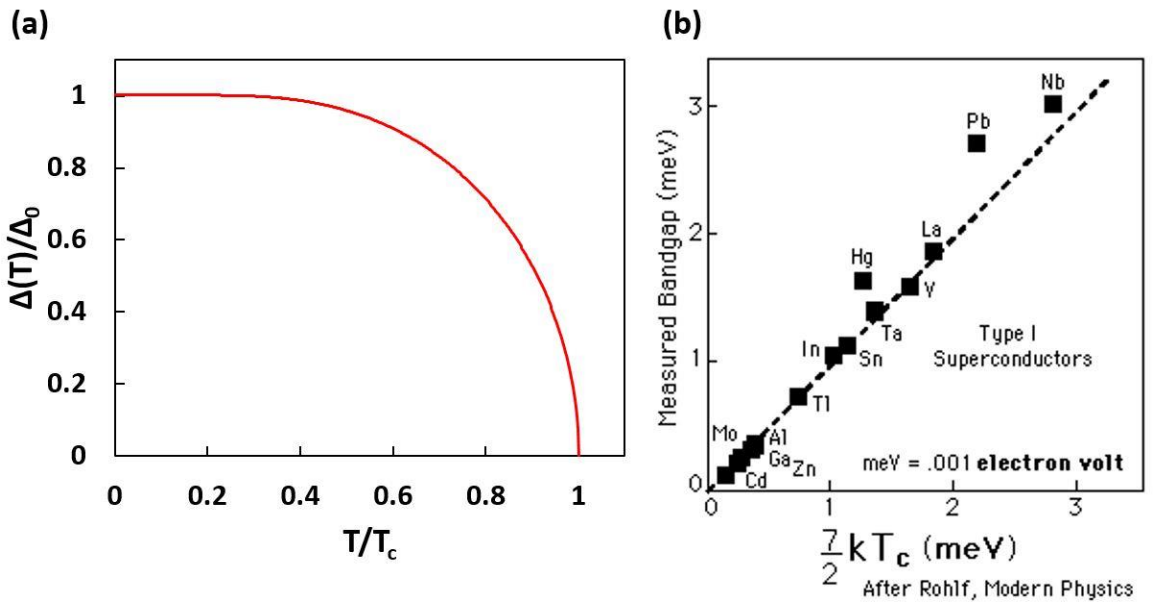

Figure 3.3: (a) The universal curve of the reduced superconducting energy gap as a function of the reduced temperature with the BCS value of 3.5. (b) Measured superconducting energy gaps of Type-I superconductors with respect to scaled critical temperatures (adopted from ref. [36]). The dotted line represents BCS prediction.

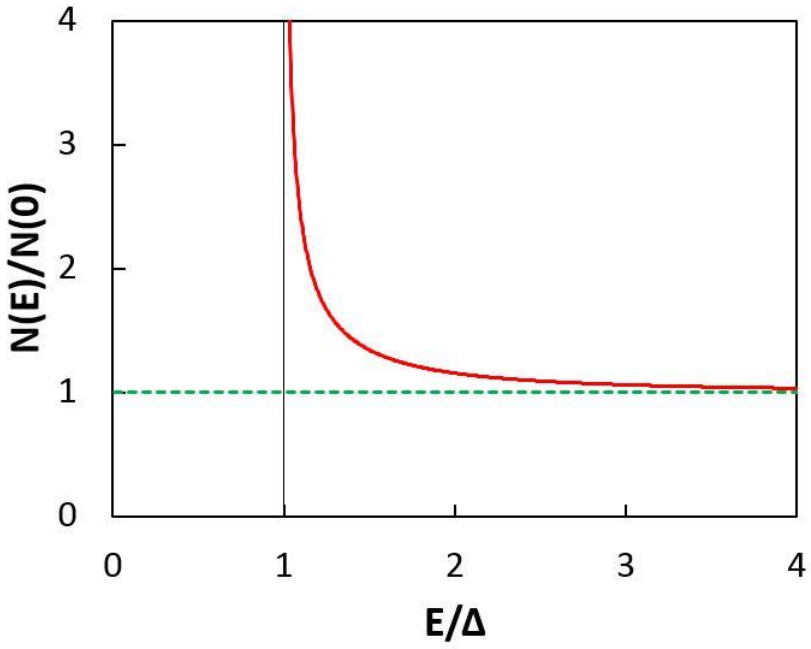

Figure 3.4: Quasiparticle density of states for both superconducting state (red solid curve) and normal state (green dotted line).

3.3.2 Quasiparticle density of states

The quasiparticle excitation energies $E_{\vec{k}}$ in superconducting states and ones $\xi_{\vec{k}}$ in the normal states, measured from Fermi level, have the relation of equation (3.13). One-to-one correspondence between fermion quasiparticles in superconducting state and electrons in normal state implies $N_s(E)dE = N_n(\xi)d\xi$. Since the interesting energy range is as small as the order of *meV*, one can assume normal state density as constant, $N_n(\xi) = N(0)$. Consequently, quasiparticle density of states is

$$\frac{N_s(E)}{N(0)} = \frac{d\xi}{dE} = \begin{cases} \dfrac{E}{\sqrt{E^2 - \Delta^2}} & (E > \Delta) \\ 0 & (E > \Delta) \end{cases}. \tag{3.18}$$

As shown in Figure 3.4, it reveals a divergent density of states just above energy gap in order to conserve the total number of states during the phase transition.

3.3.3 Normal metal-insulator-superconductor tunneling

Tunneling current from initial- to final-electrodes is proportional to the number of occupied initial states $N_i(E)f(E)$ and one of unoccupied final states $N_f(E+eV)[1-f(E+eV)]$ as well as the square of tunneling matrix elements.

$$I_{i\to f} \propto \int_{-\infty}^{\infty} \left|M_{i\leftrightarrow f}\right|^2 N_i(E)f(E)N_f(E+eV)[1-f(E+eV)]dE \qquad (3.19)$$

Let us assume that $\left|M_{i\to f}\right|^2$ is a constant and then consider the reverse tunneling current, the net current between two electrodes (1 and 2) at a bias of V becomes

$$I_{net}(V) \propto \left|M_{i\leftrightarrow f}\right|^2 \int_{-\infty}^{\infty} N_1(E)N_2(E+eV)[f(E)-f(E+eV)]dE \qquad (3.20)$$

When one side of the electrodes is a superconducting metal, the tunneling current can be written as

$$\begin{aligned} I_{ns} &\propto |M_{1\leftrightarrow 2}|^2 N_{n1}(0) \int_{-\infty}^{\infty} N_{s2}(E)[f(E)-f(E+eV)]dE \\ &\propto |M_{1\leftrightarrow 2}|^2 N_{n1}(0)N_{n2}(0) \int_{-\infty}^{\infty} \frac{N_{s2}(E)}{N_{n2}(0)}[f(E)-f(E+eV)]dE\,. \end{aligned} \qquad (3.21)$$

The differentiation of Equation (3.21) with respect to V leads to the differential conductance at a certain bias,

$$\begin{aligned} \left.\frac{dI_{ns}}{dV}\right|_V &\propto \int_{-\infty}^{\infty} \frac{N_{s2}(E)}{N_{n2}(0)}\left[-\frac{\partial f(E+eV)}{\partial V}\right]dE \\ &\propto \int_{\Delta}^{\infty} \frac{E}{\sqrt{E^2-\Delta^2}}\left[-\frac{\partial f(E+eV)}{\partial V}\right]dE\,. \end{aligned} \qquad (3.22)$$

It means that experimental measurement of differential conductance as a function of an applied bias reveals thermally broadened density of states of the superconducting electrode due to a finite temperature, still lower than the critical temperature T_c. Figure 3.5 is a

numerical calculation result of Equation (3.22) as a function of bias at different temperatures.

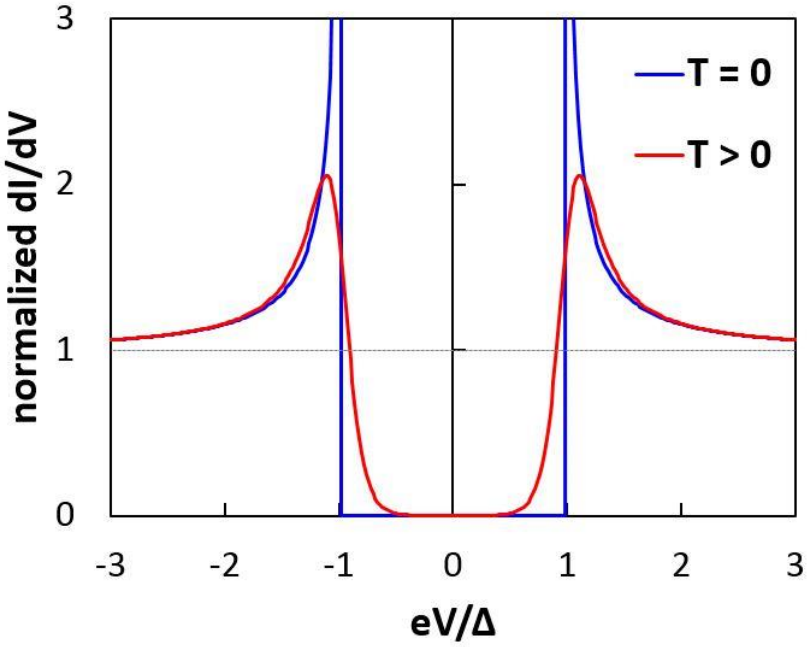

Figure 3.5: Differential conductance of tunneling current as a function of bias. Blue and red solid curves are of normalized dI/dV at zero and a finite-temperatures, respectively.

3.4 Temperature dependence of magnetic field penetration depth

3.4.1 Penetration depth within BCS

From Equation (3.3), penetration depth is defined as $\lambda \equiv \frac{1}{H(z=0)} \int_0^\infty H(z)dz$. λ serves to determine the density of superconducting electrons using the relationship of $n_s \propto \lambda^{-2}$. Within BCS theory, the response of superconductor to weak magnetic fields in low frequency ($\hbar\omega < 2\Delta$) can be considered with a perturbation term in BCS Hamiltonian,

$$H_1 = \frac{ie\hbar}{2mc}\sum_j \nabla_j \cdot \vec{\boldsymbol{A}} + \vec{\boldsymbol{A}} \cdot \nabla_j \tag{3.23}$$

where $\vec{\boldsymbol{A}}(\vec{\mathbf{r}})$ is a transverse vector potential ($\vec{\boldsymbol{B}} = \vec{\nabla} \times \vec{\boldsymbol{A}}$), including the screening effects related to superfluid responses. In the low frequency limit, the superfluid response has the analytic form [37]

$$\frac{\lambda^2(0)}{\lambda^2(T)} = \left[1 - 2\int_{\Delta}^{\infty}\left(-\frac{\partial f}{\partial E}\right)\frac{E}{\sqrt{E^2 - \Delta^2}}dE\right], \tag{3.24}$$

which is for a pure superconductor in local limit of $\lambda \ll \xi$. The second term of Equation (3.24) shows that quasiparticle plays an important role in the suppression of $1/\lambda^2$ (or supercurrent). It gives negative contribution in total response because the excited quasiparticles carry a net current in the reverse direction.

In dirty superconductor in which mean free path is shorter than coherence length ($l < \xi$), the temperature dependence of penetration depth can be rewritten by

$$\frac{\lambda^2(0)}{\lambda^2(T)} = \frac{\Delta(0)}{\Delta(T)} tanh^{-1}\left(\frac{\Delta(T)}{2k_B T}\right). \tag{3.135}$$

Figure 3.6 is numerical calculation of normalized inverse penetration depth as a function of reduced temperature in the limit of pure and dirty superconductors.

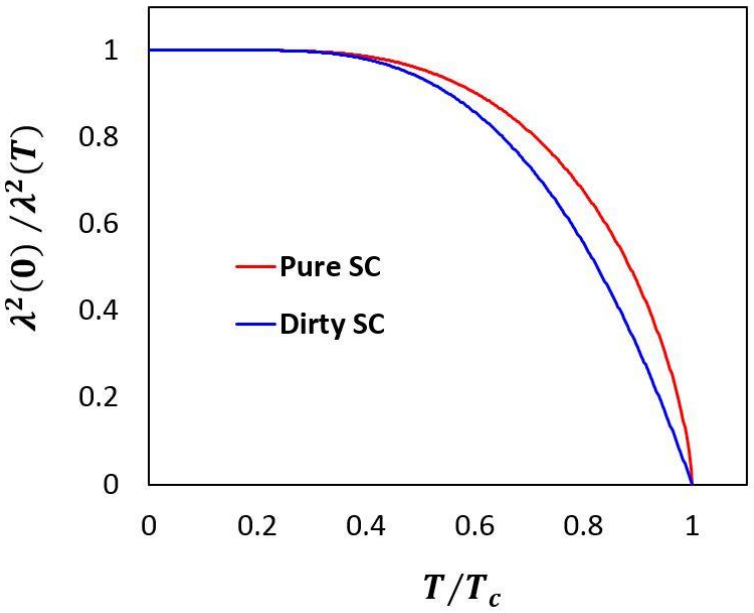

Figure 3.6: Temperature dependence of penetration depth within BCS theory for pure (red) and dirty (blue) superconductors.

Chapter 4: Remarkable superfluid rigidity in ultrathin 2D superconductor

Two-dimensional (2D) superconductors are supposed to be fragile because phase fluctuations can disrupt the long-range order of Cooper pairs [38-53]. The studies on epitaxially grown conventional superconductor in quasi-2D regime showed a surprising result [40-42, 44, 54-56]. Recent scanning tunneling spectroscopy (STS) on epitaxially grown Pb films, however, has shown that Cooper pair binding remains relatively robust until the film thickness approaches atomic limit, as shown in Figure 4.1 (a) [54], whereas macroscopic measurements appeared to show significant suppression of T_C on similarly prepared films, supporting the notion of fragility in superconductivity due to the loss of the long range phase coherence, as shown in Figure 4.1 (b) [40, 42].

Here, superfluid phase rigidity in epitaxially grown ultrathin Pb films is proven by the results of four different length scale measurements, STS, scanning Superconducting Quantum Interference Device (S-SQUID), double-coil mutual inductance, and magneto-transport measurements with the similar T_C. In addition, magneto-transport shows remarkably high parallel critical field over the Clogston-Chandrasehkar limit. Studies of thicker films show that orbital contribution to critical field is scaled as the inverse film thickness.

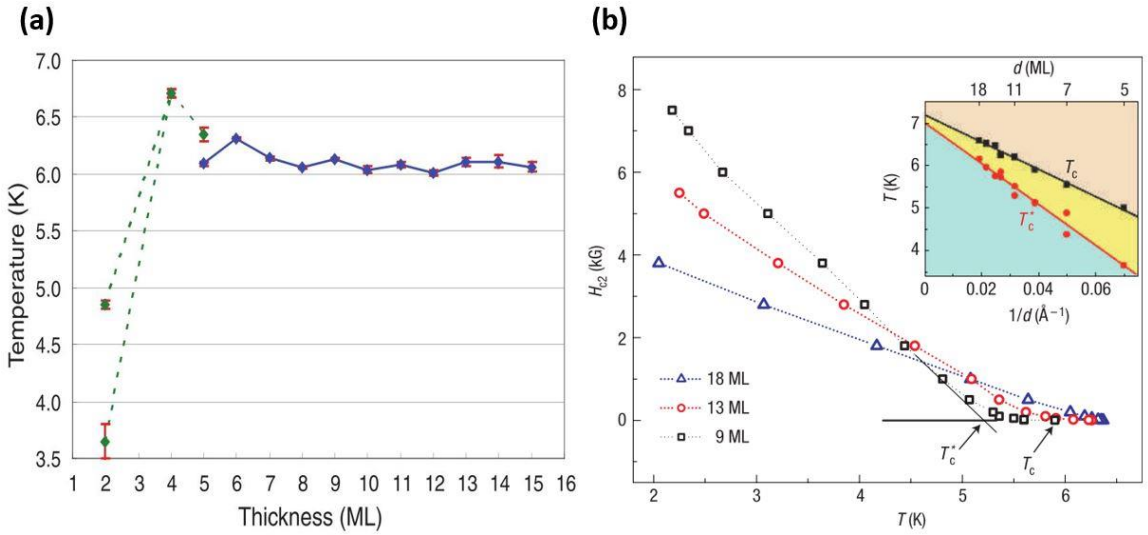

Figure 4.1: (a) Superconducting transition temperature as a function of film thickness, acquired by superconducting gap measurement, at which Cooper pair binding is broken (adopted from ref. [54]). (b) Upper critical fields as a function of temperature for three different thickness Pb films. The insets show two superconducting transition temperatures, T_C and T_C^* as a function of the inverse of the film thickness. At T_C diamagnetic screening starts; whereas, T_C^* is acquired from the extrapolated $H_{C2}(T)$ data (adopted from ref. [42]).

4.1 Superfluid density

4.1.1 Emery-Kivelson criterion

As mentioned in the previous chapter, in conventional superconductor, superconductivity disappears at a critical temperature where the magnitude of order parameter $\Delta(=|\psi|)$ goes to zero and the phase of order parameter θ does not play an important role to determine the critical temperature. In principle, superconductivity can be destroyed by phase fluctuation although Δ is still a finite value. Here, the phase stiffness represents the energy cost to twist the phase,

$$V_0 = \frac{\hbar^2 n_s(0) a}{4m^*}. \tag{4.1}$$

where a is the length scale for phase fluctuation; for the isotropic three dimensional system, a is coherence length ξ, whereas for all quasi-2D materials, a is their thickness d. m* is effective mass. The zero temperature superfluid density is

$$n_s(0) = \frac{m^*}{4\pi}\left(\frac{c}{e\lambda(0)}\right)^2. \tag{4.2}$$

Therefore, the expression of the phase stiffness with measurable quantities is

$$V_0 = \frac{(\hbar c)^2 a}{16\pi e^2 \lambda^2(0)}. \tag{4.3}$$

Since V_0 is in energy scale, it need to convert it to the upper bound of phase ordering temperature T_θ^{max} for convenience like the following

$$T_\theta^{max} = AV_0, \tag{4.4}$$

where A is a dimensionless number; for 3D superconductors, A = 2.2, whereas for 2D, A = 0.9.

V. J. Emery and S. A. Kivelson [65] introduced a useful criterion for the importance of phase fluctuation; if $T_\theta^{max}/T_c \gg 1$, phase fluctuation has minor effect on T_C and T_C is similar to T^{MF}, whereas if $T_\theta^{max}/T_c \sim 1$, there happens apparent difference between Tc and the mean field transition temperature T^{MF} owing to phase fluctuation, and pseudogap feature appears at the middle of the transition, like Figure 4.2.

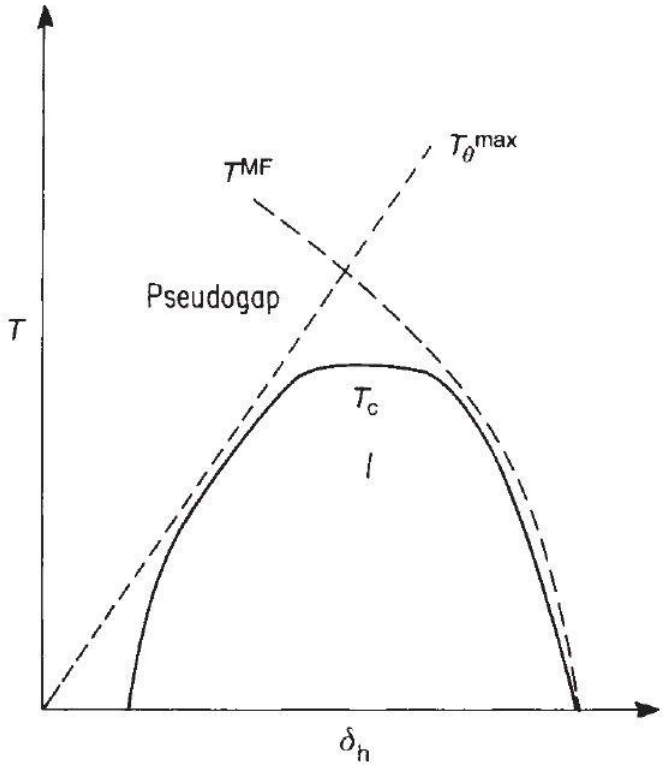

Figure 4.2: The schematic phase diagram of high-temperature superconductors in terms of doping δ_h (adopted from ref. [65]).

4.1.2 BKT transition in 2D xy-model

In 1973, J. M. Kosterlitz and D. J. Thouless interpreted how vortices can give rise to a second order phase transition in the xy-model [67, 68]. The self-energy of an isolated vortex is

$$E_{vortex} = \pi\rho_s ln\left(\frac{R}{a}\right), \tag{4.5}$$

where R is a sample size, a is the lattice size, and ρ_s is the spin-wave stiffness in spin system, corresponding to phase stiffness in superfluid system. Since the vortex should be anywhere in the sample, the entropy is

$$S = \ln\left(\frac{R}{a}\right)^2 = 2\ln\left(\frac{R}{a}\right). \quad (4.6)$$

Therefore, the free energy of the xy-system with a single vortex is

$$F = E - TS = (\pi\rho_s - 2T)\ln\left(\frac{R}{a}\right). \quad (4.7)$$

In the case of $T < \pi\rho_s/2$, F can be minimized with no vortex; whereas, as $T > \pi\rho_s/2$, F can be minimized by increasing the number of vortices and by destroying the quasi long range order. Finally, the system size dependence of free energy gives rise to the phase transition from the ordered to disordered phase at $T_{BKT} = \pi\rho_s/2$, which lead to the system independent universal form,

$$\rho_s/T_{BKT} = 2/\pi. \quad (4.8)$$

The real system with thermally excited vortices is described by the Kosterlitz-Thouless recursion relations,

$$\frac{dK^{-1}}{dl} = 4\pi^3 y^2(l) + O[y^4(l)] \; and \quad (4.9)$$

$$\frac{dy(l)}{dl} = [2 - \pi K(l)]y(l) + O[y^3(l)], \quad (4.10)$$

where reduced stiffness is $K = \rho_s/T$ and vortex fugacity is $y = e^{-E_{core}/T}$ with vortex core energy E_{core}. For temperature near T_C, the solution of the recursion relations is

$$\rho_s^R(T) \approx \rho_s^R(T_C^-)\left[1 + b(T_C - T)^{\frac{1}{2}}\right], \quad (4.11)$$

where b is not a universal coefficient. Figure 4.3 (a) shows the evaluation of equation (4.11) for a series of different T_C. For the experimental example of BKT transition, Figure 4.3 (b) [69, 70] is the period shift ΔP of pure helium 4 for a series of different coverages, using Torsional oscillator techniques. ΔP is proportional to change of superfluid mass. Indeed, superfluid of pure helium 4 undergoes the Kosterlitz-Thouless transition from the superfluid to the normal fluid state.

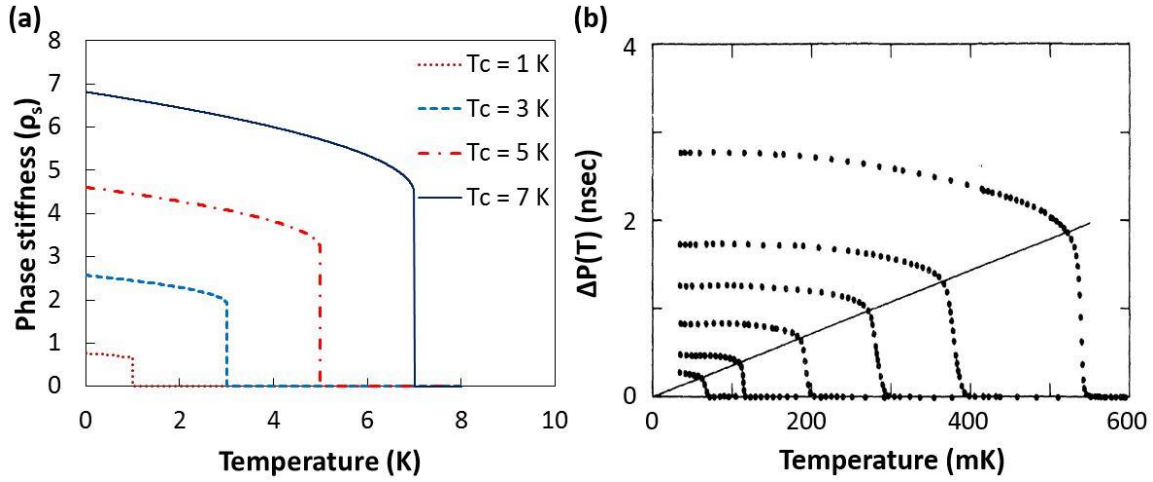

Figure 4.3: (a) Phase stiffness of equation (4.11) as a function of temperature for a series of different T_C. (b) Period shift ΔP(T) for different coverages of pure ^{4}He (adopted from ref. [69]). The solid line is the universal Kosterlitz-Thouless line.

Note that, unlike superfluid of bosonic elements, superfluid of fermionic pairs is somewhat different. As predicted within BCS theory, due to quasi particle excitations at finite temperature, the superfluid density in 2D superconductor undergoes much gradual decrease as temperature increases, except for near T_C.

4.2 Ultrathin global flat Pb film

The ultrathin Pb films are grown using molecular beam epitaxy on highly doped Si (111) substrates. Template surface for global flat thin film growth, is first prepared to create a dense phase of striped incommensurate (SIC) Pb/Si(111) reconstruction, before growth of Pb film [58, 59]. To get SIC surface, ~ 1.5 ML Pb is deposited on Si(111)-7×7 surface at room temperature, followed by annealing the sample at ~ 450 ˚C for 4 min. Figure 4.4 (a) and (b) are the prepared Si(111)-7×7 and SIC reconstruction surfaces, respectively.

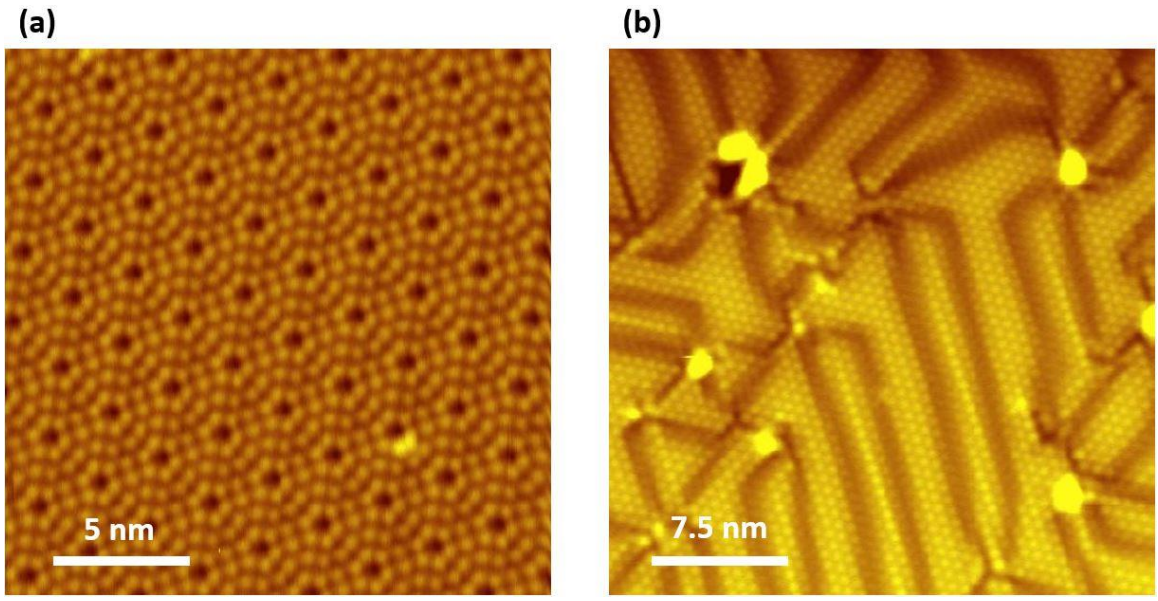

Figure 4.4: (a) Topographic image of Si(111)-7×7 acquired at T = LN_2. (b) Striped incommensurate Pb/Si(111) reconstruction as a template for global flat Pb film growth, acquired at T = LHe.

Global flat Pb films were grown on the template using a two-step process − a low temperature deposition at $T \sim 80$ K and then annealing the sample at room temperature sample garage [60]. Since ultrathin films are sensitive to temperature, the annealing span depends on the film thickness. The film thickness and surface uniformity were always checked quantum well state measurement and topographies at different locations, respectively.

Figure 4.5 (a) and its inset are topographic images of a 5 ML film acquired at two different sample locations that are about 2 mm apart. Figure 4.5 (b) is QWS measurement confirming that 5 ML is the main film thickness. The image in the inset shows triangular pits covering about 1 % of the surface area. These pits are 5 atomic layers deep, exposing very small wetting layer regions. On the other hand, the main STM image acquired at a

location about 2 mm away shows that about 1 % of the surface is covered with additional 2D islands that are 2 ML thick. This result affirms that the film thickness is uniform over a macroscopic length scale with a statistical fluctuation of the film coverage < ± 1 %.

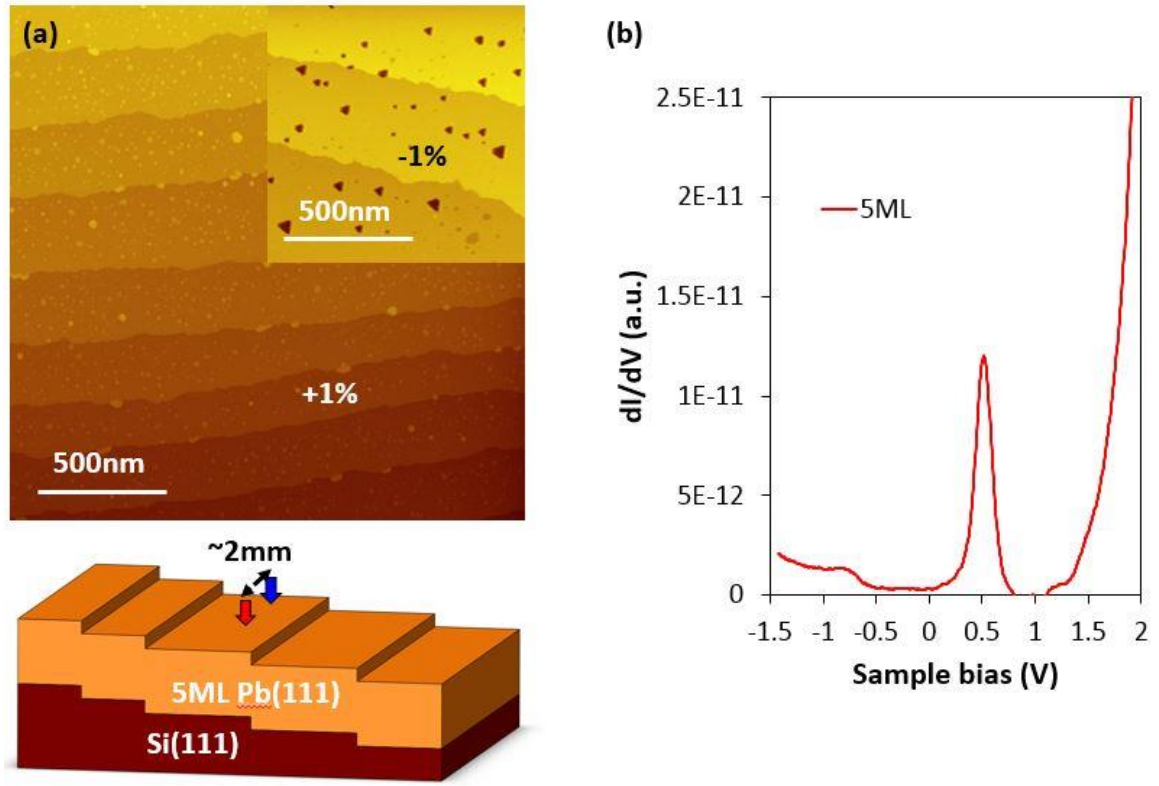

Figure 4.5: (a) Topographic image taken in the middle of the sample, which have additional tiny islands of 2 ML thick. The inset was taken at different location, ~ 2 mm away from the original point. The lower figure is the schematic sample structure and tip locations marked by red and blue arrows. (b) Quantum well state measurement, which confirms the main film thickness of 5 ML Pb film.

4.2.1 Germanium capping for *ex-situ* measurements

Since the macroscopic and mesoscopic measurements were carried out at different facilities, protecting layer had been required to avoid the degradation of superconductor film by not only oxidation but also dewetting in air at room temperature. After finishing *in-situ* STS study, all films were capped with 3 nm of amorphous Ge in the MBE system. While transferring sample from STM to MBE, Pb films were kept at $T \sim 120$ K under UHV of order of 1×10^{-10} torr, using the UHV-LT transfer vessel (in Chapter 2.4.2).

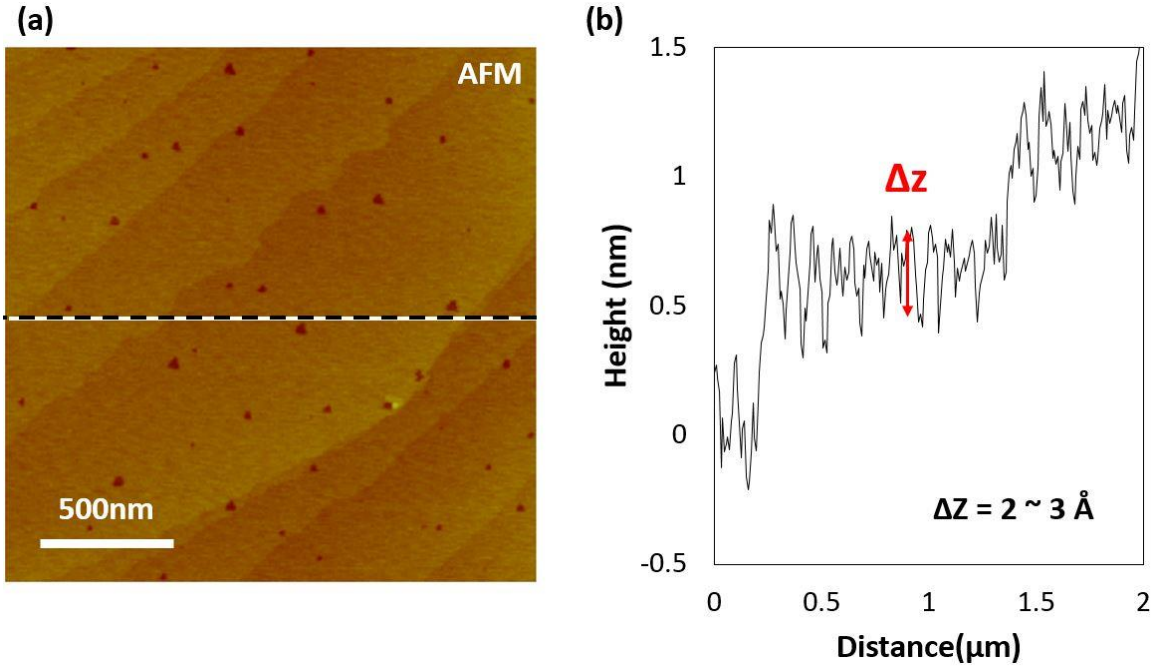

Figure 4.6: (a) Topographic image of 3 nm Ge-capped 5 ML Pb film using AFM. This AFM image was taken in the similar area where the inset of Figure 4.4 (a) had been taken. Both images reveals the same features of pits and smooth surface with clean substrate step edges. (b) The line profile along the dot line in (a), showing apparent terraces. The roughness of amorphous Ge surface is only of 2 Å ~ 3 Å.

In Figure 4.6 (a), atomic force microscope (AFM) image is measured of 3 nm Ge-capped 5 ML Pb film in air at room temperature. The corresponding STM image in a

similar area before capping, is shown as the inset of Figure 4.5 (a). Note that in this region, the coverage is about 1 % deficient as revealed by STM. The same morphology is observed after Ge capping and line profile in Figure 4.6 (b) reveal the roughness of 2 Å ~ 3 Å. Those observations reflect the atomic smoothness of Ge capping film. The quality of Ge capping is extremely important to obtain reliable *ex-situ* superconductivity measurement in practice. Lower quality Ge capping degrades the underlying Pb film so that it gives rise to the suppression of superconductivity; in the worst case, total loss.

4.3 Superconducting phase rigidity

Using the same procedure, Pb films of different thicknesses were prepared for *in-situ* and *ex-situ* measurements. We studied the superconducting phase rigidity in ultrathin global-flat Pb films by comparison with the superconducting transition temperatures acquired at different length scales and in four different methods.

4.3.1 Scanning tunneling spectroscopy

First, STS measurement were performed on *in-situ* Pb films to get one of the critical temperatures, at which Cooper pair binding is broken, by measuring the superconducting gap as a function of temperature. In Figure 4.7 (a), the quasiparticle density of states with sharp coherence peaks can be observed at the spectrum at $T = 2.1$ K. The properties of zero bias conductance and coherence peaks apparently weaken as temperature increases, implying that superconducting gap decreases. The superconducting gap finally disappears at the spectrum of $T = 6.6$ K, although a smooth but weak depression can be seen between ± 10 mV. This type of weak suppression in tunneling spectra persists even at $T >> T_C$, as reported before [61, 62].

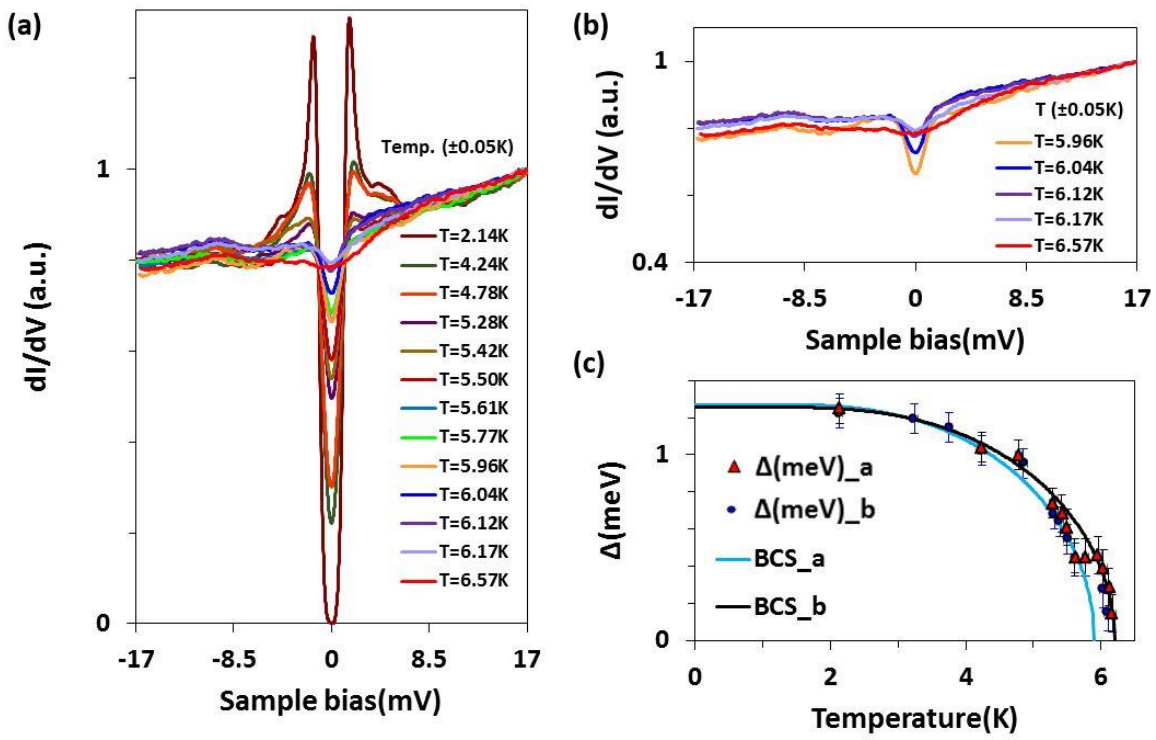

Figure 4.7: (a) *In-situ* STS on 5ML Pb film before Ge-capping at a series of temperatures at the same tip location. (b) For clarity, spectra at $T > 5.8$ K. (c) Superconducting gap as a function of temperature. The red triangles were deduced from BCS quasiparticle density of state fitting to spectra (a). The blue circles are another set of spectra taken with a different tip on the same quality but different 5 ML Pb film to double-check STS measurement. The light blue solid line is BCS fit considering the superconducting gap data points > 0.5 meV, whereas the black solid line for all data points.

Figure 4.7 (c) shows the deduced superconducting gap values Δ with respect to temperature. To double check, two sets of experiments were done with different tips on the same quality but different 5 ML Pb films. Both experiments were self-consist to each other. If we consider data points with $\Delta > 0.5$ meV, the BCS fit deduces the superconducting transition temperature of $T_C = 5.9$ K. A small superconducting gaps, however, still keep going over this temperature. That persistency can directly be seen even in Figure 4.7 (b)

which are spectra taken at $T > 5.8$ K. If we include those data points, BCS fit gives a little higher transition temperature of ~ 6.2 K. Although we can still see the break in the smooth BCS curve around $T = 5.8$ K, except for this feature, superconducting gap is following well the mean field theory [63]. Therefore, it calls this transition temperature T^{MF}.

4.3.2 Double-coil mutual inductance measurement

Double-coil mutual inductance measurement is a nondestructive tool that not only can measure the penetration depth λ of superconductors, but also can acquire absolute value of λ as a function of temperature with no model dependent assumption. Since the relation between superfluid density (SFD) and λ is given by equation 4.2, like $n_s(T) \propto 1/\lambda^2(T)$, it is convenient to call $1/\lambda^2(T)$ superfluid density. The double-coil experiment determines SFD in superconducting films [53]. Figure 4.8 (a) is the schematic diagram of the core part of double-coil mutual inductance measurement set-up. There are two coaxial coils located on the right opposite sides of a superconductor film.

In principle, if temperature is lower than the critical temperature of superconductor films, there appears an induced supercurrent responding to the magnetic field generated by the drive coil. The induced supercurrent both attenuates and shifts the phase of the mutual inductance by an amount measured at receive coil as the complex sheet conductivity of the film, $(\sigma_1 + i\sigma_2)d$, where d is the film thickness; for example, the thickness of 5 ML Pb film is d = 1.43 nm. In fact, the areal density of superconducting carriers $n_s(T)d$ is proportional to $\sigma_2(T)d$, where $1/\lambda^2 \equiv \mu_0\omega\sigma_2$. The frequency of AC current in the drive coil was 50 kHz. Since this frequency is much lower than $2\Delta/\hbar$, of order of THz, our measurement is still in the very low frequency limit. The coil diameters are typically of

millimeter order, so this experiment probes the superconductivity of Pb film at the macro level.

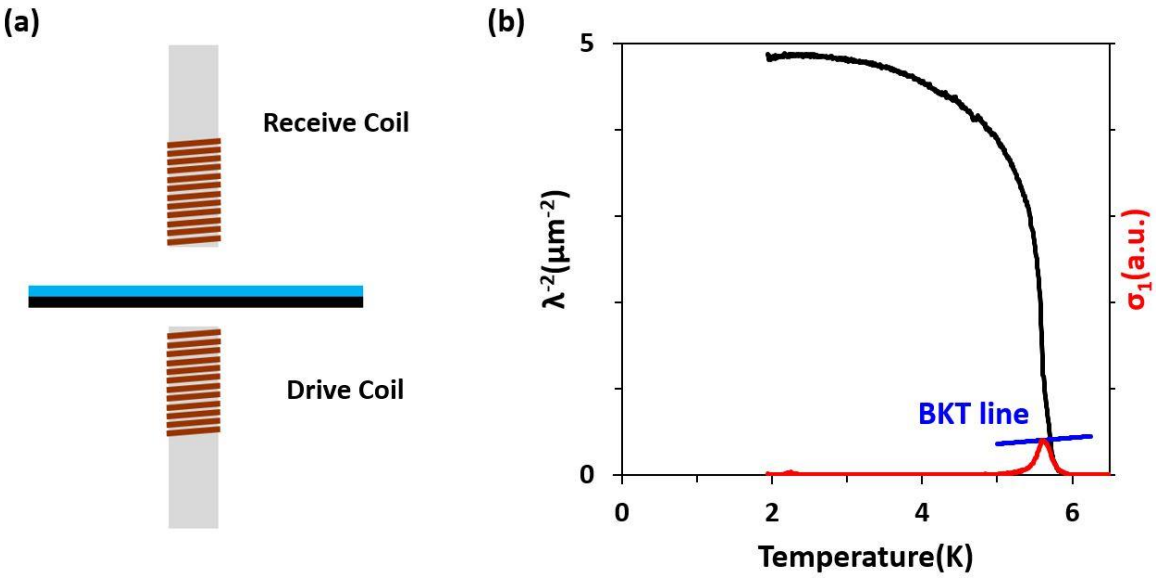

Figure 4.8: (a) Schematics of the core part of double-coil mutual inductance set-up. (b) SFD measured on 3 nm Ge-capped 5 ML Pb film. The blue line is universal BKT transition line, which crosses the SFD curve at T = 5.75 K. (Measured by J. Yong and T. R. Lemberger at OSU)

In Figure 4.8 (b), the temperature dependence of $1/\lambda^2$ show unusual steep drop to zero at T_C, which will be discussed elsewhere. In any case, T_C is at about 5.75 K, whether it is defined from the peak in σ_1 or from the intersection of BKT line $(1/\lambda^2 = 8\pi\mu_0 k_B T/\Phi_0^2 d)$ with SFD curve, where Φ_0 is flux quantum. From this experiment, the macroscopic T_C, where SFD disappears, is similar to T^{MF} determined by STS measurements of superconducting gap at atomic scale. The measured SFD of 5 μm^{-2}, however, is relatively low compared with the bulk SFD of 650 μm^{-2}(deduced by using the penetration depth of bulk Pb of λ = 39 nm).

4.3.3 Scanning-SQUID

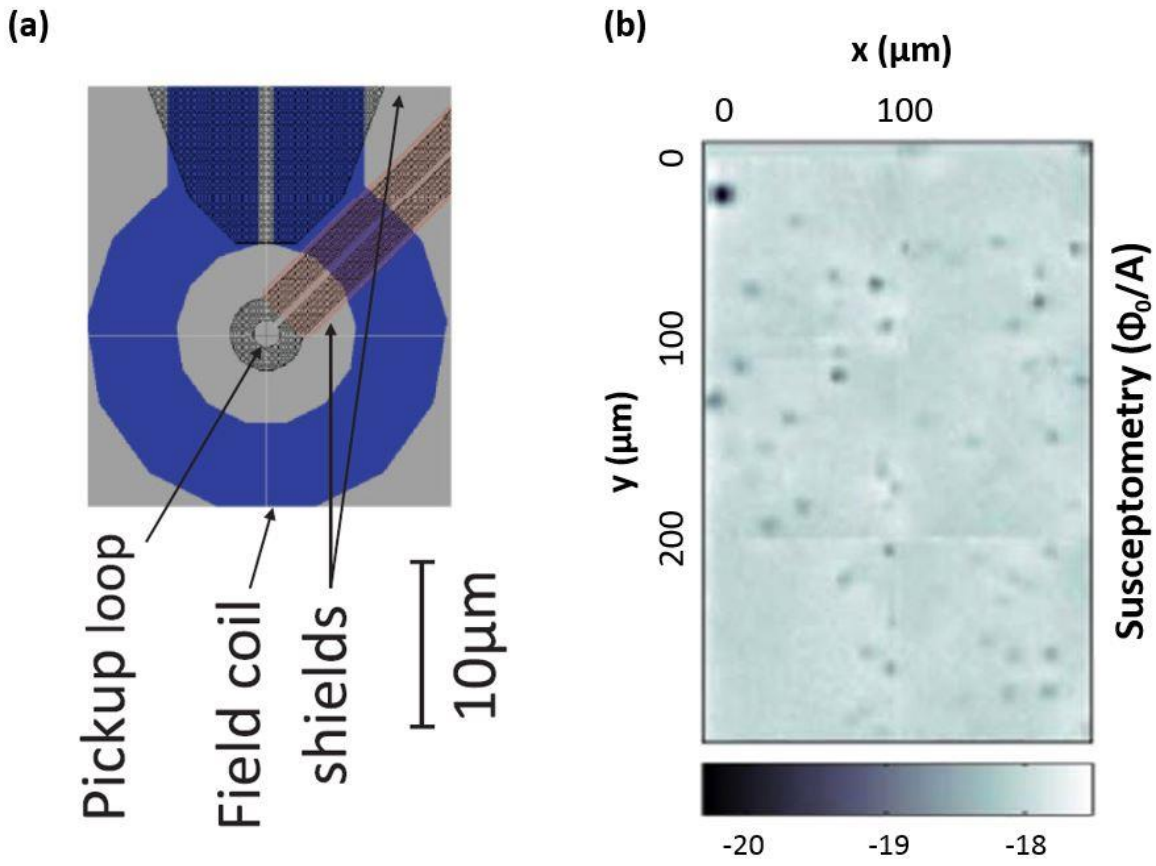

Figure 4.9: (a) The drawing of S-SQUID sensor (adopted from ref. [64]). (b) Susceptometry image taken on the 3 nm Ge-capped 5 ML Pb film cooled at $T = 4.2$ K in a field less than 0.3 μTesla. This mosaic image reflect the spatial uniformity of our superconductor film, except for the black dots. (Measured by P. A. Kratz, J. Kertley, and K. A. Moler at Stanford).

To investigate the superconductivity of 2D Pb films at a mesoscopic length scale, S-SQUID was used to probe our epitaxial 5 ML Pb film with 3 nm Ge capping layer. Figure 4.9 (a) is the drawing of S-SQUID sensor which has a pickup loop of 3 μm in diameter and field coil with the effective radius of a = 8.4 μm [64]. Figure 4.9 (b) is the mosaic images of susceptometry consisting of six images of 100 μm × 100 μm, which phase-sensitively

detected the magnetic flux through the pickup loop due to a 98 μA amplitude AC current flowing through the field coil. The image was acquired at the prove-sample separation of 2 μm at T = 4.2 K. S-SQUID image reflects the spatial uniformity of our sample in terms of the superconductivity respond to magnetic field, except for several black dots. Since the susceptibility at the dots persists at temperature over 7 K, they are most likely local thicker regions where the subtracted step bunching happens. Shown by Figure 4.10 is the AFM image including a step bunching site. The local height is even higher than the highest terrace surface.

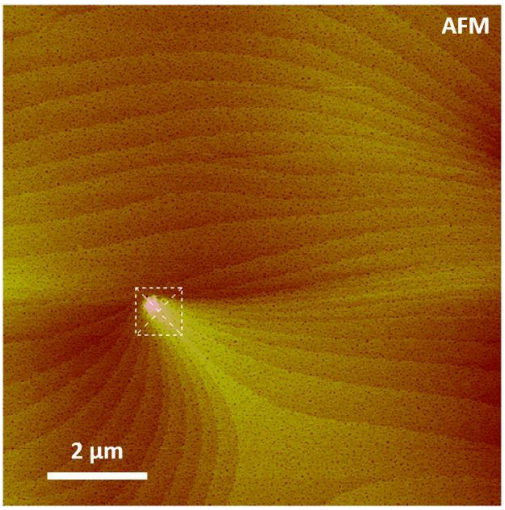

Figure 4.10: AFM images on 3 nm Ge-capped Pb film. It shows a local peak at the step bunching point of silicon substrate. The local height is even higher than the highest terrace surface.

In addition to susceptometry, S-SQUID enables us to determine Pearl length which is another kind of penetration depth and is also directly related to the superfluid density using the double-coil experiment as $\Lambda = 2\lambda^2/d$. Figure 4.11 (a) shows the susceptibility touchdown at T = 4.2 K. The blue dots are experimental data as a function of the sensor

height z above epitaxial 5 ML Pb film and the red solid line is a fit of the SQUID susceptibility expression for a thin diamagnetic film [64],

$$\frac{\phi(z)}{\phi_s} = -\frac{a}{\Lambda}\left(1 - \frac{2\bar{z}}{\sqrt{1+4\bar{z}^2}}\right) \tag{4.12}$$

$$\phi(z) \equiv \frac{\Phi(z)}{I\Phi_0}, \tag{4.13}$$

where $\Phi(z)$ is the magnetic flux through the pickup loop, I is the current through the field coil, and $\Phi_0 = h/2e$ is the superconducting flux quantum, $\bar{z} = z/a$. Here, the Pearl length Λ is used as a fitting parameter. Taking a = 8.4 μm and the sensor self-inductance ϕ_s = 800 A^{-1}, and estimating a minimum height of SQUID sensor $z_0 = 2.5\ \mu m$, the Pear length at T = 4.2 K is of ~ 110 μm. Using the relation between Pear length and the magnetic field penetration depth, the Pearl length of 110 μm for 5ML Pb film corresponds to $1/\lambda^2 = 13\ \mu m^{-2}$ if we assume a uniform film thickness. The results of double-coil and S-SQUID experiments are relatively consistent with each other, within a factor of about three, although the length scales are different by three orders of magnitude.

Figure 4.11 (b) shows the inverse of fitted Pearle length values at different temperatures. The uniform background susceptibility goes to zero as temperature increases over 6 K, except for the black dots as mentioned above. The lower and upper limits of error bars are coming from the sensor heights of 1.5 μm and 3.5 μm, respectively. The temperature dependence of inverse Pearl length reflects that the transition temperature should be in between 5.5 K and 6 K, which is consistent with T_C values determined at the microscopic and macroscopic length scales.

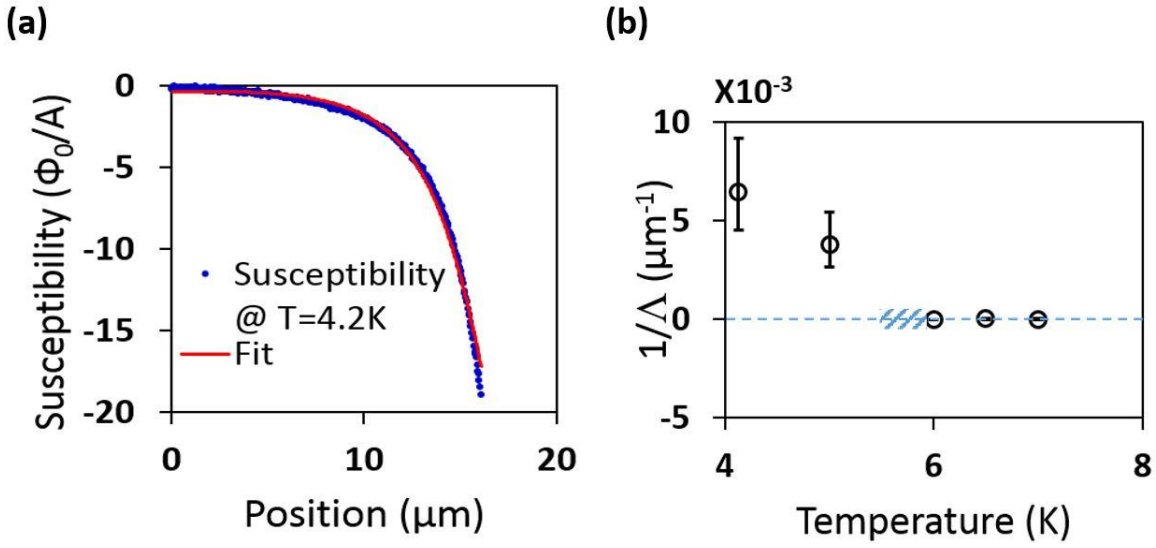

Figure 4.11: (a) SQUID susceptibility measurement as a function of the height of the S-SQUID sensor at T = 4.2 K. The blue dots are experimental data and the red solid line is a fit to an expression for a uniform, thin diamagnetic sample [64]. (b) Inverse Pearl length as a function of temperature. (Measured by P. A. Kratz, J. Kertley, and K. A. Moler at Stanford).

4.3.4 Critical temperature as a function of Pb film thickness

We carried out the superconductivity measurements for not only 5 ML Pb film but also somewhat thicker Pb films. As shown in Figure 4.12, the summary clearly shows the consistent values of T_C although superconductivity proved through dramatically different length scales (from atomic to millimeter scale). Indeed, it proves the superconducting phase rigidity in those ultra-thin superconducting films that are only a few atom thick. However, the measured SFD shows the strong suppression of about two orders of magnitude smaller than the bulk value. It is most surprising that ultrathin Pb films keep their superconducting phase rigidity even under the strong suppression of SFD. Using the Emery-Kivelson criterion in Chapter 4.1.1, this behavior can be explained qualitatively. For 5 ML Pb film, the ratio of T_θ^{max} to T^{MF} is 12, which is still much greater than 1, even with the lowest

value of measured $1/\lambda^2 = 5\,\mu m^{-2}$ from double-coil measurement. This means that the epitaxial Pb film still has strong phase rigidity, and then the superconducting transition temperature should be similar to T^{MF} as we proved.

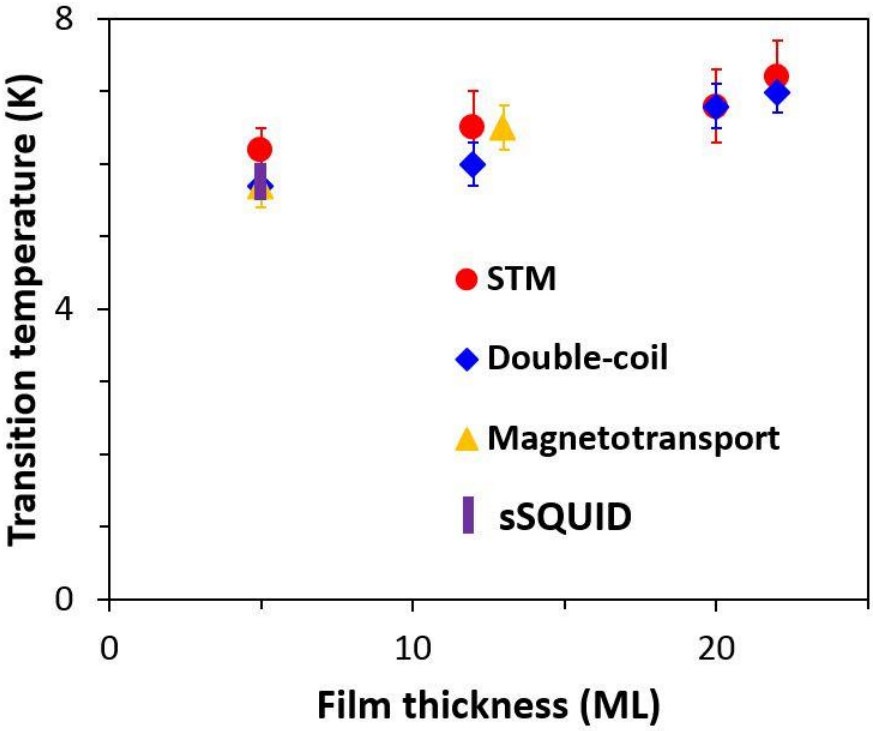

Figure 4.12: Superconducting transition temperatures of epitaxial Pb films of different thicknesses in four different methods at different length scales. For magneto-transport data, we shall see at chapter 4.3.5.

4.3.5 Magneto-transport measurement

Magneto-transport measurement was also performed on Ge-capped Pb films, 5 ML and 13 ML thick. This set-up is able to change the angle of magnetic field with respect to sample surface and to apply the magnetic field strength up to 9 Tesla. Figure 4.13 (a) and (b) are the result of sheet resistance versus temperature ($R_{\square} - T$) under a series of parallel

magnetic fields to the sample surface. First of all, $R_{\square} - T$ data at zero magnetic field shows the apparent superconducting transition at T = 5.7 K for 5 ML Pb film, consistent with double-coil and S-SQUID experiments as seen in Figure 4.12.

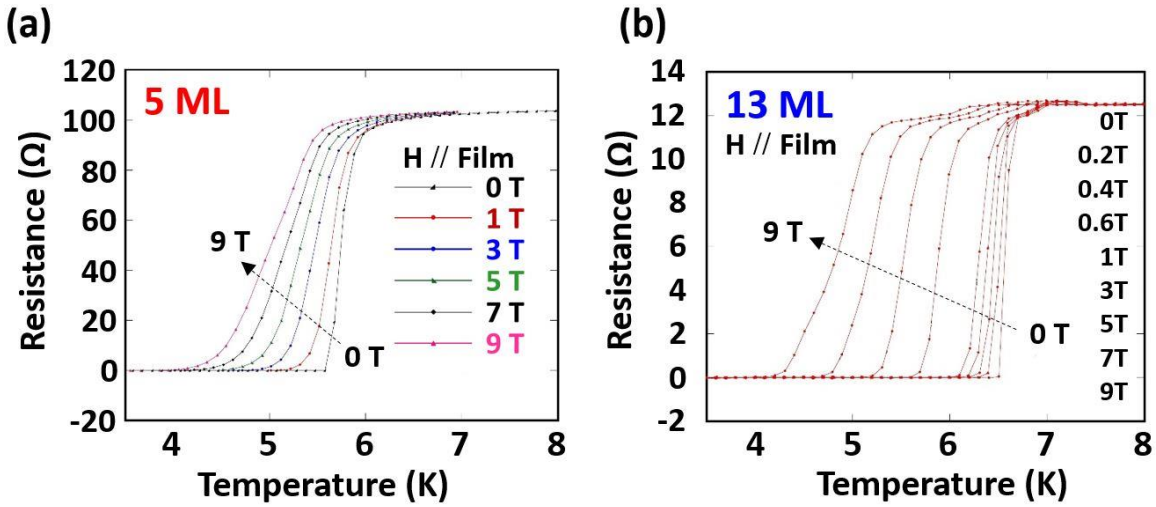

Figure 4.13: Temperature dependence of sheet resistance under the parallel magnetic fields: (a) R-T on 5 ML and (b) on 13 ML Ge-capped Pb films. (Measured by T. J. Liu and P. W. Adams at LSU).

The most remarkable observation is that the superconducting states obviously survive at the maximum available magnetic field of 9 Tesla in the parallel direction to the sample surface; in this configuration, the magnetic field response is mainly due to Zeeman splitting of the conduction electrons, since the orbital coupling to the magnetic field should be suppressed. For example, superconductivity even on 5 ML Pb film at 9 Tesla is clearly observed above T = 4 K as well as 13 ML Pb film.

Another noticeable observation is the apparently low normal-state sheet resistances for both films, whose values are at least one order of magnitude smaller than other's previous studies even on the similarly prepared samples [42, 71]. The normal-state sheet resistances for 5 ML and 13 ML films are 100 Ω and 12 Ω, respectively which is obviously

much smaller than the quantum resistance for electron pairs, $R_Q = h/4e^2$ (~ 6.45 kΩ). Here, the sheet resistance ratio of $R_{\square,5ML}/R_{\square,13ML} = 8.3$ does not meet with the thickness ratio of $d_{13ML}/d_{5ML} = 2.6$, which imply that the resistivity ρ is limited by the surface scattering. Thus, if we reasonably assume the film thicknesses as the mean free paths, it should lead to the resistivity ratio of $\rho_{5ML}/\rho_{13ML} = 2.6$. If we use the definition of sheet resistance, $R_\square = \rho/d$, it would finally induce the expected sheet resistance ratio of $R_{\square,5ML}/R_{\square,13ML} =$ 6.8. The expectation ratio is consistent with the experimental observation.

4.4 Parallel critical field

As shown in Figure 4.14 (a) and (b), angular dependent sheet resistance as a function of the magnitude of magnetic field, $R_\square(|\vec{H}|, \measuredangle\vec{H})$,also carried out at a constant temperature of T = 2 K. The perpendicular critical fields $H_{C,\perp}$ are 1.56 Tesla and 0.63 Tesla for 5 ML and 13 ML films, respectively. According to the Abrikosov-Gorkov theory, the relation between $H_{C,\perp}$ and the carrier diffusion constant D is

$$eDH_{C,\perp}(0) = \frac{\Delta_0}{2}. \tag{4.14}$$

Therefore, the diffusion constant ratio of D_{13ML}/D_{5ML} is about 2.9. It proves again that the normal state carrier conduction in epitaxial ultrathin Pb films is governed by the surface scattering; moreover, it shows the self-consistency between the critical fields and normal state resistances of magneto-resistance experiment.

Figure 4.14 (c) and (d) shows that the angular dependent critical fields increase when the angle of magnetic field becomes lower. Due to the limit of the maximum magnetic field as 9 Tesla, we cannot prove the critical field at angles lower than θ = 6 degree for 5 ML film. For 13 ML film, we can also see that the critical field at θ = 2 degree

really exceeds the measurement limit of 9 Tesla. In addition, in Figure 4.14 (c), the critical field for 5 ML film is 2.8 time higher than that for 13 ML films at all angles.

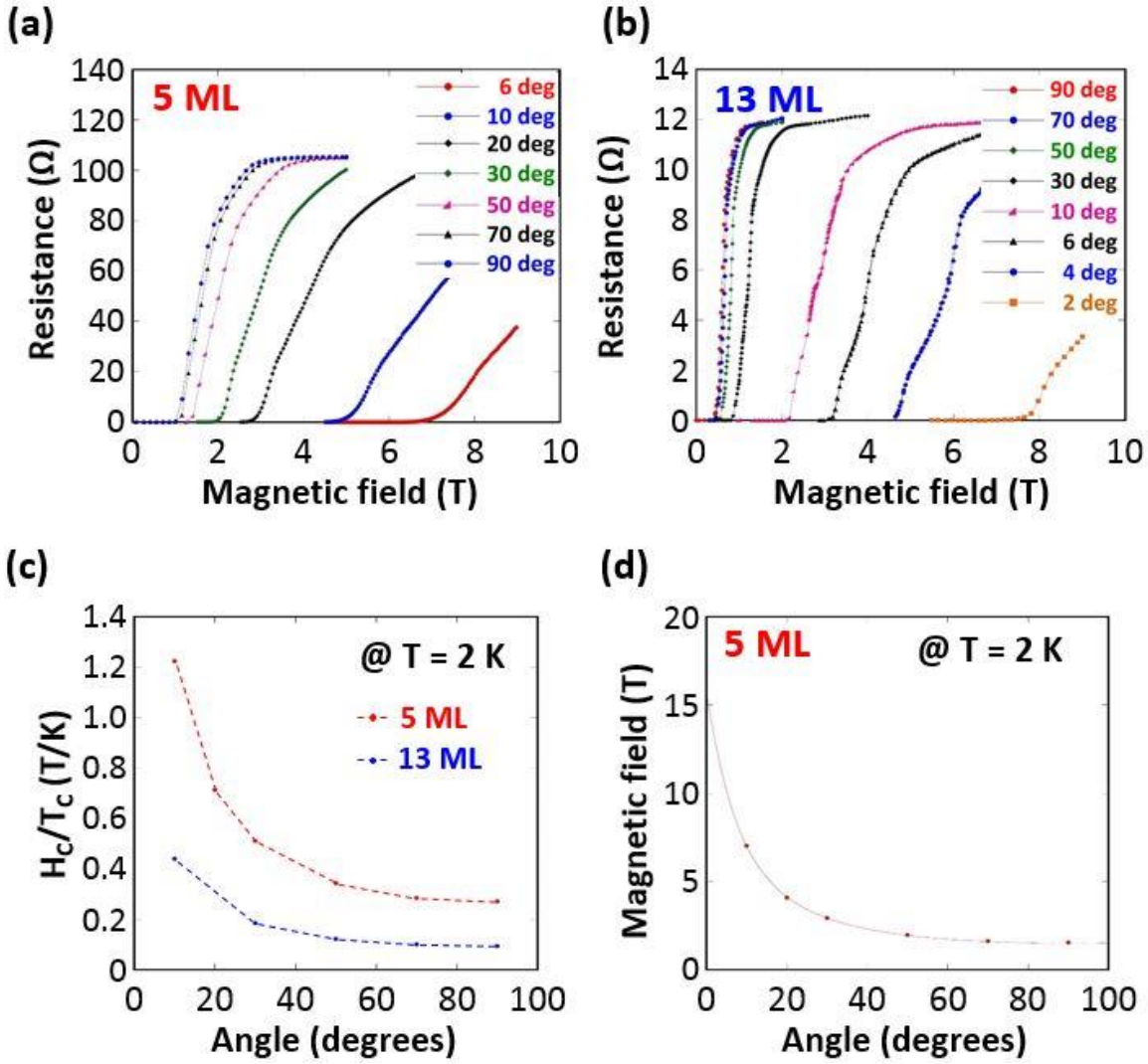

Figure 4.14: $R_{\square}$ as a function of the magnitude of magnetic field at several different angles at T = 2 K. (a) and (b) are for 5 ML and 13 ML Pb films, respectively. (c) Angular dependent critical field, $H_C(\theta)$ normalized to the critical temperature TC. Note that the critical field ratio of $H_{C,5ML}(\theta)/H_{C,13ML}(\theta)$ is 2.8, kept at all angles. Thinkham formula fit to the angular dependent critical field, $H_{C,5ML}(\theta)$ at T = 2 K for 5ML film. The deduced parallel critical field is of 16 Tesla. (Measured by T. J. Liu and P. W. Adams at LSU).

If we neglect spin-orbit scattering, since the parallel magnetic field response is mainly driven by Zeeman splitting, we can consider that the Pauli-limit (Clogston-Chandrasekar) parallel critical field is

$$H_{P,\parallel} = \frac{\Delta}{\sqrt{2}\mu_B}. \tag{4.15}$$

With our experimental data, $\Delta = 1.23\ meV$ for 5 ML film, the Pauli-limit parallel critical field is of ~ 10 Tesla. But with the contribution of spin-orbit scattering, the parallel critical field will increase rather than the Pauli limit because the order-parameter acquires a spin triplet component. Indeed, Figure 4.13 (a) reflects that for 5 ML Pb film, the parallel critical field possibly exceeds the Pauli limit of 10 Tesla. Note that even at 9 Tesla, superconductivity well sustain and T_C is still over 4 K. To estimate a parallel critical field from angular dependent critical field data, we can use Tinkham formula [66],

$$\frac{H_C(\theta)\sin(\theta)}{H_{C,\perp}} + \left(\frac{H_C(\theta)\cos(\theta)}{H_{C,\parallel}}\right)^2 = 1, \tag{4.16}$$

where $H_{C,\perp}$ and $H_{C,\parallel}$ are fitting parameters. $H_{C,\parallel}$ of ~ 16 Tesla was extracted from fit to the experimental data of angular dependent critical fields. Note that with the data at $\theta \geq 10$ deg. Tinkham fit is most likely to underestimate the parallel critical field. In fact, already shown in Figure 3 for Pb film of d ~ 500 Å thickness in Tinkham's original paper [66], the slope of experimental data at low angles are much steeper than that of Tinkham formula. Moreover, for 13 ML film, the critical field at $\theta = 2$ deg. already exceeds 9 Tesla. If we consider the factor of 2.8 between angular dependent critical fields for 5 ML and 13 ML films, $H_{C,5ML}(2^\circ)$ should be over 25 Tesla for 5 ML films. It means that the parallel critical field $H_{C,5ML}(0^\circ)$ is possibly even higher than the expected value at $\theta = 2$ deg., which would be arisen from the consequence of the strong spin-orbit coupling of Pb [72, 73].

4.5 Summary

We were able to epitaxially grow globally flat and ultrathin Pb films. For *ex-situ* measurement, we could successfully cap the epitaxial Pb films with 3 nm amorphous Ge layer which only protects the films without disrupting the underlying Pb films. One of the most intriguing observations is the consistency of superconducting transition temperatures at all length scales. This result attests the robust superfluid rigidity in ultrathin Pb films. The superfluid density analysis confirms that the phase stiffness is still remarkably strong even in 1.43 nm thickness Pb film. The most noticeable observation is that the superconductivity sustains in Zeeman fields, much greater than Pauli limit.

Chapter 5: STM/S studies of three dimensional intrinsic topological insulator $Bi_{2-x}Sb_xTe_{3-y}Se_y$

Three dimensional topological insulators (3D-TI) have been attracting a lot of interest in spin chiral topological surface states (TSS) [74-84]. One of the major material challenges has been the difficulty to create a topological insulator with true insulating bulk so that TSSs become the main channel of transport properties [85-88]. There has been effort in creating the ternary/quaternary compounds, $Bi_{2-x}Sb_xTe_{3-y}Se_y$ (BSTS) with intrinsic bulk states [79, 82, 83, 89]. Namely the Fermi level is inside the bulk band gap with Dirac point (DP) also in the bulk band gap. Angle resolved photoemission spectroscopy (ARPES) has been used to show that BSTSs possess this desirable property. Fourier transform scanning tunneling spectroscopy (FT-STS) was carried out to show electron backscattering protection in the wide range angle, arising from spin chiral TSS in $Bi_{1.5}Sb_{0.5}Te_{1.7}Se_{1.3}$ [90]. Moreover, recent observation of TSS quantum Hall effect (QHE) in BSTS, marks another important milestone, demonstrating the $Bi_1Sb_1Te_1Se_2$ exhibits surface dominated conduction up to room temperature and a surface Dirac Fermion QHE until $T = 35$ K [91].

Using scanning tunneling microscopy and spectroscopy (STM/S), we studied the structure and stability of single crystal $Bi_2Te_2S_1$ and $Bi_1Sb_1Te_1Se_2$ samples. All BSTS samples were grown by the vertical Bridgeman technique. According to the analysis of bias dependent STM, the structures of BSTS samples were uncovered compared with X-ray diffraction (XRD) analysis. In terms of electronic structure, with the second derivative of tunneling current, we accurately observed the locations of valence band maximum point and conduction band minimum point as well as DP, which is consistent with previous ARPES studies. Using this method, we can discuss the spatial correlation of DP fluctuation with respect to the local compositional fluctuation due to random alloy. The most intriguing

observation is that DP tends to self-align around Fermi level in $Bi_1Sb_1Te_1Se_2$ despite the nature of random alloy.

5.1 Introduction

5.1.1 Three dimensional topological insulator

$Bi_{1-x}Sb_x$ is the 3D-TI that was first experimentally discovered using ARPES [74], shown in Figure 5.1 (a). However, it has some issues associated with the small band gap of less than 50 meV and alloying disorder as well as five surface bands. Those issues make it hard to utilize topological insulator phase, especially due to the small band gap and the complex surface feature.

After $Bi_{1-x}Sb_x$ alloy, Y. Xia et al [84] reported the observation of new generation 3D-TI, Bi_2Se_3 with a single Dirac cone on the surface, induced by the strong spin-orbit coupling. Figure 5.1 (b) shows that ARPES clearly revealed the single Dirac cone in Bi_2Se_3 band gap. Its structure is stoichiometric with quintuple layers (QL) [like Figure 5.1 (c)] rather than a random alloy. The noticeable part at the application point of view is that Bi_2Se_3 has a large band gap of ~ 0.3 eV. This value indicates that Bi_2Se_3 behaves as topological insulator at room temperature. But, due to atomic vacancies or excess selenium, Bi_2Se_3 has strong tendency to be n-type; namely, Fermi level is inside the bulk conduction band, as shown in Figure 5.1 (b) and (d). Since both phases of quantum spin Hall insulator and the strong topological insulator are expected in the vicinity of Dirac point, if Fermi level is inside the bulk conduction band, bulk carrier behaviors would fully bury the novel topological surface properties. To get the Fermi level within band gap, additional works are required, such as electrical or chemical gating methods [87, 88].

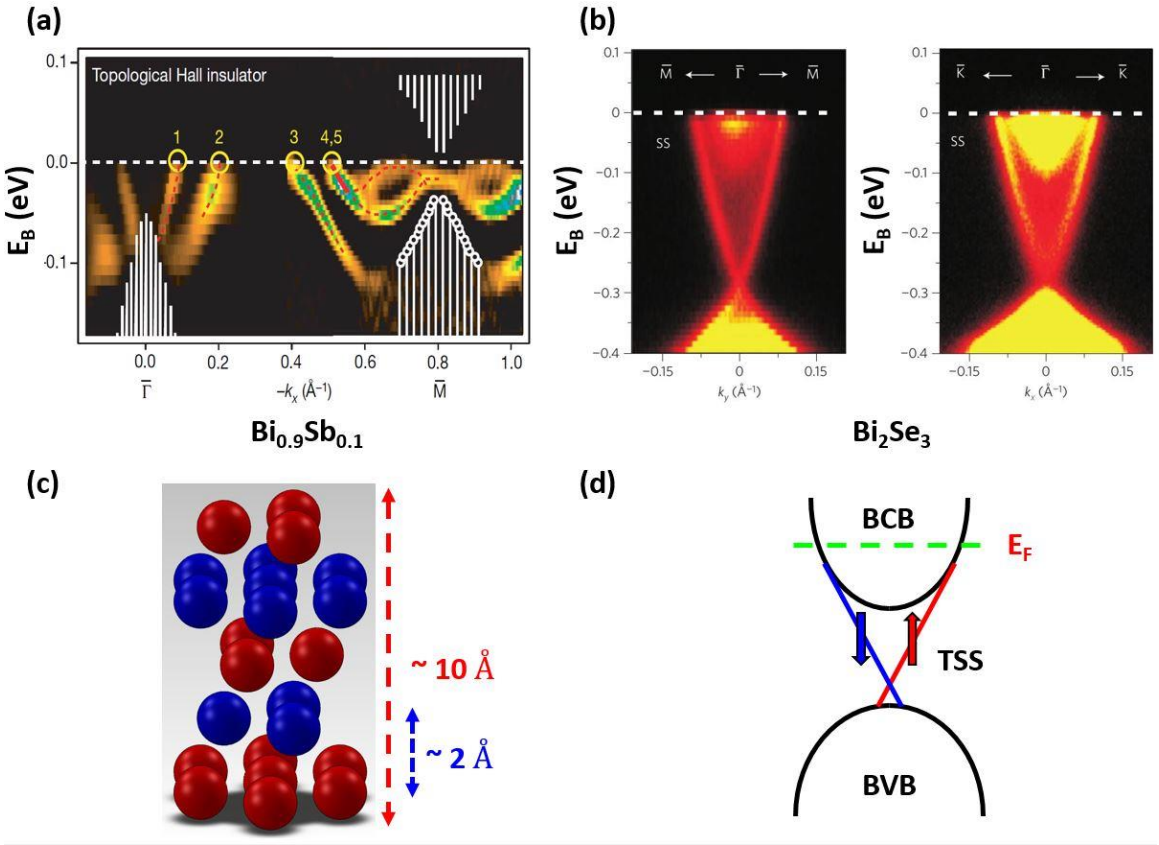

Figure 5.1: (a) ARPES data of $Bi_{0.9}Sb_{0.1}$ with five surface states, crossing Fermi level, in the band gap of less than 50 meV (adopted from ref. [74]). (b) ARPES measurements on Bi_2Se_3 revealing one Dirac cone in bulk band gap of about 0.3 eV (adopted from ref. [84]). Note that Fermi level is inside the bulk conduction band. Schematics of quintuple layer (c) and band structure (d) of Bi_2Se_3 class. Red and blue spheres represent Se (or Te) and Bi (or Sb) atoms, respectively. The thickness of one quintuple layer is about 10 Å and the nearest layers distance is of ~ 2 Å.

In addition, Bi_2Se_3 are not free from aging effect under which the electronic structure of TSS undergoes the apparent change as a function of time [85-88, 92]. Shown in Figure 5.2 is that the aging effect continuously happens after cleaving Bi_2Se_3 surface and leads to not only the shift of Fermi level towards the deep inside of the bulk conduction band, but also the change in bulk band structures, such as Rashiba splitting. Aging effect

is another issue which prevents making use of the exotic states of TI in science and application.

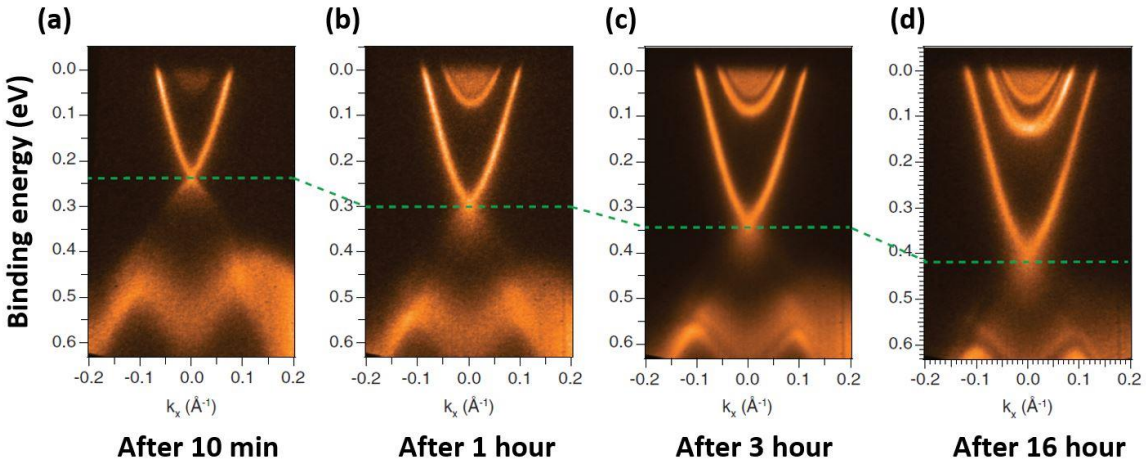

Figure 5.2: ARPES measurements of Bi_2Se_3 at different times after cleaving the surface (adopted from ref. [92]). Note that, as time passes after cleaving the sample surface, Fermi level clearly move towards the deep inside of conduction band as well as Rashiba splitting in bulk band structures.

5.1.2 Previous APRES studies for BSTS

Recently ARPES studies carried out four selective composition ratios of BSTS compounds [89], like Figure 5.3 (a), which are expected to be suitable for reducing defect formations due to chemical characteristics. ARPES data showed that BSTS compounds have Fermi level within bulk band gap, as well as a single Dirac cone. Despite the complex constituent elements, linear dispersion features are well developed for all four samples. Moreover, DP relative location within bulk band gap can be tuned by changing the composition ratio, which can determine the type of Dirac carriers. Note that, as shown in Figure 5.3 (b), the change of DP location is stronger than that of energy gap as the

composition ratio is tuned. This fact implies that the variation of local composition could be reflected on the spatial distribution of DP.

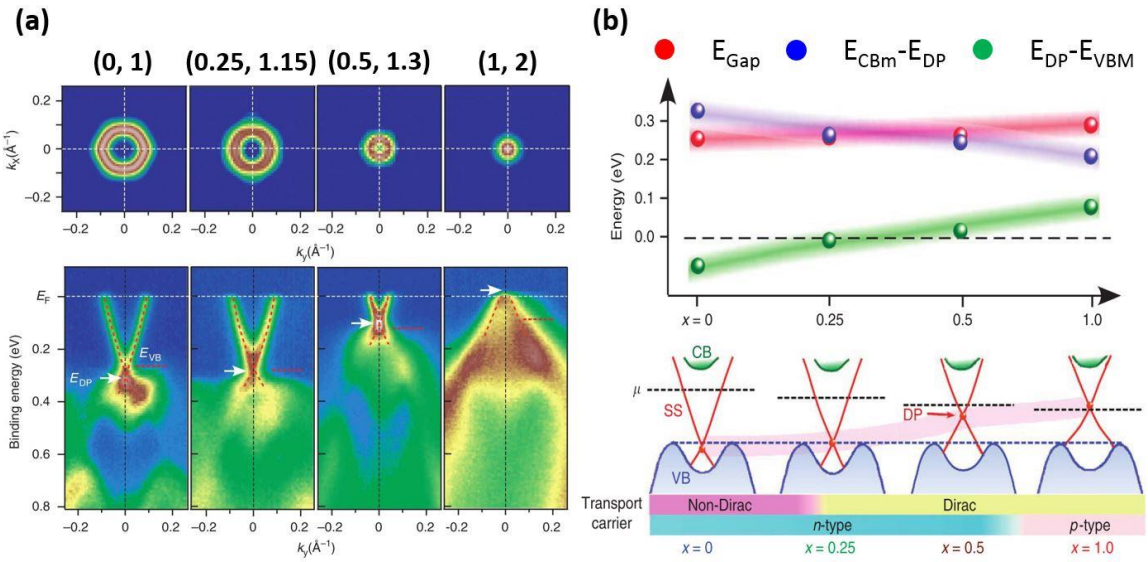

Figure 5.3: (a) APRES data of $Bi_{2-x}Sb_xTe_{3-y}Se_y$ with for different composition ratios (x, y) (adopted from ref. [89]). All four samples show Fermi level within bulk band gap with a single Dirac cone feature. (b) The schematic band diagram and the values of characteristic energies (adopted from ref. [89]). The red symbols are bulk band gap. The blue and green symbols indicate energy differences between DP and either the conduction bend minimum (CBm) or the valence band maximum (VBM), respectively.

Indeed, some of the exotic behaviors in 3D-TI were observed, based on the surface-dominated conduction of BSTS TI. For instance, the robust protection of Dirac carriers from backscattering, due to spin-polarized single Dirac cone on the surface, was revealed by the comparison between the quasiparticle interference measurement and ARPES [in Figure 5.4 (a)] [90]. The critical scattering vector is 75 % of the corresponding TSS diameter, which means that scattering is prevented in the wide range of angle, 100˚ - 180˚. Another remarkable observation was reported by Y. Xu *et al.* that BSTS exhibits the

surface dominated conduction till room temperature and topological surface state spin QHE at temperature as high as $T = 35$ K [in Figure 5.4 (b)] [91].

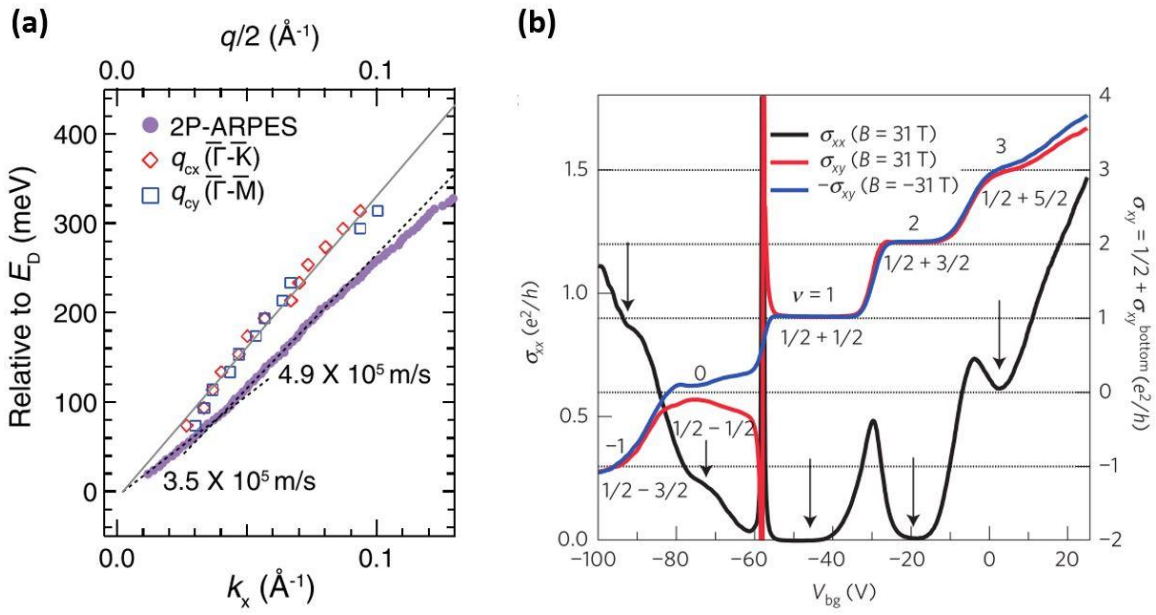

Figure 5.4: (a) The critical scattering vector lengths q_{cx} and q_{cy} from FT-STS measurements and the diameter of constant energy contour of TSS from ARPES. Here, the critical scattering vector length is about 75 % of the corresponding TSS diameter (adopted from ref. [90]). (b) Gate-tuned quantum Hall effect in BSTS, clearly showing the behavior of a surface Dirac fermion QHE in the magnetic field of B = 31 Tesla (adopted from ref. [91]).

On the other hand, there were some reports associated with aging effect even in BSTS, such as $Bi_2Te_2Se_1$ and $Bi_{1.5}Sb_{0.5}Te_{1.7}Se_{1.3}$ [89, 90, 93, 94]. However, we will show the interesting observation that $Bi_1Sb_1Te_1Se_2$ is remarkably stable against aging effect in contrast to other BSTS compositions.

5.2 Order or random alloys

Unlike binary compound TIs, stoichiometric alloys, there are various possible combinations of constituent elements in quintuple layer for ternary/quaternary compounds. One reasonable combination is that a compound tends to be an alloy with the ordering of either pnictogens (Bi or Sb) or chalcogens (Te or Se), whereas another is to be completely random alloys in both pnictogen and chalcogen layers. Using scanning tunneling microscopy, the microscopic analysis of $Bi_2Te_2Se_1$ and $Bi_1Sb_1Te_1Se_2$, here, revealed that their structures are order and random alloys, respectively, consistent with the macroscopic measurement results of XRD data on samples from the same batch of BSTSs.

5.2.1 Ordered arrangement of Bi_2Te_2Se with slight random arrangement

STM topographic image of Figure 5.5 acquired on our $Bi_2Te_2Se_1$, shows a clean atomic image with binary contrast. Even at dark lattice points, complete appearance of atoms are shown up, instead of parts of three atoms like Figure 5.5 (d). In addition, the line profile, along the white dash line on Figure 5.5 (a), reveals that all registered atoms shows up at the exact lattice points with even heights in both bright and dark regions. The height difference of only 60 pm is too small compared with the nearest layer distance within a quintuple layer of ~ 2 Å. Therefore, the dark spots are still one of chalcogen atoms. The binary contrast behavior most likely reflects different chalcogen atoms on the homogenous underlying Bi layer. The dark atoms are possibly Se atoms due to smaller atom size and more preferable Se-Bi bonding [94]. Moreover, since Te ratio is larger than Se ratio for $Bi_2Te_2Se_1$, it is reasonable to assign the bright atoms in topography as Te, whereas Se for dark atoms. When we count the number of each kind of atoms, the occupations are 85% for Te and 15 % for Se, respectively. The numbers are much different from 67 % and 33

%, deduced from the fact that the total ratio of Te to Se is 2:1. This reflects the ordered feature of $Bi_2Te_2Se_1$ rather than a random configuration.

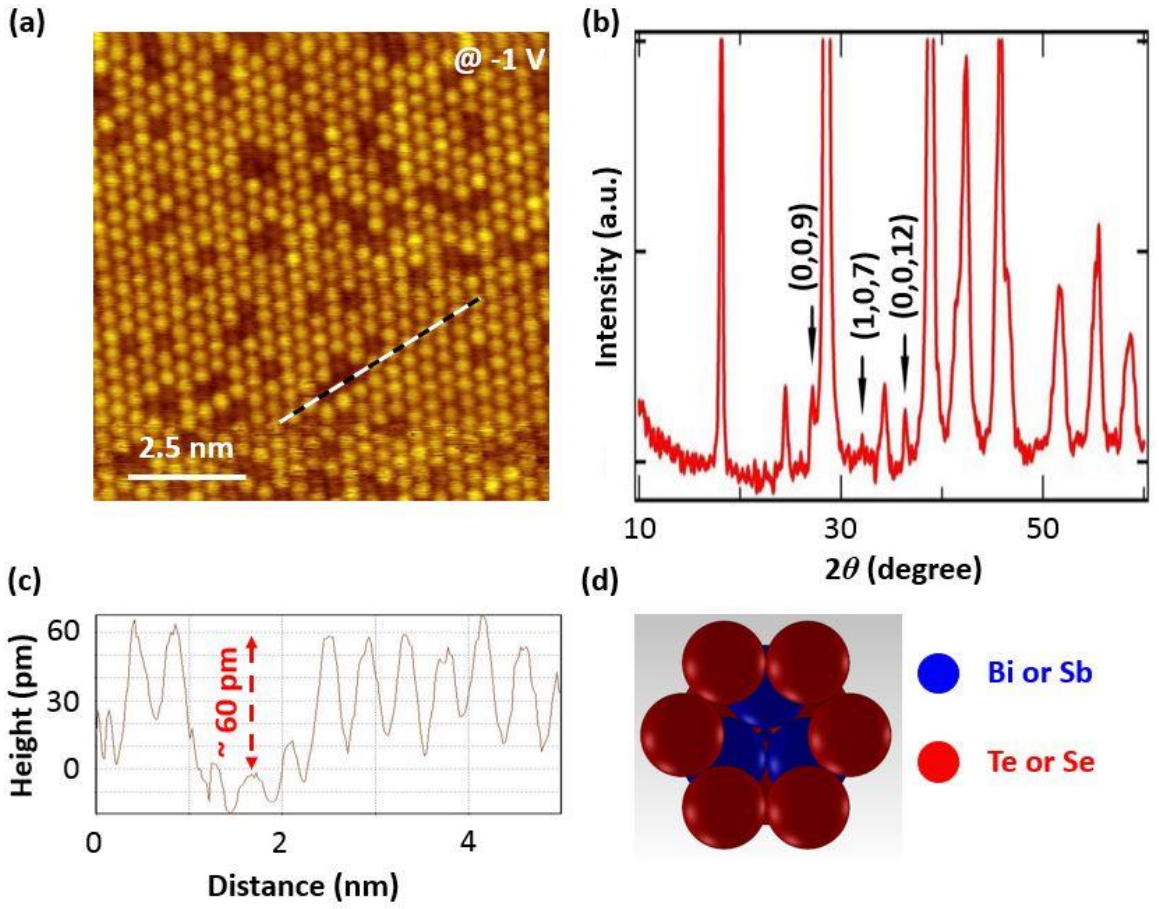

Figure 5.5: (a) Topographic image of $Bi_2Te_2Se_1$ acquired at V_{sample} = -1 V and at T = 77 K. The ratio of bright to dark lattice points is 85 % : 15 %. (b) X-ray powder-diffraction patterns of the same batch of $Bi_2Te_2Se_1$ (adopted from ref. [93]). The three characteristic peaks are marked by (0,0,9), (1,0,7), and (0,0,12). (c) Line profile along the white dash line in (a), showing apparent atomic alignment with even height and 60 pm height difference between bright and dark spots. (d) Schematic top view around the lattice point where one atom in top chalcogen layer is missed. Bi atoms in underlying are not registered right under the center of lattice points of top layer.

In fact, as previous XRD study for $Bi_2Te_2Se_1$ compound [93-95], our XRD spectrum in Figure 5.5 (b) also shows consistent features with the three characteristic peaks, marked by (0,0,9), (1,0,7), and (0,0,12) [93]. Those peaks implied the ordered arrangement of $Bi_2Te_2Se_1$, like the quintuple layer of Te-*Bi*-Se-*Bi*-Te. Within this ordered arrangement, the formation of Se vacancies would be well suppressed due to the strong chemical bonding with Bi atoms. It finally leads to achieve the bulk insulating topological surface state behaviors in $Bi_2Te_2Se_1$.

Using STM and XRD, both microscopic and macroscopic observations showed the consistent result that the $Bi_2Te_2Se_1$ is an order alloy, although there is a slight randomness of 15 % of top chalcogen layer. The quintuple layer is close to Te-*Bi*-Se-*Bi*-Te, rather than the random configuration such as $(Te_2/Se_1)_{1/3}$-*Bi*-$(Te_2/Se_1)_{1/3}$-*Bi*-$(Te_2/Se_1)_{1/3}$.

5.2.2 Random arrangement of $BiSbTeSe_2$

For $Bi_1Sb_1Te_1Se_2$, the topographic image in Figure 5.6 (a) is so complicated that it would be ascribed to the random arrangement in not only the pnictogen layer but also the chalcogen layer. As shown in Figure 5.6 (c), the line profile clearly shows apparent contrast to figure 5.5 (c). There are diverse height atoms instead of even height feature. However, all atoms are still registered at the center of top layer lattice points. In addition, since the height difference is only 35 pm, the dark atoms cannot be atoms in the underlying layer. The complicated contrast should be not due to missing atoms but the random variation of local composition in both kind layers in each quintuple layer. Moreover, if the quintuple layer of $Bi_1Sb_1Te_1Se_2$ has an ordering configuration, such as Se-*(Bi/Sb)*$_{1/2}$-Te-*(Bi/Sb)*$_{1/2}$-Se, STM image should be similar to Figure 5.5 (a) with the binary contrast because of the

homogenous chalcogen layers at this time. Therefore, the quintuple layer of $Bi_1Sb_1Te_1Se_2$ is a random structure like $(Te/Se_2)_{1/3}$-*(Bi/Sb)*$_{1/2}$-$(Te/Se_2)_{1/3}$-*(Bi/Sb)*$_{1/2}$-$(Te/Se_2)_{1/3}$.

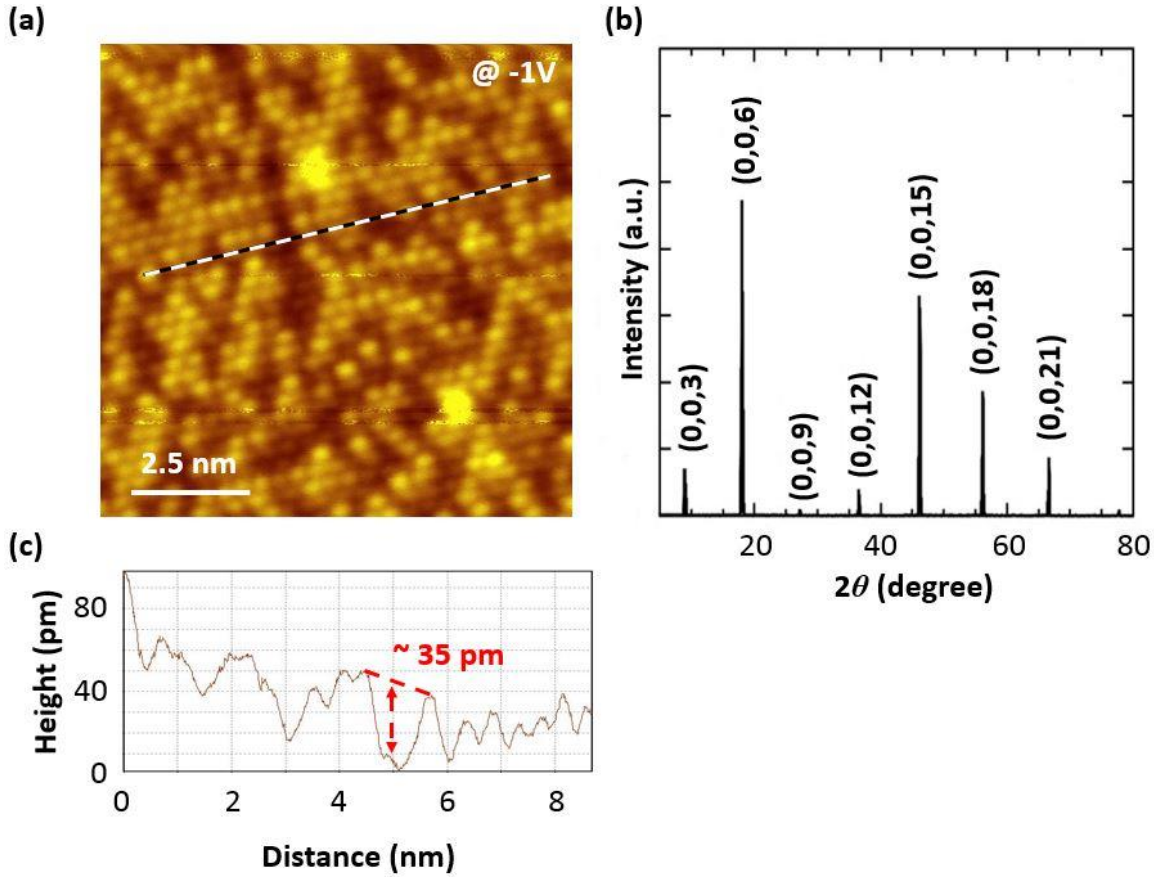

Figure 5.6: (a) Topographic image of $Bi_1Sb_1Te_1Se_2$ taken at V_{sample} = -1 V and at T = 77 K, showing much more complicated contrast than that of $Bi_2Te_2Se_1$. (b) XRD spectrum measured from a bulk crystal. It does not indicate ordering features, but shows high quality of the single crystal with the large peak of (0,0,6) (adopted from ref. [91]). (c) Line profile along the white dash line in (a). The height difference between deep site atom and neighbor bright atom is only 35 pm.

Figure 5.6 (b) shows XRD measured from the bulk single crystal [91]. Although the spectrum indicates the high quality of our single crystal with the strong peak of (0,0,6), it reflects no ordering feature, which is consistent with STM analysis of $Bi_1Sb_1Te_1Se_2$. The

bias dependence of STM images gives more convincing evidence for both TI structures. For $Bi_2Te_2Se_1$, STM images shows direct correlation with respect to the sign of sample bias like Figure 5.7 (a) and (b). As mentioned before, the STM image contrast is indeed independent of bias polarity because it is related only to chalcogen layer atom variation on the homogeneous Bi-layer. As shown in figure 5.8, the simulation for the most top two layers reveals the height difference between Te and Se atoms is about 52 pm, using atomic radii of atoms: 1.5 Å for Bi, 1.42 Å for Te, and 1.19 Å for Se. Compared with 60 pm from STM line profile in figure 5.6 (c), it proves that major factor of STM contrast in $Bi_2Te_2Se_1$, indeed comes from chalcogen atom size difference father than local electron density.

In contrast, for $Bi_1Sb_1Te_1Se_2$, both chalcogen and pnictogen layers have random alloying behaviors, which leads to complicate local composition variation as well. Both factors of atom size difference and local electron density of states most likely contribute to the final random contrast feature at STM image. Figure 5.7 (c) and (d) shows neither direct correlation nor anti-correlation behavior in $Bi_1Sb_1Te_1Se_2$ to the bias polarity change. There are four circles on both images for easy comparison. Note that the complexity of composition does not mean breaking crystallite. At XRD spectra and STM images, we can still see the high quality of sample crystallite.

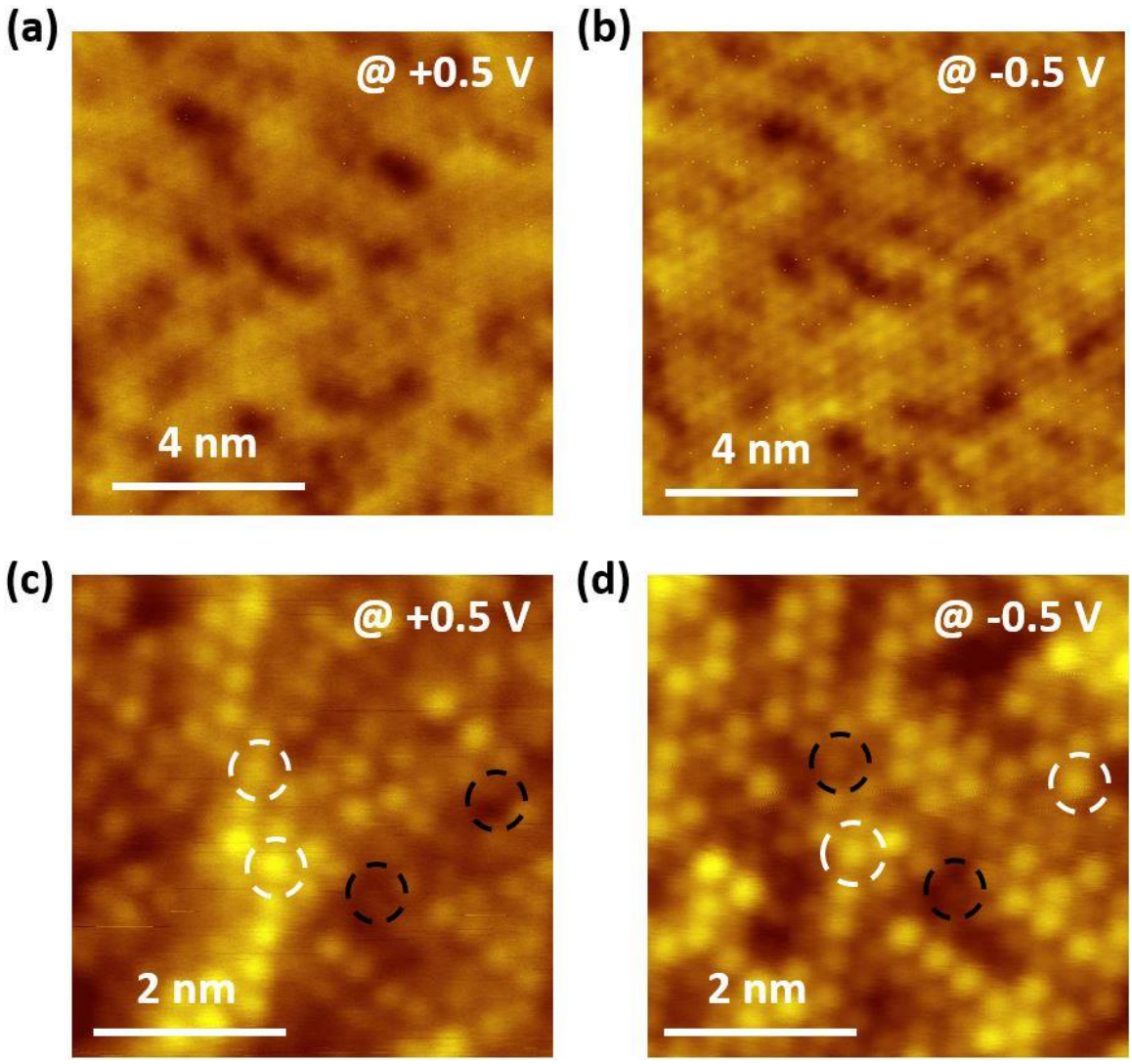

Figure 5.7: Polarity dependence of topographic images: (a) and (b) on $Bi_2Te_2Se_1$, (c) and (d) on $Bi_1Sb_1Te_1Se_2$. Four representative atoms are marked by circles on the both images of (c) and (d). This comparison reveals that the contrast change has neither simple correlation nor anti-correlation with respect to bias polarity.

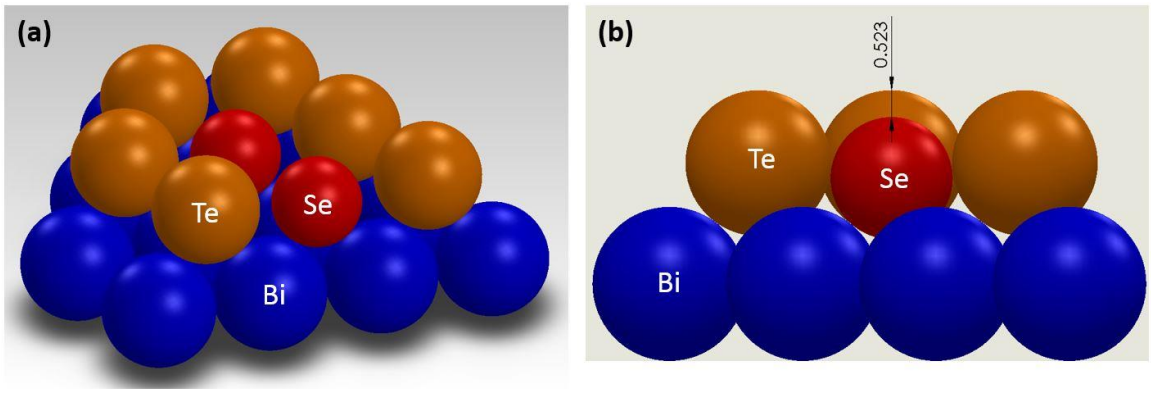

Figure 5.8: (a) Schematics of the most top two layers of Bi_2Te_2Se on vacuum side, using atomic radii: 1.5 Å for Bi, 1.42 Å for Te, and 1.19 Å for Se. (b) Lateral view shows the height difference of 0.523 Å, consistent with STM line profile.

5.3 Self-alignment of Dirac point in $BiSbTeSe_2$

In the previous section, we saw that $Bi_1Sb_1Te_1Se_2$ structure is a random alloy. Despite spatial fluctuation of composition, we observed that DP tends to align together by themselves, especially around Fermi level. Here, we adopted the second derivative spectroscopy for apparent discussion about energy levels.

5.3.1 The second derivative spectroscopy.

As discussed about the random arrangement of $Bi_1Sb_1Te_1Se_2$, there must be local composition variation. As shown in Figure 5.3 (b), the composition variation gives rise to strong change of DP location in bulk band gap, whereas the band gap is of slight change. Therefore, the random alloy feature would be reflected on the spatial fluctuation of DP. In order to examine the electronic structure of TI, we carried out the second derivative spectroscopy on the surface of $Bi_1Sb_1Te_1Se_2$. The red curves in Figure 5.9 (a) and (b) are differential conductivity of tunneling current from experimental measurement and its

simulation, respectively. On experimental dI/dV spectrum acquired at T = 77 K, one can recognize the characteristic surface features of an intrinsic topological insulator; for example, linear TSS dispersion within bulk band gap and DP coincided with Fermi level. It is, however, not easy to accurately identify the energy locations with respect to Fermi level, especially CBm and VBM owing to the thermally smoothed dispersion curves.

To accurately determine the energy locations, we took the derivative to the dI/dV spectrum, like the black curves in Figure 5.9 (a) and (b). DP is the point where d^2I/dV^2 curve crosses over zero level. The linear TSS dispersion curves with negative and positive slops appears as negative and positive value plateaus, respectively. Indeed, like shown in both Figure 5.9 (a) and (b), experimental and simulation d^2I/dV^2 curves exhibit consistent and expected behaviors. The determined values of E_F-DP, DP-VBM, and CBm-DP are -0.004 eV, ~ 0.09 eV, and ~ 0.22 eV respectively. Those energies are well matched with corresponding values from APRES study in Figure 5.3, (E_F-DP) ~ 0 eV, (DP-VBM) ~ 0.08 eV, and (CBm-DP) ~ 0.21 eV [89]. As we shall see, we applied d^2I/dV^2 spectroscopy to the study of spatial variation of DP with respect to local composition fluctuation of $Bi_1Sb_1Te_1Se_2$.

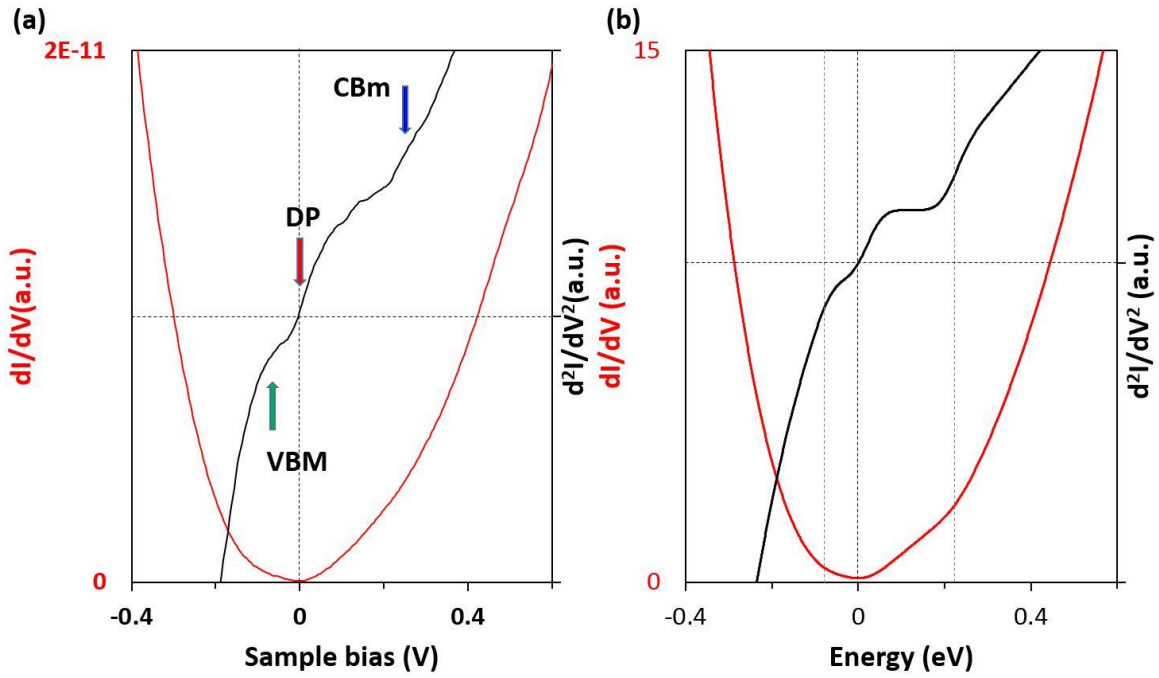

Figure 5.9: Scanning tunneling spectroscopy on $Bi_1Sb_1Te_1Se_2$ at T = 77 K. (a) the red curve is the differential conductivity of tunneling current, corresponding to local density of states of $Bi_1Sb_1Te_1Se_2$. The black curve is the second derivative of tunneling current. Three energy points, DP, CBm, and VBM, are marked by red, blue, and green arrows, respectively. (b) The red curve is a simple simulation of the linear TSS dispersion and bulk bands of $Bi_1Sb_1Te_1Se_2$, and the black for its derivative. The dot lines represent DP, CBm, VBM, and the zero level of the second derivative.

5.3.2 Spatial distribution of Dirac point

Figure 5.10 (a) and (c) were taken before and after acquiring current image tunneling spectroscopy (CITS). The identical triangle in both images moved upwards about 1 nm for 5 hour CITS. It is so slow that the image of Figure 5.10 (b) still exhibits atomic image under the thermal drift of 2 Å/hour. The second derivative spectroscopy gives accurate DP information. Spatial distribution of DP is presented in Figure 5.10 (e). When we counted the number of DPs as a function of energy from Fermi level (E_F), the

distribution center is 8 meV and full width half maximum is 34 meV from Gaussian fit. In this area, there are apparently different kinds of DP, red and blue zones in Figure 5.10 (e). The white dot lines were drawn to help guiding eyes. There seems like the weak correlation of atomic image contrast with DP variation.

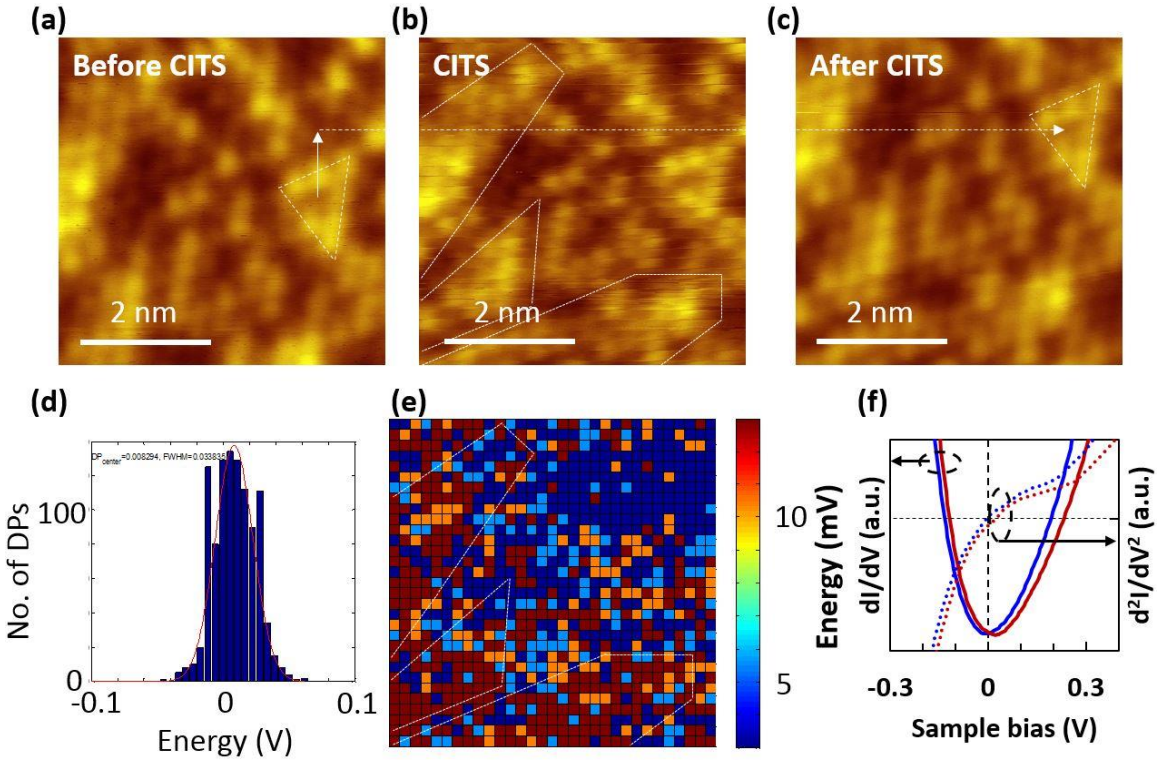

Figure 5.10: Topographic images of (a), (b), and (c) acquired before, during and after CITS, respectively. By tracking an identical triangle in (a) and (c), thermal drift happened about 1 nm for 5 hour CITS. (d) The statistic of DPs. Gaussian fit reveals that distribution center is + 8 meV and FWHM is 34 meV. (e) Spatial distribution of DP. In this location, there are two different DP zones. (f) dI/dV & d^2I/dV^2 spectra at red and blue zones of CITS. δ(DP) = 20 meV and δ(CBm) = 40 meV.

Note that the spectra at red and blue areas exhibit important information: the DP difference is δ(DP) = 20 meV, but the CBm shift is much stronger as δ(CBm) = 40 meV. This means that there is the substantial change of DP distance from CBm; namely, two

areas have difference compositions due to random structure of $Bi_1Sb_1Te_1Se_2$. The truly intriguing observation is that DP in $Bi_1Sb_1Te_1Se_2$ has a strong tendency to remain around Fermi level, despite its spatial composition variation.

5.3.3 Dirac point on line defect

We can seldom see line defects like Figure 5.11 (a) in the $Bi_1Sb_1Te_1Se_2$ sample. Shown in Figure 5.11 (b) is the STS on the defect site, which reveals the same tendency, supporting the previous result. There is a defect state at +0.1 eV over E_F and in the bulk band gap. Nevertheless, DP of the line defect site and E_F stick together. It reflects how strong DP in $Bi_1Sb_1Te_1Se_2$ tends to align themselves at Fermi level.

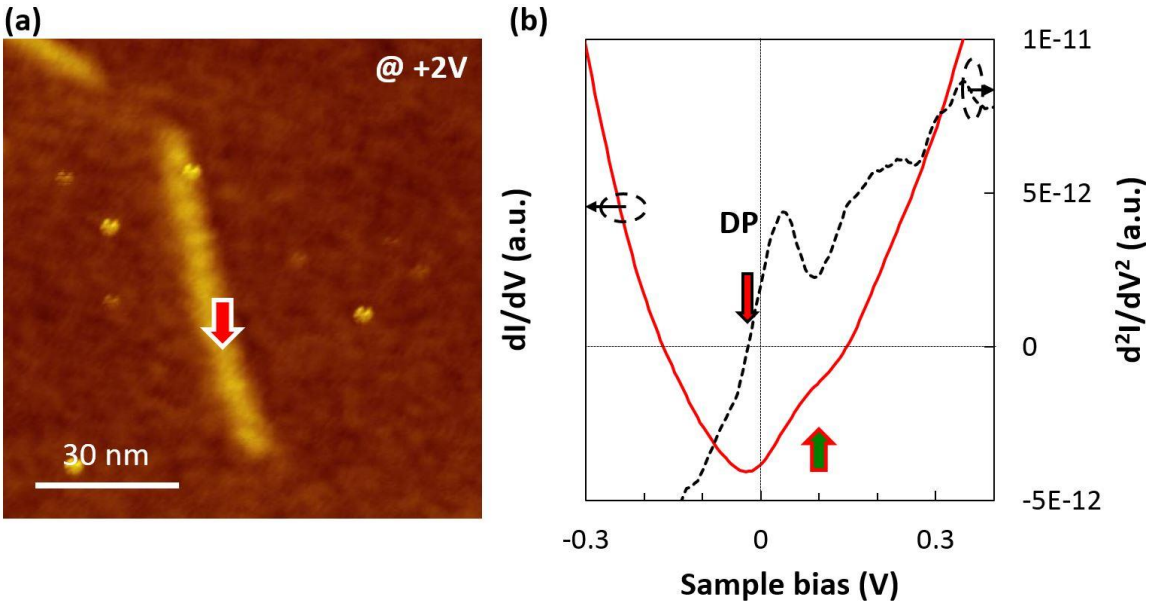

Figure 5.11: (a) Line defect site of 80 pm height. (b) STS on the line defect, at 0.1 eV over E_F. DP is ~ 20 meV slight below E_F.

5.4 Aging effect

Actually, BSTS is not free from aging effect, as previous reports for $Bi_2Te_2Se_1$ and $Bi_{1.5}Sb_{0.5}Te_{1.7}Se_{1.3}$ [89, 90, 93, 94]. For $Bi_2Te_2Se_1$, its ordering feature of quintuple layer like Te-*Bi*-Se-*Bi*-Te could not give resistance against aging effect. But we observed the remarkable stability of our $Bi_1Sb_1Te_1Se_2$ sample even if it has similar structural complexity to $Bi_{1.5}Sb_{0.5}Te_{1.7}Se_{1.3}$.

5.4.1 On Bi_2Te_2Se

To get fresh surface, single crystal of $Bi_2Te_2Se_1$ had been cleaved in the ultrahigh vacuum (UHV) chamber in the order of 10^{-11} torr and then the sample was transferred in one minute to a cold sample stage of T = 77 K to freeze the fresh surface. Like Figure 5. 12 (a), STS spectrum on the fresh surface reveals the band gap is of ~ 0.3 eV, consistent with ARPES study as shown in Figure 5.3. Indeed, Fermi level is in the bulk band gap, but at about 60 meV over E_F. The sample aging was carried out as RT annealing under the same pressure. After aging for around 30 min, E_F apparently moves towards CBm; however, it is still within the bulk band gap. This result is now close to previous ARPES reports. Only 30 min aging leads to substantial E_F shift of more than 0.2 eV. Finally, for 3 day aging, E_F moves inside the bulk conduction band. STS spectrum shows that the bulk conduction band becomes to be slightly complicated as well. Because of the ordering feature of $Bi_2Te_2Se_1$, it was expected that Se atoms would be well trapped in the middle of Bi layers; therefore, the formation of Se vacancies should be suppressed unlike Bi_2Se_3. As our microscopic analysis revealed, 15 % Se occupation in outside quintuple layer, however, most likely induces undesirable aging effect on $Bi_2Te_2Se_1$, despite its structural benefit.

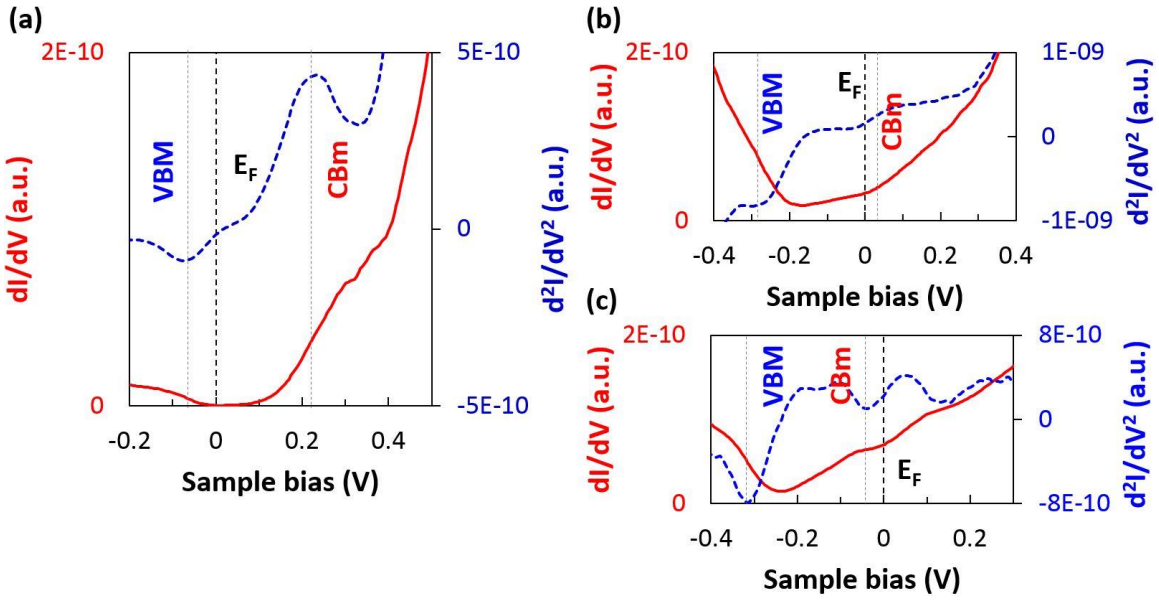

Figure 5.12: Aging effect in $Bi_2Te_2Se_1$: (a) Fresh surface. STS reveals both linear TSS dispersion curve and ~ 0.3 eV bulk band gap. E_F is within band gap, ~ 60 meV over VBM. (b) Aging at RT for ~ 30 min. E_F moved towards nearby CBm but still within bulk band gap. (c) Aging at RT for 3 days. Finally, E_F is inside the bulk conduction band.

5.4.2 On $BiSbTeSe_2$

We applied the same cleaving and aging process to $Bi_1Sb_1Te_1Se_2$. In contrast to previous aging studies, $Bi_1Sb_1Te_1Se_2$ shows the remarkable persistency against aging effect. As we already saw, STS spectrum on the fresh surface in Figure 5.13 (a) has the characteristic features, such as, E_F within the large bulk band gap of ~ 0.3 eV and DP coinciding with E_F. After aging even for one week, as in Figure 5.13 (b), the sample shows no substantial change in band structure at all. Although we do not currently know what gives rise to such robust property, $Bi_1Sb_1Te_1Se_2$ has truly surprising stability and it is really good for application if you consider the aging of $Bi_{1.5}Sb_{0.5}Te_{1.7}Se_{1.3}$ [90].

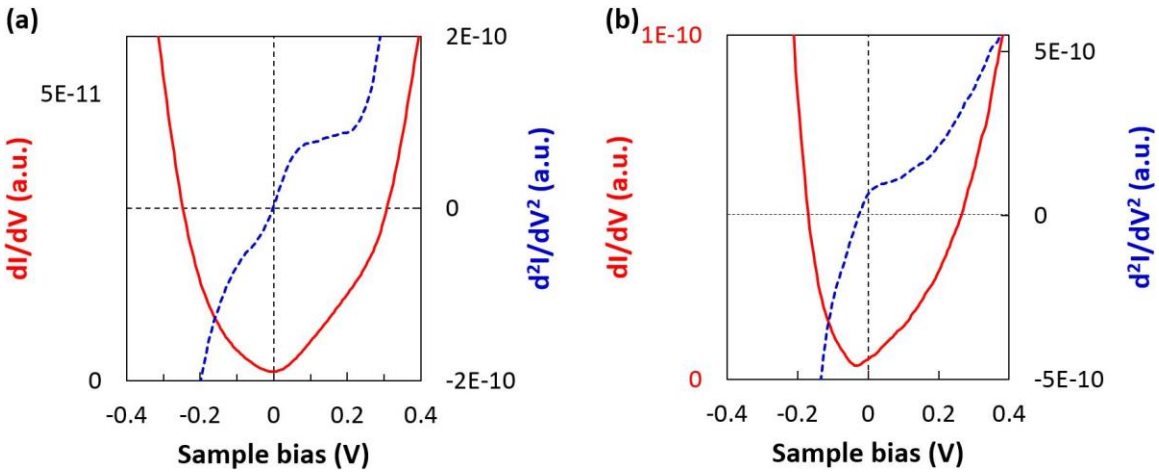

Figure 5.13: Aging effect in $Bi_1Sb_1Te_1Se_2$: (a) Fresh surface. As seen before, E_F is within bulk band gap and apparently coincides with DP. (b) Aging at RT for one week. E_F is still around DP within the band gap. The energy difference is only 20 meV.

5.5 Summary

We studied two intrinsic topological insulators, $Bi_2Te_2Se_1$ and $Bi_1Sb_1Te_1Se_2$, with respect to their structure and stability. In comparison to the XRD spectrum, scanning tunneling spectroscopy showed that $Bi_2Te_2Se_1$ is an order alloy, whereas $Bi_1Sb_1Te_1Se_2$ is a random alloy. Scanning tunneling spectroscopy confirmed that DP has a strong tendency to self-align around Fermi level within the bulk band gap, even on the defect site, despite its random arrangement. Moreover, $Bi_1Sb_1Te_1Se_2$ has remarkably strong stability against aging if the aging effect on $Bi_{1.5}Sb_{0.5}Te_{1.7}Se_{1.3}$ were considered. Even after annealing at RT for seven days, the band structure is almost identical to that prior to aging. Both observations for $Bi_1Sb_1Te_1Se_2$ are very important for application to utilize exotic topological surface properties under surface dominant conduction.

Appendix

A.1 Matlab code

Note that all input txt files should be pure data without labels.

A.1.1 Savitzky-Golay Method [96] for Numerical Derivative of Raw Data

```
%%%%%%%%%%%%%%%%%%%%%%%%%%%%%%%%%%%%%%%%%%%%%%%%%%%%%%%%%%%%%%%%%%%%%%%%
%%%%%%%%% load raw data %%%%%%%%%%%%%%%%%%%%%%%%%%%%%%%%%%%%%%%%%%%%%%%%
%%%%%%%%%%%%%%%%%%%%%%%%%%%%%%%%%%%%%%%%%%%%%%%%%%%%%%%%%%%%%%%%%%%%%%%%
answer0 = inputdlg({'File Name(ex) GEPB0000)'},...
                   'Enter the file name',...
                   1,...
                   {'PSIC0170a'});
raw_data=load([answer0{1} '.txt']);
[p q]=size(raw_data);
Vias=raw_data(:,1);
dx=Vias(2)-Vias(1);
Vias1=Vias;
%%%%%%%%%%%%%%%%%%%%%%%%%%%%%%%%%%%%%%%%%%%%%%%%%%%%%%%%%%%%%%%%%%%%%%%%
%%%%%%%% Savitzky-Golay Method %%%%%%%%%%%%%%%%%%%%%%%%%%%%%%%%%%%%%%%%%
%%%%%%%%%%%%%%%%%%%%%%%%%%%%%%%%%%%%%%%%%%%%%%%%%%%%%%%%%%%%%%%%%%%%%%%%
answer1 = inputdlg({'Order of polynomial fit', 'Window length(Odd
No.)'},...
                   'Parameters for Savitzky-Golay Method',...
                   1,...
                   {'4', '11'});
OP=str2double(answer1{1}); % Order of Polynomial fit
WL=str2double(answer1{2}); % Window Length
[b, g]=sgolay(OP,WL);
%%%%%%%%%%%%%%%%%%%%%%%%%%%%%%%%%%%%%%%%%%%%%%%%%%%%%%%%%%%%%%%%%%%%%%%%
SG0_data=zeros(p,q-1);
SG1_data=zeros(p,q-1);
SG2_data=zeros(p,q-1);
HW=((WL+1)/2)-1;
for i1=1:q-1
    for i2=1:p
        if i2 < HW+1
            %%%%% data on the left hand side %%%%%%
            SG0_data(i2,i1)=0;
            SG1_data(i2,i1)=0;
            %%%%%%%%%%%%%%%%%%%%%%%%%%%%%%%%%%%%%%%%%%%%%%%%%%%%%%%%%%%%%%%%
        elseif i2 > p-HW
            %%%%% data on the right hand side %%%%%
            SG0_data(i2,i1)=0;
            SG1_data(i2,i1)=0;
            %%%%%%%%%%%%%%%%%%%%%%%%%%%%%%%%%%%%%%%%%%%%%%%%%%%%%%%%%%%%%%%%
        else
```

```
            %%%%% otherwise %%%%%%%%%%%%%%%%%%%%%%
            SG0_data(i2,i1)=dot(g(:,1), raw_data(i2-HW:i2+HW,i1+1));
            SG1_data(i2,i1)=dot(g(:,2), raw_data(i2-HW:i2+HW,i1+1));
            %%%%%%%%%%%%%%%%%%%%%%%%%%%%%%%%%%%%%%
        end
    end
end
Vias1([1:HW, (p-HW+1):p])=[];
SG0_data([1:HW, (p-HW+1):p],:)=[];
SG1_data([1:HW, (p-HW+1):p],:)=[];
SG1_data=SG1_data/dx;
%%%%%%%%%%%%%%%%%%%%%%%%%%%%%%%%%%%%%%%%%%%%%%%%%%%%%%%%
%%%%%%%%%%%%%%%% Plot the results %%%%%%%%%%%%%%%%%%%%%
%%%%%%%%%%%%%%%%%%%%%%%%%%%%%%%%%%%%%%%%%%%%%%%%%%%%%%%%
subplot(1,2,1)
plot(Vias,raw_data(:,end),'b',Vias1,SG0_data(:,end),'r')
title(['(Order, WL)=( ' answer1{1} ', ' answer1{2} ')'])
grid on
axis tight
subplot(1,2,2)
plot(Vias1,SG1_data(:,end),'r')
title(answer0{1})
grid on
axis tight

SG0=[Vias1 SG0_data];
SG1=[Vias1 SG1_data];
%%%%%%%%%%%%%%%%%%%%%%%%%%%%%%%%%%%%%%%%%%%%%%%%%%%%%%%%
%%%%%%%%%%%%%%%% Save data %%%%%%%%%%%%%%%%%%%%%%%%%%%%
%%%%%%%%%%%%%%%%%%%%%%%%%%%%%%%%%%%%%%%%%%%%%%%%%%%%%%%%
check_Q=menu('Do you want to save it?',...
             'Yes',...
             'No');
if check_Q == 1
    save([answer0{1} '_SG0.txt'],'SG0','-ASCII');
    save([answer0{1} '_SG1.txt'],'SG1','-ASCII');
end
%%%%%%%%%%%%%%%%%%%%%%%%%%%%%%%%%%%%%%%%%%%%%%%%%%%%%%%%
%%%%%%%%%%%%%%%%%%%% End %%%%%%%%%%%%%%%%%%%%%%%%%%%%%%
%%%%%%%%%%%%%%%%%%%%%%%%%%%%%%%%%%%%%%%%%%%%%%%%%%%%%%%%
```

A.1.2 Temperature Dependence of Superconducting Gap

Figure 2.9 is one of the examples produced by using this program.

```
%%%%%% The default values are for Pb %%%%%%%
answer0 = inputdlg({'T_c[K]', '2*Delta(0)/k_b T_c', 'Debye
Temperature[K]'},...
                   'Enter Parameters for the Calculation of
Delta(T)!',...
                    1,...
```

```
                    {'7.3', '4.3','88'});

%%%%% Basic Physical Value %%%%%%%%%%%%%%%%
kb=8.617332478e-2; %[meV/K]
hbar=6.5821192815e-13; % [meV*s]
%%%%%%%%%%%%%%%%%%%%%%%%%%%%%%%%%%%%%%%%%%%%
Tc=str2double(answer0{1});
r_factor=str2double(answer0{2});
Theta=str2double(answer0{3});
gap0=r_factor*kb*Tc/2;

hbarwD=kb*Theta; %[meV] obtain Debye frequency from Debye temperature.
int_up=hbarwD/(2*kb*Tc);

%%%%%% delta =0 at t=1 (T=Tc) %%%%%%%%%%%%%%%%%%%
%%%%%% in order to get 1/vN %%%%%%%%%%%%%%%%
inv_vN=quadl(@(x)integrand_Tc(x,0,1),0,int_up);
%%%%%%%%%%%%%%%%%%%%%%%%%%%%%%%%%%%%%%%%%%%%

t=linspace(0,1,500)'; % Reduced Temperatue: t=T/Tc
r_gap=zeros(size(t)); % Reduced Gap: r_gap = gap/2kbTc

for i=1:size(t,1)
    %%%% The unit of Tc calculation at a certain Temperature %%%
    delta0=1;
    inc_delta=0.2;
    f0=quadl(@(x)integrand_Tc(x,delta0,t(i)),0,int_up);
    if abs(f0-inv_vN)>=1e-6
        check_0=2;
        delta=delta0-inc_delta;
    else
        check_0=1;
        r_gap(i)=delta0;
    end
    while check_0==2
        f=quadl(@(x)integrand_Tc(x,delta,t(i)),0,int_up);
        if abs(f-inv_vN)<=1e-6
            check_0=1;
            r_gap(i)=delta;
        else
            if f>f0
                if (f-inv_vN)*(f0-inv_vN) >= 0
                    if f>inv_vN
                        delta1=delta;
                        delta=delta0+(delta0-delta1);
                    else
                        delta1=delta0;
                        delta0=delta;
                        delta=delta0-(delta1-delta0);
                    end
                else
                    delta1=delta0;
```

```
                    delta0=delta;
                    delta=delta0+0.5*(delta1-delta0);
                end
            else
                if (f-inv_vN)*(f0-inv_vN) >= 0
                    if f0>inv_vN
                        delta1=delta0;
                        delta0=delta;
                        delta=delta0+(delta0-delta1);
                    else
                        delta1=delta;
                        delta=delta0-(delta1-delta0);
                    end
                else
                    delta1=delta0;
                    delta0=delta;
                    delta=delta0-0.5*(delta0-delta1);
                end
            end
            f0=f;
        end
    end
end
r_gap=r_gap*1.13; %in order to change gap/2kbTc to gap/gap(T=0)
Gap=r_gap*gap0;
Temp=t*Tc;
figure(1)
plot(t,r_gap,'r')
figure(2)
plot(Temp,Gap,'r')
hold on
%%%%%% Experimental Data %%%%%%%%%%%%%%%%%%%%
plot([2.2 4.3 5.1 5.9],[1.22 1.07 0.91 0.815],'bo')
xlabel('T[K]')
ylabel('Delta[meV]')
title(['(' answer0{1} '[K], ' num2str(gap0) '[meV])'])


data_Tc=[t r_gap Temp Gap];
choice_Save = menu('Do you want to save this result?',...
                   'Yes',...
                   'No');
if choice_Save ==1
    answer2 = inputdlg({'File Name'},...
                        'Enter the file name',...
                         1,...
                       {'BCS_Tc'});
    save([answer2{1} '.txt'],'data_Tc','-ASCII');
end
%%%%%%%%%%%%%%%%%%%%%%%%%%%%%%%%%%%%%%%%%%%%%%%%%%%%
%%%%%%%%%%%%%%%%%%%% End %%%%%%%%%%%%%%%%%%%%%%%%%%
%%%%%%%%%%%%%%%%%%%%%%%%%%%%%%%%%%%%%%%%%%%%%%%%%%%%
```

```
%%%%%%%%%%%%%%%%%%%%%%%%%%%%%%%%%%%%%%%%%%%%%%%%%%%%%%%%%%%%%%%%%%%%%%%
%%%%%%%%%%%%%%%%%%%%%% subfunction %%%%%%%%%%%%%%%%%%%%%%%%%%%%%%%%%%%%
%%%%%%%%%%%%%%%%%%%%%%%%%%%%%%%%%%%%%%%%%%%%%%%%%%%%%%%%%%%%%%%%%%%%%%%
function y=integrand_Tc(x,a,t)
% x is a reduced energy.
% a is a reduced gap.
% t is a reduced temperature.
y1=sqrt(x.^2+a.^2);
if t==0
    y=1./y1;
else
    y=tanh(y1/t)./y1;
end
%%%%%%%%%%%%%%%%%%%%%%%%%%%%%%%%%%%%%%%%%%%%%%%%%%%%%%%%%%%%%%%%%%%%%%%
%%%%%%%%%%%%%%%%%%%%%% End %%%%%%%%%%%%%%%%%%%%%%%%%%%%%%%%%%%%%%%%%%%%
%%%%%%%%%%%%%%%%%%%%%%%%%%%%%%%%%%%%%%%%%%%%%%%%%%%%%%%%%%%%%%%%%%%%%%%
```

A.1.3 CITS and Line Spectroscopy

Figure 1.6 shows how to utilize this program.

```
%%%%%%%%%%%%%%%%%%%%%%%%%%%%%%%%%%%%%%%%%%%%%%%%%%%%%%%%%%%%%%%%%%%%%%%
%%%%%%%%% load raw data %%%%%%%%%%%%%%%%%%%%%%%%%%%%%%%%%%%%%%%%%%%%%%%
%%%%%%%%%%%%%%%%%%%%%%%%%%%%%%%%%%%%%%%%%%%%%%%%%%%%%%%%%%%%%%%%%%%%%%%
filename ='CITS_PBAG0576';%Change file name here!!!!
m=load([filename '.txt']);
m_min=min(min(m));
m_max=max(max(m));
answer = inputdlg({'Lateral Size(nm)', 'Resolution(64X64)'},...
    'Enter lateral size of the image and its resolution!!!',...
    1,...
    {'64','64'});
scale.size=str2num(answer{1}); %[nm]
scale.resolution=str2num(answer{2});
scale.factor=scale.size/scale.resolution; % nm/pixel
biasoffset=0;
[p q]=size(m);
V_bias=m(:,1)-biasoffset;
CITS.dIdV=m(:,2:(end-1));
%%%%%%%%%%%%%%%%%%%%%%%%%%%%%%%%%%%%%%%%%%%%%%%%%%%%%%%%%%%%%%%%%%%%%%%
%%%%%% plot CITS image to draw a line%%%%%%%%%%
answer = inputdlg({'Bias'},...
                  'What bias do you want to plot CITS at',...
                   1,...
                   {'0'});
CITS.bias=str2num(answer{1});

choice1 =1;
choice2 =1;
choice3 =1;
choice4 =1;
```

```
cmin=1e-9;
cmax=1e-8;
while choice1 == 1
    for index1=1:(p-1)
        if V_bias(index1) >= CITS.bias
            if V_bias(index1+1) < CITS.bias
                CITS.data=CITS.dIdV(index1,:);
                for index2=1:scale.resolution
                    for index3=1:scale.resolution
                        CITS.mtrx(index2, index3)...
                            =CITS.data(scale.resolution*(index2-
1)+index3);
                    end
                end
            end
        end
    end

    figure(1)
    surf(CITS.mtrx,'EdgeColor','none')
    colormap('hot')
    axis([1 scale.resolution 1 scale.resolution  m_min m_max])
    colorbar
    view([180 90])
    while choice2 == 1
        answer = inputdlg({'c_min','c_max'},...
            'Color Axis Scaling',...
            1,...
            {num2str(cmin),num2str(cmax)});
        cmin=str2num(answer{1});
        cmax=str2num(answer{2});
        caxis([cmin cmax])
        choice2 = menu('Do you want to change color axis scaling?',...
            'Yes',...
            'No');
    end
    hold on

    choice1 = menu('Do you want to change bias?',...
              'Yes',...
              'No');
    if choice1 ==1
        answer = inputdlg({'Bias'},...
                  'What bias do you want to plot CITS at',...
                   1,...
                   {'0'});
        CITS.bias=str2num(answer{1});
    end
end
%%%%%%%%%%%%%%%%%%%%%%%%%%%%%%%%%%%%%%%%%%%%
%%%%%%%%%% To get the number of lines %%%%%
answer = inputdlg({'The Number of Lines'},...
```

```
    'Enter the number of lines',...
    1,...
    {'1'});
num_line=2*round((str2num(answer{1})-1)/2)+1;
%%%%%%%%%%%%%%%%%%%%%%%%%%%%%%%%%%%%%%%%%%%%%%%
%%%%%%%%%%% Draw a Line %%%%%%%%%%%%%%%%%
%%%%%%%%%%%%%%%%%%%%%%%%%%%%%%%%%%%%%%%%%%%%%%%
hold on
while choice4 == 1
    [xx yy]=ginput(2);
    xx=round(xx)';
    yy=round(yy)';
    zz=[m_max m_max];
    plot3(xx,yy,zz,'w--','LineWidth',1.5)
    if abs(xx(2)-xx(1)) >= abs(yy(2)- yy(1))
        x.xi=[xx(1):sign(xx(2)-xx(1)):xx(2)];
        y.yi=round((yy(2)-yy(1))/(xx(2)-xx(1))*(x.xi-xx(1)))+yy(1);
        ri=scale.factor*sqrt((x.xi-x.xi(1)).^2+(y.yi-y.yi(1)).^2);
%[nm]
        num_case=1;
    else
        y.yi=[yy(1):sign(yy(2)-yy(1)):yy(2)];
        x.xi=round((xx(2)-xx(1))/(yy(2)-yy(1))*(y.yi-yy(1)))+xx(1);
        ri=scale.factor*sqrt((x.xi-x.xi(1)).^2+(y.yi-y.yi(1)).^2);
%[nm]
        num_case=2;
    end
%%%%%%%%%%%%%%%%%%%%%%%%%%%%%%%%%%%%%%%%%%%%%%%
%%%%%%%%%%%%%%% Line Spectra %%%%%%%%%%%%%%%
%%%%%%%%%%%%%%%%%%%%%%%%%%%%%%%%%%%%%%%%%%%%%%%
    CITS.lineSPC=[];
    for index4=1:max(size(x.xi))
        LSPC=[];
        if num_case == 1
            for index5 = 1:num_line
                LSPC=[LSPC CITS.dIdV(:,x.xi(index4)+round(-(yy(2)-
yy(1))/(xx(2)-xx(1))*(index5-
round(num_line/2)))+scale.resolution*(y.yi(index4)+(index5-
round(num_line/2))-1))];
            end
        else
            for index5 = 1:num_line
                LSPC=[LSPC CITS.dIdV(:,x.xi(index4)+(index5-
round(num_line/2))+scale.resolution*(y.yi(index4)+round(-(xx(2)-
xx(1))/(yy(2)-yy(1))*(index5-round(num_line/2)))-1))];
            end
        end
        s_LSPC=sum(LSPC,2)/num_line;
        CITS.lineSPC=[CITS.lineSPC s_LSPC];
    end

    figure(2)
```

```
    [R Y]=meshgrid(ri,V_bias);
    surf(R, Y, CITS.lineSPC,'EdgeColor','none')
    xlabel('Distance(nm)')
    ylabel('Bias(V)')
    colormap('Hot')
    axis([min(min(R)) max(max(R)) min(min(Y)) max(max(Y))])
    colorbar
    view([0 90])
    while choice3 == 1
        answer = inputdlg({'c_min','c_max'},...
            'Color Axis Scaling',...
            1,...
            {num2str(cmin),num2str(cmax)});
        cmin=str2num(answer{1});
        cmax=str2num(answer{2});
        caxis([cmin cmax])
        choice3 = menu('Do you want to change color axis scaling?',...
            'Yes',...
            'No');
    end
    choice5 = menu('Do you want to save this line profile?',...
            'Yes',...
            'No');
    if choice5 == 1
        answer = inputdlg({'File Name'},...
            'Enter the file name',...
            1,...
            {[filename '_lineprofile']});
        %%%%%%%%%%%%%%% Save the result %%%%%%%%%%%%%%%
        linSPC_m=CITS.lineSPC;
        linSPC_m=[V_bias linSPC_m]; % include the bias.
        linSPC_m=[0 ri; linSPC_m];
        save([answer{1} '.txt'],'linSPC_m','-ASCII');
        %%%%%%%%%%%%%%%%%%%%%%%%%%%%%%%%%%%%%%%%%%%%%%%
    end
    choice4 = menu('Do you want to try another line?',...
            'Yes',...
            'No');
    if choice4 == 1
        choice3 = 1;
        close(2);
    end
end
%%%%%%%%%%%%%%%%%%%%%%%%%%%%%%%%%%%%%%%%%%%%%%%%%%%%
%%%%%%%%%%%%%%%%%%%% End %%%%%%%%%%%%%%%%%%%%%%%%%%%
%%%%%%%%%%%%%%%%%%%%%%%%%%%%%%%%%%%%%%%%%%%%%%%%%%%%
```

If you are interested in other programs, feel free to contact to author.

Bibliography

1. G. Binning and H. Rohrer, Scanning tunneling microscopy, *Helv. Phys. Acta.* **55**, 726 (1982).
2. G. Binning et al, 7 x 7 reconstruction on Si(111) resolved in real space, *Phys. Rev. Lett.* **50**, 120 (1983).
3. K. Takayanagi et al, Structure analysis of Si(111)-7 x 7 reconstructed surface by transmission electron diffraction, *Surf. Sci.* **164**, 367 (1985).
4. C. J. Chen, Introduction to scanning tunneling microscopy, *Oxford University Press* (1993).
5. R. Wiesendanger, Scanning probe microscopy and spectroscopy - Methods and applications, *Cambridge University Press* (1994).
6. I. Giaever, Energy gap in superconductors measured by electron tunneling, *Phys. Rev. Lett.* **5**, 147 (1960).
7. J. Bardeen, L. N. Cooper, and J. R. Schrieffer, Microscopic theory of superconductivity, *Phys. Rev.* **106**, 162 (1957).
8. J. Bardeen, Tunneling from a many-body point of view, *Phys. Rev. Lett.* **6**, 57 (1960).
9. L. D. Landau and L. M. Lifshitz, Quantum Mechanics, *Pergmon Press* (1977).
10. G. Binning et al, Tunneling through a controllable vacuum gap, *Appl. Phys. Lett.* **40**, 178 (1982).
11. S. H. Pan, E. W. Hudson, and J. C. Davis, Vacuum tunneling of superconducting quasiparticles from atomically sharp scanning tunneling microscope tips, *Appl. Phys. Lett.* **73**, 2992 (1998).

12. S. H. Pan, E. W. Hudson, and J. C. Davis, 3He refrigerator based very low temperature scanning tunneling microscope, *Rev. Sci. Instr.* **70**, 1459 (1999).
13. S. H. Pan, Piezoelectric motor, *International Patent Publication No.* **WO 93/19494** (30 September 1993).
14. D. J. Eom, Low temperature scanning tunneling microscope study of metallic thin films on the semiconductor substrates, *PhD Dissertation* (2005).
15. J. D. Kim, Low temperature scanning tunneling microscope study of low-dimensional superconductivity on metallic nanostructures, *PhD Dissertation* (2010).
16. http://www.datasheetlib.com/datasheet/425586/1202-005_spectrum-advanced-specialty-products.html?page=11#datasheet.
17. N. E. Promisel, Tungsten, Tantalum, Molybdenum, Niobium and their alloys, *Pergamon Press, New York* (1964).
18. R. M. Feenstra, J. A. Stroscio, and A. P. Fein, Tunneling spectroscopy of the Si(111) 2x1 surface, *Surf. Sci.* **181**, 295 (1987).
19. L. W. Swanson and L. C. Crouser, Total-energy distribution of field-emitted electrons and single-plane work functions for tungsten, *Phys. Rev.* **163**, 622 (1967).
20. R. F. Willis and B. Feuerbacher, Angular-resolved secondary-electron-emission spectroscopy of clean and adsorbate covered tungsten single-crystal surface, *Surf. Sci.* **53**, 144 (1975).
21. W. Drube et al., Unoccupied surface states on W(001) and Mo(001) by inverse photoemission, *Phys. Rev. B* **34**, 8989 (1986).
22. R. H. Gaylord et al., Experimental Fermi surfaces of clean and hydrogen-covered W(110), *Phys. Rev. Lett.* **62**, 2036 (1989).

23. H. K. Onnes, The resistance of pure mercury at helium temperatures. *Leiden Comm.* **120b** (1911).
24. H. K. Onnes, The disappearance of the resistance of mercury, *Leiden Comm.* **122b** (1911).
25. H. K. Onnes, On the sudden change in the rate at which the resistance of mercury disappears, *Leiden Comm.* **124c** (1911).
26. W. Meissner and R. Ochsenfeld, A new effect concerning the onset of superconductivity, *Naturwissenschaften* **21**, 787 (1933).
27. F. London and H. London, The electromagnetic equations of the superconductor, *Proc. Roy. Soc.* **149**, 71 (1935).
28. J. Bardeen, L. N. Cooper, and J. R. Schrieffer, Theory of superconductivity, *Phys. Rev.* **108**, 1175 (1957).
29. T. E. Faber and A. B. Pippard, The penetration depth and high-frequency resistance of superconducting aluminium, *Proc. Roy. Soc. Lon.* **231**, 336 (1955).
30. V. L. Ginzburg and L. D. Landau, On the theory of superconductivity, *Zh. Eksperim. i. Teor. Fiz.* **20**, 1064 (1950).
31. L. P. Gor'kov, Microscopic derivation of the Ginzburg-Landau equations in the theory of superconductivity, *Sov. Phys. JETP* **36**, 1364 (1959).
32. J. Bardeen, L. N. Cooper, and J. R. Schrieffer, Theory of superconductivity, *Phys. Rev.* **108**, 1175 (1957).
33. L. N. Cooper, Bound electron pairs in a degenerate Fermi gas, *Phys. Rev.* **104**, 1189 (1956).
34. E. Maxwell, Isotope effect in the superconductivity of mercury, *Phys. Rev.* **78**, 477 (1950).

35. C. A. Reynolds, B. Serin, W. H. Wright, and L. B. Nesbitt, Superconductivity of isotopes of mercury, *Phys. Rev.* **78**, 487 (1950).

36. J. W. Rohlf, Modern physics from α to Z^0, *John Wiley & Sons, Inc.* (1994).

37. M. Tinkham, Introduction to superconductivity, *Dover Publications, Inc.* (1996).

38. A. K. Geim *et al.*, Phase transitions in individual sub-micrometre superconductors. *Nature* **390**, 259 (1997).

39. A. Bezryadin, C. N. Lau, M. Tinkham, Quantum suppression of superconductivity in ultrathin nanowires. *Nature* **404**, 971 (2000).

40. Y. Guo *et al.*, Superconductivity modulated by quantum size effects. *Science* **306**, 1915 (2004).

41. D. Eom, S. Qin, M. Y. Chou, C. K. Shih, Persistent superconductivity in ultrathin Pb films: A scanning tunneling spectroscopy study. *Phys. Rev. Lett.* **96**, 027005 (2006).

42. M. M. Ozer, J. R. Thompson, H. H. Weitering, Hard superconductivity of a soft metal in the quantum regime. *Nat. Phys.* **2**, 173 (2006).

43. T. Nishio *et al.*, Superconducting Pb island nanostructures studied by scanning tunneling microscopy and spectroscopy. *Phys. Rev. Lett.* **101**, 167001 (2008).

44. M. M. Ozer, Y. Jia, Z. Y. Zhang, J. R. Thompson, H. H. Weitering, Tuning the quantum stability and superconductivity of ultrathin metal alloys. *Science* **316**, 1594 (2007).

45. N. Reyren *et al.*, Superconducting interfaces between insulating oxides. *Science* **317**, 1196 (2007).

46. M. Strongin, R. S. Thompson, O. F. Kammerer, J. E. Crow, Destruction of superconductivity in disordered near-monolayer films. *Physical Review B-Solid State* **1**, 1078 (1970).

47. G. J. Dolan, J. Silcox, Critical thicknesses in superconducting thin films. *Phys. Rev. Lett.* **30**, 603 (1973).

48. B. G. Orr, H. M. Jaeger, A. M. Goldman, Transition-temperature oscillations in thin superconducting films. *Phys. Rev. Lett.* **53**, 2046 (1984).

49. R. C. Dynes, A. E. White, J. M. Graybeal, J. P. Garno, Breakdown of Eliashberg theory for two-dimensional superconductivity in the presence of disorder. *Phys. Rev. Lett.* **57**, 2195 (1986).

50. D. B. Haviland, Y. Liu, A. M. Goldman, Onset of superconductivity in the two-dimensional limit. *Phys. Rev. Lett.* **62**, 2180 (1989).

51. A. Yazdani, A. Kapitulnik, Superconducting-insulating transition in two-dimensional a-MoGe Thin Films. *Phys. Rev. Lett.* **74**, 3037 (1995).

52. M. Hermele, G. Refael, M. P. A. Fisher, P. M. Goldbart, Fate of the Josephson effect in thin-film superconductors. *Nat. Phys.* **1**, 117 (2005).

53. I. Hetel, T. R. Lemberger, M. Randeria, Quantum critical behaviour in the superfluid density of strongly underdoped ultrathin copper oxide films. *Nat. Phys.* **3**, 700 (2007).

54. S. Y. Qin, J. Kim, Q. Niu, C. K. Shih, Superconductivity at the two-dimensional limit. *Science* **324**, 1314 (2009).

55. J. Kim *et al.*, Visualization of geometric influences on proximity effects in heterogeneous superconductor thin films. *Nat. Phys.* **8**, 464 (2012).

56. T. Uchihashi, P. Mishra, M. Aono, T. Nakayama, Macroscopic superconducting current through a silicon surface reconstruction with indium adatoms: Si(111)-($\sqrt{7} \times \sqrt{3}$)-In. *Phys. Rev. Lett.* **107**, 207001 (2011).

57. S. Y. Tan *et al.*, Interface-induced superconductivity and strain-dependent spin density waves in FeSe/SrTiO3 thin films. *Nat. Mater.* **12**, 634 (2013).

58. M. Hupalo, J. Schmalian, M. C. Tringides, "Devil's staircase" in Pb/Si(111) ordered phases. *Phys. Rev. Lett.* **90**, 216109 (2003).

59. S. M. Lu *et al.*, Scanning tunneling spectroscopy observation of electronic resonances originating from 1 x 1 potential on the dense Pb overlayer on Si(111). *Jpn. J. Appl. Phys.* **51**, 015702 (2012).

60. A. R. Smith, K. J. Chao, Q. Niu, C. K. Shih, Formation of atomically flat silver films on GaAs with a "silver mean" quasi periodicity. *Science* **273**, 226 (1996).

61. K. D. Wang, X. Q. Zhang, M. M. T. Loy, T. C. Chiang, X. D. Xiao, Pseudogap mediated by quantum-size effects in lead islands. *Phys. Rev. Lett.* **102**, 076801 (2009).

62. J. Kim, G. A. Fiete, H. Nam, A. H. MacDonald, C. K. Shih, Universal quenching of the superconducting state of two-dimensional nanosize Pb-island structures. *Phys. Rev. B* **84**, 014517 (2011).

63. I. Brihuega *et al.*, Experimental observation of thermal fluctuations in single superconducting Pb nanoparticles through tunneling measurements. *Phys. Rev. B* **84**, 104525 (2011).

64. J. R. Kirtley *et al.*, Scanning SQUID susceptometry of a paramagnetic superconductor. *Phys. Rev. B* **85**, 224518 (2012).

65. V. J. Emery and S. A. Kivelson, Importance of phase fluctuations in superconductors with small superfluid density, *Nature* **374**, 434 (1995).

66. M. Tinkham, Effect of fluxoid quantization on transitions of superconducting films. *Phys. Rev.* **129**, 2413 (1963).

67. J. M. Kosterlitz and D. J. Thouless, Ordering, metastability and phase transitions in two-dimensional systems, *J. Phys. C* **6**, 1181 (1973).

68. P. M. Chaikin and T. C. Lubensky, Principles of condensed matter physics, Cambridge University Press (1995).
69. D. J. Bishop and J. D. Reppy, Study of the superfluid transition in two-dimensional ^{4}He films, *Phys, Rev. Lett.* **40**, 1727 (1978)
70. D. McQueeney, G. Agnolet, and J. D. Reppy, Surface superfluidity in dilute ^{4}He-^{3}He mixtures, *Phys. Rev. Lett.* **52**, 1325 (1984).
71. W. Zhao et al, Evidence for Berezinskii-Kosterlitz-Thouless transition in atomically flat two-dimensional Pb superconducting films, *Sol. St. Comm.* **165**, 59 (2013).
72. T. Sekihara, R. Masutomi, and T. Okamoto, Two-dimensional superconducting state of monolayer Pb films grown on GaAs(110) in a strong parallel magnetic field, *Phys. Rev. Lett.* **111**, 057005 (2013).
73. K. Yaji et al, Large Rashba spin splitting of a metallic surface-state band on a semiconductor surface, *Nat. Comm.* **1**, 17 (2010).
74. D. Hsieh *et al*, A topological Dirac insulator in a quantum spin Hall phase, *Nature* **452**, 970 (2008).
75. J. E. Moore, The birth of topological insulators, *Nature* **464**, 194 (2010).
76. P. D. C. King *et al*, Large tunable Rashba spin splitting of a two-dimensional electron gas in Bi_2Se_3, *Phys. Rev. Lett.* **107**, 096802 (2011).
77. Y. Zhang *et al*, Crossover of the three-dimensional topological insulator Bi_2Se_3 to the two-dimensional limit, *Nat. Phys.* **6**, 584 (2010).
78. C. Mann *et al*, Mapping the 3D surface potential in Bi_2Se_3, *Nat. Comm.* **4**, 2277 (2013).

79. Y. Ando *et al*, Electrical detection of the spin polarization due to charge flow in the surface state of the topological insulator $Bi_{1.5}Sb_{0.5}Te_{1.7}Se_{1.3}$, *Nano Lett.* **14**, 6226 (2014).

80. C. L. Kane and E. J. Mele, Z_2 topological order and the quantum spin Hall effect, *Phys. Rev. Lett.* **95**, 146802 (2005).

81. Y. S. Fu *et al*, Imaging the two-component nature of Dirac-Landau levels in the topological surface state of Bi_2Se_3, *Nat. Phys.* **10**, 815 (2014).

82. B. Xia *et al*, Indications of surface-dominated transport in single crystalline nanoflake devices of topological insulator $Bi_{1.5}Sb_{0.5}Te_{1.8}Se_{1.2}$, *Phys. Rev. B* **87**, 085442 (2013).

83. H. Zhang *et al*, Topological insulators in Bi_2Se_3, Bi_2Te_3 and Sb_2Te_3 with a single Dirac cone on the surface, *Nat. Phys.* **5**, 438 (2009).

84. Y. Xia *et al*, Observation of a large-gap topological-insulator class with a single Dirac cone on the surface, *Nat. Phys.* **5**, 398 (2009).

85. S. Urazhdin *et al*, Surface effects in layered semiconductors Bi_2Se_3 and Bi_2Te_3, *Phys. Rev. B.* **69**, 085313 (2004).

86. M. Bianchi *et al*, Simultaneous quantization of bulk conduction and valence states through adsorption of nonmagnetic impurities on Bi_2Se_3, *Phys. Rev. Lett.* **107**, 086802 (2011).

87. H. M. Benia *et al*, Reactive chemical doping of the Bi_2Se_3 topological insulator, *Phys. Rev. Lett.* **107**, 177602 (2011).

88. D. Hsieh *et al*, Observation of time-reversal-protected single-Dirac-cone topological-insulator states in Bi_2Te_3 and Sb_2Te_3, *Phys. Rev. Lett.* **103**, 146401 (2009).

89. T. Arakane *et al*, Tunable Dirac cone in the topological insulator $Bi_{2-x}Sb_xTe_{3-y}Se_y$, *Nat. Comm.* **3**, 636 (2012).

90. S. Kim *et al*, Robust protection from backscattering in the topological insulator $Bi_{1.5}Sb_{0.5}Te_{1.7}Se_{1.3}$, *Phys. Rev. Lett.* **112**, 136802 (2014) & its supplementary.

91. Y. Xu *et al*, Observation of topological surface state quantum Hall effect in an intrinsic three-dimensional topological insulator, *Nat. Phys.* **10**, 956, (2014) & supplementary.

92. M. Bianchi *et al*, The electronic structure of clean and adsorbate-covered Bi_2Se_3: an angle-resolved photoemission study, *Semicond. Sci. Technol.* **27**, 124001 (2012).

93. H. Cao *et al*, Controlling and distinguishing electronic transport of topological and trivial surface states in a topological insulator, *ArXiv* 1409.3217 (2015).

94. Z. Ren *et al*, Large bulk resistivity and surface quantum oscillations in the topological insulator Bi_2Te_2Se, *Phys. Rev. B*, **82**, 241306R (2010).

95. O. B. Sokolov et al, Chemical reactions on the Bi_2Te_3-Bi_2Se_3 section in the process of crystal growth, *J. Crystal. Growth* **262**, 442 (2004).

96. A. Savitzky and M. J. E. Golay, Smoothing and differentiation of data by simplified least squares procedures, *Anal. Chem.* **36**, 1627 (1964).

Vita

Hyoungdo Nam was born in Changnyeong-gun, South Korea on July 5, 1977. In 1996, he entered Chung-Ang University majoring in Physics. After receiving the degree of Bachelor of Science in 2003, he entered the Graduate School of the same university while working as commissioned intern research scientist at Korea Institute of Science and Technology, and receiving the degree of Master of Science in 2006. In August 2008, he started the doctoral course in Physics, The University of Texas at Austin.

Permanent address: 3704 Speedway, Austin, 78705

This dissertation was typed by Hyoungdo Nam.